MODELLING THE MOLECULAR MECHANISMS OF BIOCOMPATIBILITY OF ARTIFICIAL MATERIALS

by

NADIYA DRAGNEVA

A thesis submitted to the

faculty of graduate studies

Lakehead University

In partial fulfilment of the

requirements for the degree of

Doctor of Philosophy in Biotechnology

Faculty of Graduate Studies

Lakehead University

May 2015

Thunder Bay Ontario

Abstract

One of the most common reasons for implant failure is immune rejection. Implant rejection leads to additional surgical intervention and, ultimately, increases health cost as well as recovery time. Within a few hours after implantation, the implant surface is covered with host proteins. Adsorption of fibrinogen, a soluble plasma glycoprotein, is responsible in triggering the immune response to a given material and, subsequently, in determining its biocompatibility. The work presented here is focused on modeling the interaction between artificial surfaces and plasma proteins at the microscopic level by taking into account the physico-chemical properties of the surfaces. Carbon-based nanomaterials are chosen as a model system due to their unique bioadhesive and contradictory biocompatible properties as well as the possibility of functionalization for specific applications. Graphene and its derivatives, such as graphene oxide and reduced graphene oxide, demonstrate controversial toxicity properties *in vitro* as well as *in vivo*. In this study, by covalently adding chemical groups, the wettability of graphene surfaces and the subsequent changes in its biocompatibility are being examined. An empirical force field potential (AMBER03) molecular dynamic simulation code implemented in the YASARA software package was utilized to model graphene/biomolecule interactions. The accuracy of the force field choice was verified by modeling the adsorption of individual amino acids to graphene surface in a vacuum. The obtained results are in excellent agreement with previously published *ab initio* findings. In order to mimic the natural protein environment, the interaction of several amino acids with graphene in an explicit solvent was modeled. The results show that the behaviour of amino acids in aqueous conditions is drasti-

cally different from that in vacuum. This finding highlights the importance of the host environment when biomaterial-biomolecule interfaces are modeled.

The surface of Graphene Oxide (GO) has been shown to exhibit properties that are useful in applications such as biomedical imaging, biological sensors and drug delivery. An assessment of the intrinsic affinity of amino acids to GO by simulating their adsorption onto a GO surface was performed. The emphasis was placed on developing an atomic charge model for GO that was not defined before. Next, the simulation of a fibrinogen fragment (D-domain) at the graphene surface in an explicit solvent with physiological conditions was performed. This D-domain contains the hidden (not expressed to the solvent) motifs (P1 γ190-202 and P2 γ377-395, and specifically P2-C portion γ383-395) that were experimentally found to be responsible for attracting inflammatory cells through CD11b/CD18 (Mac-1) leukocyte integrin and, consequently, promoting the cascade of immune reactions. It was hypothesized that the hydrophobic nature of graphene would cause critical changes in the fibrinogen D-domain structure, thus exposing the sequences and result in the foreign body reaction. To further study this issue, molecular mechanics was used to stimulate the interactions between fibrinogen and a graphene surface. The atomistic details of the interactions that determine plasma protein affinity modes on surfaces with high hydrophobicity were studied. The results of this work suggest that graphene is potentially pro-inflammatory surface, and cannot be used directly (without alterations) for biomedical purposes. A better understanding of the molecular mechanisms underlying the interaction between synthetic materials and biological systems will further the ultimate goal of understanding the biocompatibility of existing materials as well as design of new materials with improved biocompatibility.

Acknowledgements

I would like to thank my supervisor Dr. Oleg Rubel, for providing me with the opportunity to pursue a degree of Doctor of Philosophy in Biotechnology, and for his continuous advice and encouragement throughout the duration of my studies. Not least, he managed to create an open and positive atmosphere in all discussions, such that even critical comments were instructive and motivating rather than discouraging. I am very grateful for the help of my co-supervisor Dr. Wely B. Floriano. Her expertise in Bioinformatics made my life much easier. Dr. Floriano also made numerous helpful suggestions and comments that were finalized in published studies, and contributed a lot in planning my research. I would also like to thank Dr. Robert Mawhinney for giving a helpful critique to every and each of our studies. My committee member Dr. Marina Ulanova for guiding in the exciting world of Immunology. Thanks also goes to Darryl Willick for great technical support of Lakehead University and Thunder Bay Regional Research Institute high performance computational facilities as well as help in studying Linux. Finally, I would like to thank some essential contributor to my Doctoral study, Dennis Stauffer, a summer school and than co-op student who helped me a lot in analysis of works mentioned in chapters 3 and 4 without which my Doctoral work wouldn't be successful. This thesis would not exist without the help of my family and friends. Thanks ever so much for the support and understanding.

Dedication

Dedicated to my father, Sergiy Dragnev.

Contents

List of Tables

List of Figures

Chapter 1

Introduction

1.1 Patients' needs in advanced biomaterials

1.1.1 Orthopaedic implants and revision complications

The demand for bone replacements has been on the rise during the last few decades resulting in a high number of revision procedures, which are required when a failed implant needs to be replaced [1]. Although advances in hip replacement design and biomaterials have been made, implants tend to fail for a variety of reasons [2]. One of the main clinical issues of hip implants is aseptic loosening due to inflammation. Inflammation is a reaction of living tissue to local injury, and it is normally accompanied by heat, redness, swelling and pain. According to the Canadian Joint Replacement Registry in 2012-2013, aseptic loosening, the failure of the implant between an implant and bone in the absence of infection [3, 4], is the most common complication resulting in hip as well as knee revision surgeries. Hip revision surgeries have less probability for successful outcomes in comparison to first replacement surgery [5].

The averaged revision burden is found to be 13% [6–8]. The revision procedure is more complex, significantly invasive, and requires an increased recovery time (at the hospital and at home) as well as health costs [9, 10]. The hip prosthesis failure (rejection) costs million dollars annually [8]. In addition, the patient may experience morbidity and discomfort that lead to changes in his/her living arrangements (immobility). It also should be noted that the revised hip prosthesis will be able to function properly for a shorter time period in comparison with the first-time replacement (will require replacement five years sooner than the original implant).

Other specific risks for hip revision surgery include infection and deep venous thrombosis [11, 12]. However, what is more important, the length of the patients leg probably will be changed as a result of the surgery [13], which may lead to patient disability. Alberton et. al [1] show that the rate of prosthesis dislocations following hip revision surgeries is 7.4% [14]. In the case of revision procedures, the dislocations are more common because both bone and the attached tissue become weaker as a result of previous surgery. The analyzed mortality rate for the hip revision surgeries is averaged at 2.5% [8, 15–17]. Severe complications associated with hip and knee revisions include infection, aseptic loosening (22-26%) [8, 18], failure of osseointegration (16-18%) and others [17].

The chronic inflammatory reaction leads to implant rejection resulting in bone detachment and loss. Aseptic loosening can occur because of the poor biocompatible properties of the material [19]. The biomaterial may be non-toxic and bioinert, but at the same time trigger foreign body reaction. Beyond absence of toxicity and chemical inertness, the biomaterial is required to promote bone adhesion and healing. Biomaterials must accommodate specific chemical demands of the biological environment in

order to not lead to implant rejection. Otherwise, it provokes the immune pathways that result in the inflammatory reactions causing fibrous capsule formation. In this way the body tries to wall off and isolate the implant (foreign body) from the rest of the body by encapsulation.

1.1.2 Current state of existing biomaterials

The choice of material for orthopaedic applications has to satisfy several criteria such as strength, hardness, resistance to corrosion, flexibility and non-toxicity. Metals, one of the most popular material for implants, have been chosen for implantation purposes primarily because of their high strength [20]. Although the majority of metals and their alloys have been chosen in order to exhibit corrosion resistance, some of them show adverse effects to their biological environment [21].

The currently acceptable alloys are based on titanium, cobalt and stainless steel [22–24]. The stainless steel alloys show moderate mechanical properties such as lower strength, decrease in ductility, and corrosion resistance with time [25]. This make the stainless steel suitable only for short-term implants [21]. The wear resistance of stainless steel is rather poor and this is the reason why the metal-on-metal pairs in joints such as the hip fail. The reasons include high friction, large number of wear debris particles that are produced which leads to a rapid aseptic loosening.

Despite lots of excellent properties of titanium and its alloys such as mechanical strength, stiffness, toughness, and good corrosion resistance, their processing is technically difficult. There is also a problem of allergy and toxicity for NiTi alloys associated with the release of Ni ions [20]. The performance of titanium implants is

sensitive to geometrical factors. In general, metals may lead to an adverse mechanism, 'metal allergy', when the metal release ions that activate immune system. Other negative effects include corrosion, wear, limited durability, and even carcinogenesis [21].

Although polymer-based materials have a micro-structure and biodegradation rate that can be precisely monitored by fabrication of scaffold polymer materials [26], drawbacks of polymers include accelerated creep [27], poor stress corrosion and bone attachment [28]. The use of polymer components leads to gaps and loss of contact between the cement and the prosthesis and between the cement and the bone. The difference in stiffness between the metallic prosthesis and the bone may induce overstress or overstrain that may produce fractures in the cement and the release of cement particles that by interacting with the surrounding tissues may induce an inflammatory reaction.

Ceramics is found to be bioresorbable, however, the limitations in use of ceramics is brittleness and poor adhesion to the substrate [29–31]. Ceramic materials also suffer from early failures due to their low fracture toughness. Although highly porous ceramics expose a larger surface to the environment, and have been developed in order to promote bone ingrowth and to induce prosthesis stabilization, their compression strength can be affected by aging. Hydroxyapatite, a calcium phosphate ceramic, fails to coat orthopaedic implants by being too thick, unstable, and poorly adhesive to the substrate [32, 33]. To overcome limitations of existing materials, advance materials with biocompatible as well as bioadhesive characteristics should be investigated and developed. The aim of research in orthopaedic biomaterials is to meet the required characteristics for appropriate *in vivo* performance in order to minimize failure rate

[20]. It is important to note that perfect incorporation (combination) of mechanical, chemical, biocompatible, and bioadhesive properties is required for the successful performance of orthopaedic application. Particularly, materials that have a potential to enhance bone regeneration are of importance in applications for hip and knee repair purposes [34].

1.2 Inflammatory-mediated implant loss

1.2.1 Definition of biocompatibility

Biocompatibility is an ability of medical device to cause no harmful physiological effects to living tissues and cells [21, 35]. In other words, biocompatibility is an ability of medical device to function (perform) with appropriate host response. General criteria for biocompatibility is absence of immunogenicity, carcinogenicity and toxicity. The tests on biocompatibility and host response can be determined by implant surface assessment through calculating the number of inflammatory cells at the surface and in surrounding tissue, by measuring thickness of fibrous capsule, and cells apoptosis. At the atomistic level biomolecules and cells together with intrinsic properties of the chosen biomaterial determine biocompatibility as well as longevity of implants [36]. Recently, it was noticed that biocompatible characteristics of the materials are directly linked to the surface hydrophobicility (unfavourable water-surface interactions): the more hydrophobic surface, poorer blood compatible properties it expresses [37–40].

1.2.2 Foreign body reaction (FBR) of the host to the implant

The human immune system consists of innate (native) and adaptive (acquired) immunity [41]. Most of the currently used medical devices cause complications such as adverse non-specific immune reactions that are found to be under control of innate immunity [21]. Human body attempts to isolate (wall off) foreign material from the rest of the tissue by activating the following defence mechanisms. The same as for the foreign body, the activated macrophages try to phagocytose or engulf and degrade foreign body material, but due to disparity in the size they stimulate release of cytokines (proteins secreted by cells of innate immunity to regulate the cellular response) promoting chronic inflammation and fibrosis until the capsule around an implant is formed (this process is also called frustrated phagocytosis) [42]. At this point implant rejection takes place. The implanted device made of non-biocompatible surface may lead to the following processes: plasma protein adsorption, acute inflammation, chronic inflammation, implant failure due to fibrous formation (encapsulation) [41].

Inflammation occurs through a cascade of reactions. Shortly after contact with the surface, by default inactive phagocyte cells become active promoting differentiation and proliferation of others [43]. The reactions are quickly spread. Blood/surface interactions promote host response to biomaterial with insufficiently biocompatible properties. The adsorbed proteins accompany initiation of inflammation and further encapsulation. This is the first line of defence of the living organism that includes blood proteins, cytokines, phagocytes (macrophages, neutrophils), and natural killer cells [44].

Fibrinogen participates in the initiation of the immune reaction by activating the

inflammatory cells, while other blood proteins regulate already triggered immune response [45]. In particular, fibrinogen has been shown to promote inflammatory reactions through binding to phagocyte Mac-1 receptor (CD11b/CD18) (Fig. 1.2.2) [46–54].

Intensity and duration of inflammatory reactions depend on physical and chemical properties of the biomaterial [55]. Emigration of leukocytes (neutrophils) leads to phagocytosis, release of enzymes, activation of neutrophils and macrophages. Phagocytosis includes foreign body recognition, neutrophil attachment, engulfment, and degradation. The neutrophils and macrophages are found to have cell membrane receptors for proteins participating in opsonization processes. Opsonization is a process by which pathogens are bound to opsonin proteins, and therefore altered, so they become ready to be engulfed by phagocytes [56]. The CR3 (Mac-1) or CD11b/CD18 is a monocyte adhesion receptor responsible for triggering acute inflammation [57]. Neutrophils (or polymorphonuclear leukocytes) are associated with acute inflammatory response i.e. within first few minutes or days of implantation. Neutrophils become hyperadherent by increase of Mac-1 integrin expression at the surface [41].

Acute inflammation is triggered by phagocytes that tend to release small proteins, danger signal molecules such as cytokines and chemokynes (chemoattractant cytokines), that attract more monocytes and neutrophils and allow plasma proteins to defuse from the blood to the tissue [44]. The secreted chemoattractant cytokines include IL-1 (interleukin), TNF-α (cytokine tumour necrosis factor), IL-8 and others [42]. The IL-1 and TNF-α cause the endothelial cells of blood vessels near the site of infection to express cellular adhesion molecules in order to attach and facilitate migration of leukocytes. Also, an increased vascular permeability leads to entry of other

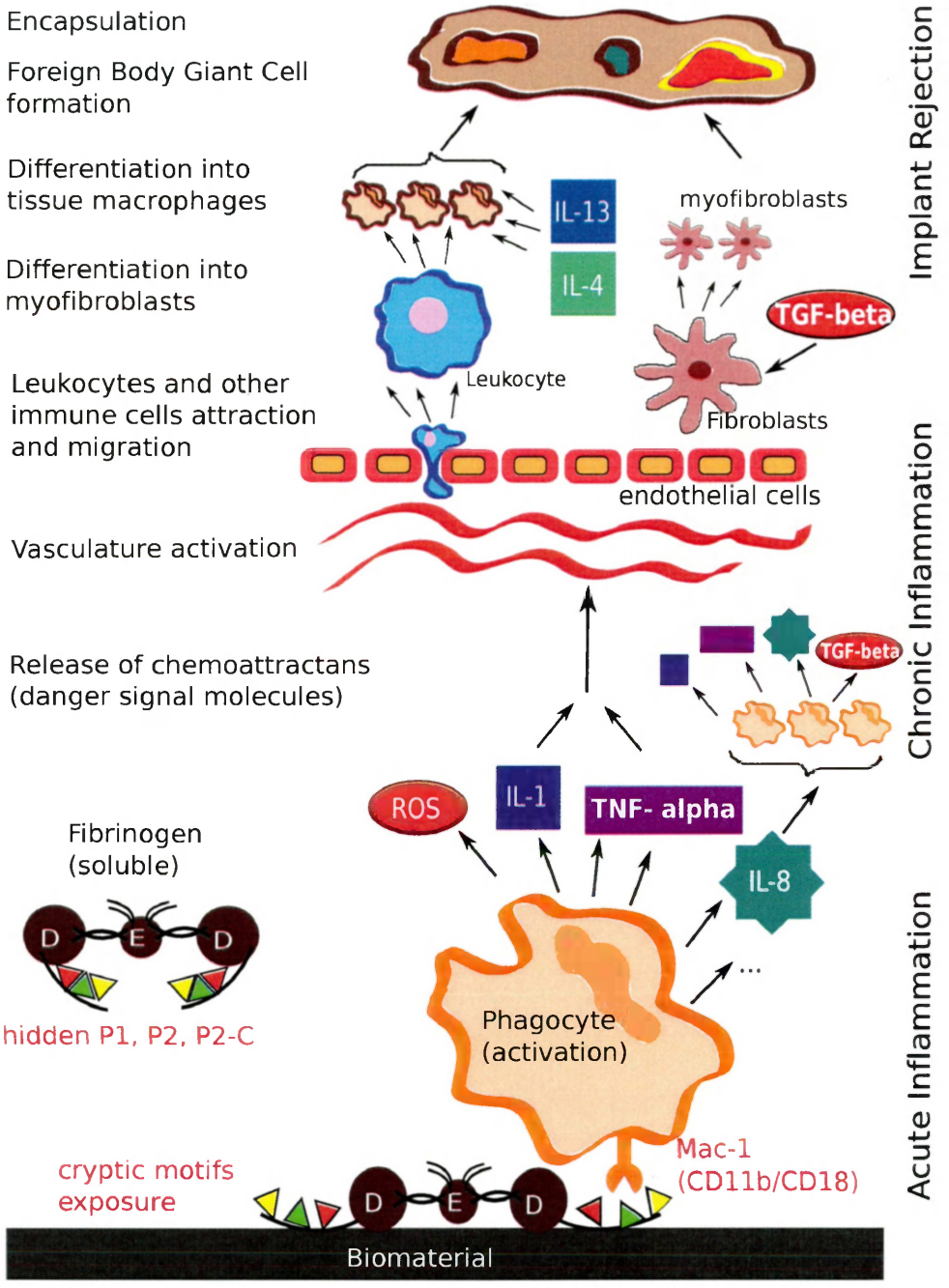

Figure 1.1: Simplified cascade of innate immune reaction triggered by binding of the exposed fibrinogen sites to phagocyte Mac-1 integrin.

blood proteins and cells to tissues. In response to IL-8 release, leukocytes become directed towards the implant site [41]. In other words, IL-8 activates leukocyte integrins promoting macrophage recruitment. Overall, cytokines that are produced by tissue macrophages increase vascular diameter, increase blood flow leading to inflammation that is accompanied by heat and redness [41]. As a result, the endothelium is activated and, instead of being joined together, the endothelial cells lining the blood vessel walls become separated, leading to an exit of fluid and proteins from the blood. The endothelial cells express cell-adhesion molecules, bind circulating leukocytes (i.e. neutrophils and monocytes) that migrate into tissue (extravasation) [58]. One of the leukocyte integrins that is important for extravasation is CR3 (complement receptor type 3, also known as CD11b/CD18 or Mac-1). All these changes are initiated by the pro-inflammatory cytokines and chemokines produced by activated macrophages. Monocytes than differentiate into tissue macrophages. IL-4 and IL-13 are inducers of foreign body giant cell (FBGC) formation (macrophage fusion) [57].

Chronic inflammation is mediated by macrophages, monocytes, lymphocytes, proliferation of blood vessels, and connective tissue [21]. Macrophages are phagocytic cells that engulf pathogens and destroy them [59]. The macrophage response is influenced by foreign material properties. Discrepancy in size of foreign material and macrophage cell causes fusion of macrophages into FBGCs leading to implant phagocytosis. Phagocytosis is a process when macrophages (phagocytes) engulf microorganisms or other cells and foreign particles in order to destroy them. If the biomaterial possesses high blood complatible properties, the FBGCs are absent. Macrophages together with FBGC products recruit fibroblasts [44]. Fibroblasts are connective tissue cells that deposit new collagen, secrete extracellular matrix (rich in collagen and other

macromolecules). Fibroblast cells differentiate into myofibroblasts, fibrotic tissue and capsule around implant [58]. Fibrous capsule is formed as a result of fibrosis which is the formation of fibrous connective tissue in an organ or tissue. The induction of fibrosis is mediated by (TGF)-β (transforming growth factor) [42]. TGF-β is expressed by macrophages. Extensive production of TGF-β leads to collagen, fibrinonectin and myofibroblasts production around implant. Myofibroblasts activate fibrotic tissue formation that isolates implant [58]. Fibroblasts deposit collagen, promote angiogenesis (growth of new vessels and capillaries from pre-existed ones) leading to encapsulation of implant by fibrous layer [21].

Other biomaterial/surface interactions leading to triggering inflammation may include complement system activation [21, 60–62], monocyte binding to fibrinogen through toll-like receptor (TLR4) [63–67]. These mechanisms are not investigated in this work due to the lack of experimental knowledge of specific molecular regions of fibrinogen participating in ligand-integrin interactions.

1.2.3 Leukocyte CD11b/CD18 (Mac-1) integrin

Integrin is a cell surface receptor that mediates cell-extracellular matrix and intercellular interactions [68]. Integrins allow a cell to migrate and respond to the environment. Integrins consist of α and β subunits [69]. Monocytes, macrophages and neutrophils express few of integrins. One of them is $\alpha_{\mathrm{M}}/\beta_2$ or Mac-1 (CD11b/CD18) integrin [65, 70]. Mac-1 is a key adhesion receptor that controls leukocyte adhesion, migration, immune and other cellular functions. Fibrinogen is one of the ligands for $\alpha_{\mathrm{M}}/\beta_2$, immobilized fibrinogen binds to leukocytes through $\alpha_{\mathrm{M}}/\beta_2$ integrin and

activates leukocytes promoting a cascade of immune reactions leading to implant rejection [46, 48–54, 71–77]. In support of this, Hu et al. [47] found that CD11b and CD18 knockout mice failed to accumulate phagocytes (monocytes, macrophages) at the surface of implant.

1.3 Factors controlling protein/surface interactions

1.3.1 Blood proteins adsorption

Shortly after implantation, the artificial surface of implanted material is covered by adhered plasma proteins, these processes result in creating a new interface between substrate and the blood [78]. The proteins primarily bound to the surface may eventually leave due to competitive adsorption processes between plasma proteins [21]. There are about 2,982 proteins present in the blood [79]. However, the surface may be dominantly attracted by proteins with high concentration or 'the big twelve' proteins: albumin, immunoglobulin G, α1-antitrypsin, transferrin, haptoglobin, low-density lipoprotein, high-density lipoprotein, immunoglobulins, complement C3, fibrinogen, and α2-macroglobulin, immunoglobulin M [62]. Early proteins leave the surface to allow new ones to adhere. The tightly adsorbed proteins may undergo the following changes: rearrangements, folding/unfolding states such as partial or complete denaturation. Fibrinogen, one of the most abundant plasma proteins, will be adsorbed to the surface creating a protein film that generates recognition patterns for a variety of immune cells [80]. The cascade of immune reactions involve inflammatory cells migration, adsorption, recognition, activation, engagement, and differentiation

mechanisms [21] (see also Sec. 1.2 for details). The outcome of these processes depends on the composition and conformation of protein layer formed at the artificial biomaterial surface. The adsorbed protein layer affects functionality of the medical implant as well as patient's treatment time. The insufficient (poor) biomaterial quality may be identified by chronic inflammation and fibrous capsule formation. Despite a variety of existing artificial materials that can be used for manufacturing bioimplants, it remains a challenge to find an ideal material with optimal properties. Some of the available biomaterials tend to stimulate the adverse immune reactions as result a of human body defence mechanisms.

The well-known artificial materials adsorb plasma proteins interacting with the blood. This phenomenon occurs during the first few milliseconds of interaction and continues until a saturation level of adsorbed layer is reached. Structural characteristics of proteins in the formed layer are influenced by protein concentrations on the one hand, and surface and protein chemical properties on the other [81]. These are factors related to activation of immune cascade i.e. plasma proteins adsorption and consequent immune cells attraction.

There are internal and external factors that affect protein/surface interactions [81]. The external factors include conditions at which experiments with proteins are usually performed such as temperature, pressure, pH level, concentration of dissolved ions. Plasma proteins are biomolecules that, in order to function properly, require physiological environment close to blood i.e. body temperature, atmospheric pressure, and appropriate to blood sodium chloride concentration. Important internal factors responsible for degree of proteins adsorption and formed layer composition are surface wettability, polarity, and pattern of the functional groups because the surface

mediates response to physiological environment [21, 62]. Depending on wettability properties, surfaces are divided into hydrophobic ('water-fearing') and hydrophilic ('water-loving') (see Sec. 5: Fig. 5.2a). The degree of wettability of the surface is defined by measuring a contact angle (θ) between a solid surface and liquid: a contact angle that is less than 90° corresponds to high wettability (a liquid droplet will spread over a large surface area), and a large contact angle 90° indicates low wettability (fluid will form a compact liquid droplet on the surface minimizing its contacts) [82].

The ability of the surface to adhere cells and proteins is pre-defined by the Berg limit [83]. Surface becomes resistant to biomolecules when its contact angle is less than $50-60°$ [84]. It is a known fact that proteins have a tendency to undergo significant conformational changes upon their binding to hydrophobic surface in contrast to hydrophilic. The higher affinity to hydrophobic surface leads to more substitutional structural changes in proteins. Also, the presence of covalently attached chemical groups at the surface allows proteins, consisting of domains with different polarity, reorient and reorganize themselves to find the most electrostatically favourable positions/conformations at the surface regions as it is shown in Fig. 1.2. It is important to note that signalling immune cells react to the content and shape of the adsorbed protein layer rather than to the implanted surface [81, 85].

Nowadays, the ultimate goal of research in orthopaedic applications is to investigate biomaterials that have appropriate cellular responses due to its ability to provide bone tissue regeneration function while not promoting foreign body reaction. In other words, the physico-chemical properties of the synthetic biomaterial need to be balanced to contribute to the bone healing process.

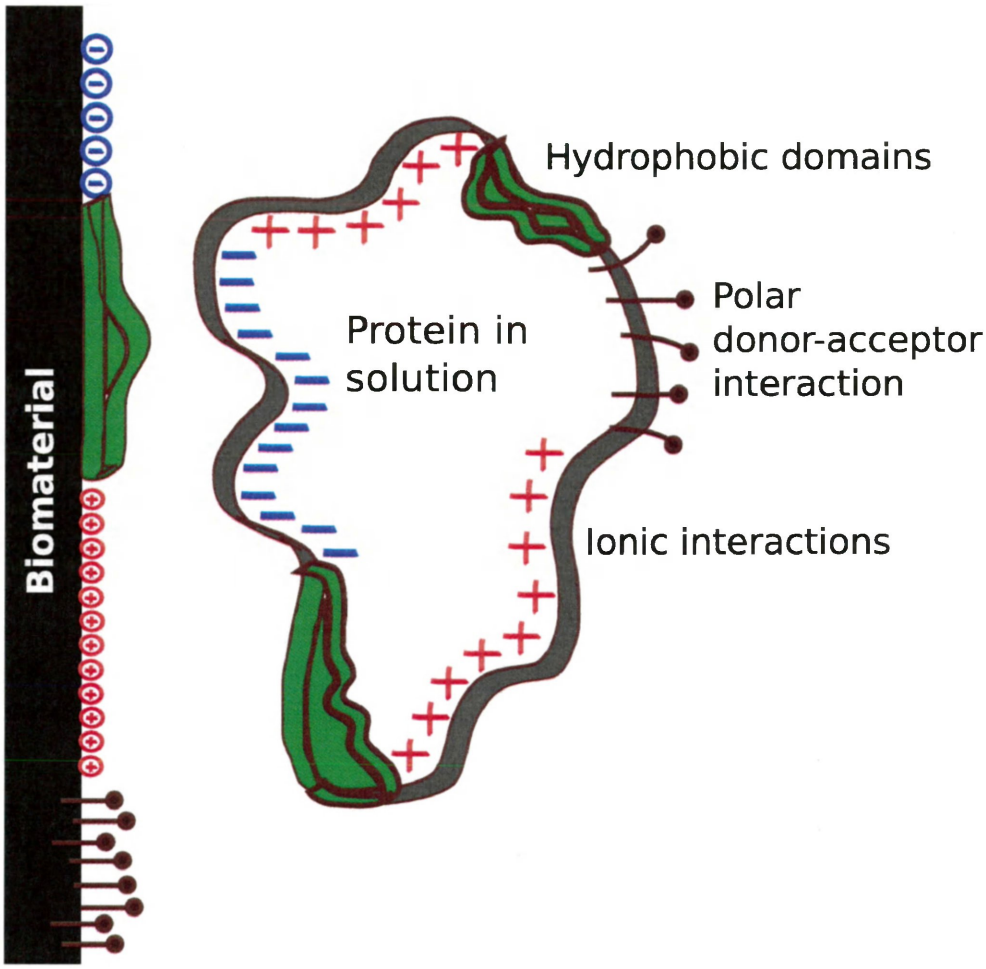

Figure 1.2: Both surface (polarity, wettability, morphology) and proteins (polarity, composition, size, complexity) properties define outcome of their contact (Adapted from Ref. [83]).

1.3.2 Surface properties and Berg limit

It has been found that surface wettability is a one of the major factors related to implant rejection. Specifically, blood proteins show a tight affinity to hydrophobic and positively charged surfaces. For example, titanium dioxide is known to be a widely-used biocompatible material. This can be explained by an oxide layer, which normally covers titanium implants. Titanium dioxide is hydrophilic and polar surface, it prefers to attract water molecules instead of proteins. Cacciafesta et al. [86] report that fibrinogen does not adhere to titanium dioxide because both the protein and the surface are negatively charged at physiological conditions. This causes electrostatic repulsion. Although the inert behaviour of titanium and titanium alloys is a good property, it does not interact with human tissues leading to controversial results on cellular bone adhesion and attachment [87]. Although it is believed that titanium dioxide coated with hydroxyapatite, a natural mineral formed of calcium apatite [88], meets the bioadhesive as well as biocompatibility requirements of bone implant [87]. Both these materials have been found to mediate an expression of inflammatory cells and lead to cell death [89]. Therefore, surface functionalized with different chemical groups can either promote or prevent adverse immune reactions [90]. Appropriate mixtures and patterns may facilitate material's biocompatibility. One of the plasma proteins, fibrinogen, has been shown to trigger adverse immune reactions due to its structural changes after adsorption to artificial hydrophobic materials.

1.3.3 Fibrinogen - main initiator of foreign body reaction

While the atomistic details of the interactions at the protein/surface interface remain undefined, the conformational changes of adsorbed protein are found to be responsible for initiating adverse immune reactions. Fibrinogen, a plasma protein, is a key factor for foreign body reactions [21, 91]. On the one hand, the processes related to wound-healing mechanisms force the fibrinogen to be hydrolyzed by thrombin (protease that converts soluble fibrinogen into insoluble fibrin, coagulation factor) to fibrin. The dense fibrin network is created and than detected by macrophages and neutrophils. The fibrin network also promotes leukocyte adhesion [80]. On the other hand, soluble fibrinogen was shown to be non-reactive to immune cells, while adsorbed and/or denatured fibrinogen participates in cells binding [80]. Fibrinogen interactions with the surface may cause conformational changes, structural changes of the previously inaccessible binding motifs (P1 and P2) [48, 51–54, 75, 80, 92]. These P1 and P2 cryptic sites become biologically active when fibrinogen undergoes structural changes as a result of adsorption to the surface. The specificity of cryptic sequences has been identified by implementing mutation to fibrinogen γ 390-396 region that was replaced with alanine amino acids [74]. As a result of *in vivo* experiment, modified fibrinogen did not support adhesion of the previously proved immune cells (neutrophils, macrophages), and as a result failed to trigger immune reaction.

The cryptic sequences bind to Mac-1 phagocyte integrin receptors, activate tissue phagocytes that, consequently, release chemokines and cytokines [62]. The chemoattractants activate vasculature (increased permeability of blood vessels) and recruit leukocytes and fibroblasts (connective tissue cells). Fibroblast cells then differentiate

into myofibroblasts resulting in fibrotic tissue and capsule around implant.

Fibrinogen is an amphiphilic molecule. Hence, it may overcome significant structural rearrangements if interactions between proteins and the surface are stronger than internal bonds of protein (for example, hydrophobic and hydrogen bonds). This plasma protein has been studied by theory and experiments for the interactions with a wide range of surfaces. In general, fibrinogen shows a high affinity and significant structural changes onto hydrophobic surfaces [93–95] in comparison to hydrophilic [93, 96–98]. As it was mentioned before, human plasma contains a vast amount of proteins that demonstrate a competitive behaviour. As a result, fibrinogen showing slight adsorption to hydrophilic surface may be rapidly replaced (exchanged) by other low-concentration proteins. Also it has been noticed that fibrinogen stays indifferent to neutral and negatively charged substrates [86, 99, 100], in contrast to positively charged surfaces. This behaviour is due to the fact that, under the physiological conditions, fibrinogen is a negatively charged biomolecule and shows electrostatic repulsion to similarly charged surfaces [101].

1.4 Required implant surface properties

1.4.1 Synergy of biocompatible and bioadhesive properties

Bioadhesion, or attraction of the molecules to the surface, plays a significant role in design of orthopaedic devices. Bioadhesion can be specific and non-specific [102]. For the purposes of this work, non-specific bioadhesion is discussed. The non-specific bioadhesion occurs through non-bonded interactions such as electrostatic, hydrogen

bonding, hydrophobic or van der Waals interactions. Non-fouling surfaces have been extensively studied because of their ability to stay indifferent to proteins, they have non-adsorptive properties. It is generally recognized that hydrophilic surfaces have a potential to resist protein adhesion, hydrophobic surfaces tightly adsorb a monolayer of plasma proteins, while non-fouling surfaces totally resist the adsorption of proteins together with cells [103]. A strongly hydrophilic surface prevents the adsorption of proteins at the same time reducing the adhesion of cells [104]. However, different adhesion mechanisms of cells can lead to the tissue development. For example, osteoblasts (bone cells) may adhere to the material creating a new layer of bone tissue [105, 106]. Therefore, enhancement of bone regeneration in tissue engineering applications can be achieved only for materials expressing adhesive properties [34, 107]. Osseointegration, a direct structural and functional connection between ordered, living bone and the surface of a load-carrying implant [108], being a very relevant issue for the anchorage of implants in the surrounding bone, great effort is being made in the design and optimization of bio-surfaces. The ideal material has to promote osseointegration independently of bone quality and/or quality that is available at the implant-tissue interface [109]. However, so far there is no material found to be suitable equally for both biocompatible and bioadhesive requirements.

1.4.2 Graphene-based nanomaterials and its derivatives

Graphene has been intensively studied during the last decade for biomedical applications [110–112]. Graphene is a one atom thick nanomaterial that consists of carbon atoms covalently bound and arranged in a hexagonal structure [113, 114]. In other

words, graphene is a one layer of well-known graphite. Despite its simple structure, this two-dimensional material has been shown to have lots of unique properties [115]. It has to be highlighted that pure graphene is a highly hydrophobic surface [116]. Also, graphene is chemically inert, however, $\pi - \pi$ stacking elicits non-specific binding of molecules that have aromaticity such as most of organic molecules, for example. Graphene shows the highest Young's modulus among existing materials. Graphene can also be easily functionalized with a variety of chemical groups [117–120]. One of the specific cases of graphene functionalization is graphene oxide. Graphene oxide (GO) [121], oxidized graphene with covalently attached epoxy, hydroxyl, and rarely carbonyl groups, is a negatively charged amphiphile material, i.e. it demonstrates both hydrophilic and hydrophobic properties. GO shows antibacterial properties, i.e. it can be harmful to bacteria [122].

It needs to be emphasized that graphene topography is very simple. As a result it can be easily produced without significant defects and impurities. Therefore, graphene can work as an ideal model for adherent cells experiments, for example, to study human osteoblasts (bone cells) [101, 123–125]. However, the interesting point here is that graphene may work as a good example for bone regeneration applications due to its ability to bind bone morphogenetic protein (BMP-2) that enhances osteogenic differentiation [126]. Moreover, graphene accelerates multi-potent stromal cells (that may differentiate in osteoblasts) differentiation even without growth factor, increases calcium deposition, and has no affect on stem cells showing a stable growth and differentiation [127].

On the other hand, the mechanism helping to kill bacteria (sharp graphene edges, and highly reactive carboxyl groups of graphene oxide) may also express toxicity to

normal human cells because graphene oxide damages cell membrane through electrostatic interaction between negatively charged epoxy groups and positive lipids of the cell membrane. Therefore, there are still lots of unresolved issues and questions related to graphene. Graphene and its derivatives such as graphene oxide, reduced graphene oxide demonstrate controversial toxicity properties *in vitro* as well as *in vivo* [128]. For *in vitro* cell tests, it is important to analyze cell morphology, adhesion, migration and proliferation at the surface. Bianco et al. [128] gives a comprehensive review on cell and animal studies for investigating toxicity characteristics of graphene. The obtained results show a dependence on the number of graphene layers, stiffness, wettability, functionalization of the surface with chemical groups, dose and if defects are present [128]. For example, accumulation of graphene in life-dependent organs (spleen, kidney and brain) demonstrates dose-dependent toxicity. No standard assay methods have been developed for graphene toxicity mainly because graphene is a quite new material, and long-term effects take time to be monitored. In this work, I examine the potential toxicity of graphene surface and summarize the biological pathways contributing to its failure.

1.5 Hypothesis and objectives

There is an evident need in reducing the number of revision surgeries that would benefit both patients and the health system. It is understood from the facts discussed above, that performance and life expectancy of bone implants are crucially dependent on the biomaterial biocompatible and bioadhesive characteristics. One solution that can help to improve implant performance is to facilitate the design of advanced

biomaterials by uncovering the biological mechanisms of biocompatibility and bone healing (formation) that will find its application in clinical care.

The objective of this work is to investigate biocompatible and bioadhesive properties of the surface by examining protein-surface interactions using molecular dynamics simulations (Fig. 1.3). The hypothesis of this work is that highly hydrophobic graphene surface will lead to structural changes of fibrinogen cryptic sites hidden in γ-chain within D-domain due to tight protein adsorption. The molecular nature of the solvent as well as realistic model for graphene surface will be taking into account.

The immediate research contribution is understanding molecular mechanisms influencing biomaterial rejection. The long-term goals are to decrease morbidity, improve patient psychology, reduce revision surgery rate, recovery time and health care costs.

This theoretical work is divided into six chapters. The first chapter gives an introductory literature review on the current state of biomaterials used for orthopaedic purposes, the immune and molecular mechanisms that were experimentally found to be responsible for implant rejections. In Chapter 2, the methodological details as well as theoretical background of the MD and DFT calculations are provided. In Chapter 3, the amino acids adsorption at the surface of graphene is examined by means of AMBER03 force field. The simulation results are linked to experimental and *ab initio* results and demonstrate a distinct picture of desolvation effect as well as sequences termination for biomolecule-surface simulations. As a prerequisite for the accurate description of the fibrinogen adsorption processes, in Chapters 3-4, a method for the simulation of the simple biomolecules (amino acids) at the surface of graphene and graphene oxide is validated. Specifically, in Chapter 4, the charge model for graphene

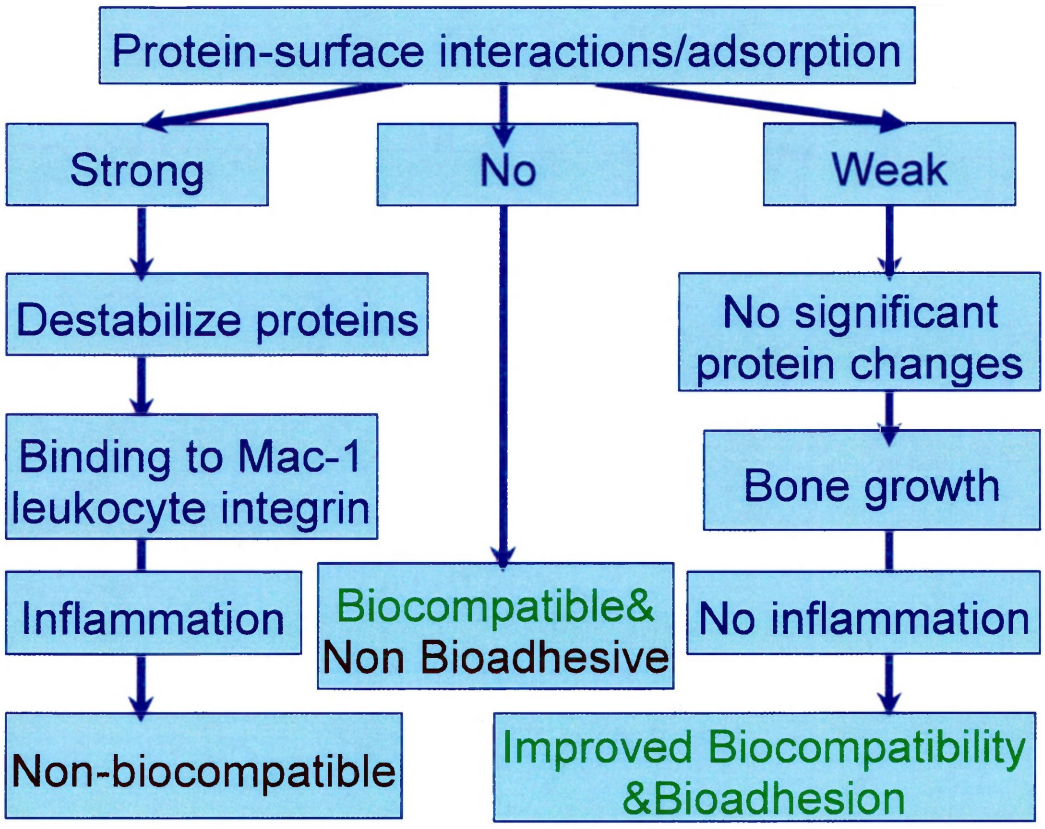

Figure 1.3: Schematic view of the hypothesis: strength of protein adsorption and degree of its conformational changes defines biomaterial bioadhesive as well as biocompatible properties.

oxide was developed and verified. Finally, in Chapter 5, the adsorption behaviour of fibrinogen D-domain at the surface of graphene and PEG monolayer is examined. The dynamics of D-domain and its cryptic sites at the atomic level using extensive MD simulations in explicit solvent were analyzed. The large size of this fragment (the simulation system with explicit solvent comprised about 700,000 atoms) and the fact that protein unfolding mechanisms may take few minutes to finish made this project computationally quite challenging.

Chapter 2

Methodology

This chapter outlines the methodological framework of this work. Subdivided into sections, it comprises summaries of density functional theory and classical molecular dynamics simulations. In order to validate the chosen molecular dynamics approach for complex models, the quantum mechanical method results were obtained for small-sized systems. For more detailed information, please refer to the cited references.

2.1 Fibrinogen structural details

2.1.1 Basics of protein structure

Proteins are long-chain polymers that consist of simple building blocks, amino acids, bound to each other forming a polypeptide chain [129] (Fig. 2.1). There are 20 basic amino acids that are categorized into several groups with respect to hydrophobic, aromatic, polar, acidic or basic characteristics of their chemical structure as well as their sizes. Each amino acid contains amino and carboxyl groups as well as a side

chain that is unique. The carbon atom to which the variable side chain attaches is called carbon-α. The ionization state of an amino acid is a function of surrounding pH. Amino acids are in their zwitterionic (isoelectric) form at physiological pH (7.0). pKa, the logarithmic measure of the acid dissociation constant, shows how acidic (or not) a given hydrogen atom is in a molecule, while pH tells how acidic the solution is. For example, when pH in physiological environment is 7.0, and is higher than pKa for carboxyl group (in a range of 3 to 5), carboxyl group donates its proton and becomes COO^-. The same principle is applied for amino groups and ionizable side chains. As a result, in this form the net charge on protein is equal to zero because COO^- and NH_3^+ charge. The nomenclature of amino acids includes one-letter and three letter codes [129].

The biological function of the protein depend on its structure. The primary structure of the protein is an order of amino acids covalently joined in polypeptide. It defines main protein features. The polypeptide bonds are formed via a dehydration synthesis reaction between the carboxyl group of the first amino acid with the amino group of the second amino acid. According to secondary protein structures, a protein consists of α-helices, β-pleated sheets pattern and turns. In an α-helix, the protein chain is coiled like a spring or helix. The structure is maintained by hydrogen bonds between i and $(i+4)$ adjacent groups. In the β-sheet structure, the chains are folded in a zig-zag pattern. This structure is preserved by hydrogen bonds between backbones (or main peptide chains). The β-sheets can be parallel or antiparallel. The tertiary protein structure is its 3-dimensional shape. The tertiary structure is created by more than one protein domain - a compact and self-folding part of the polypeptide chain that represents a discreet structural and functional unit due to ionic, van

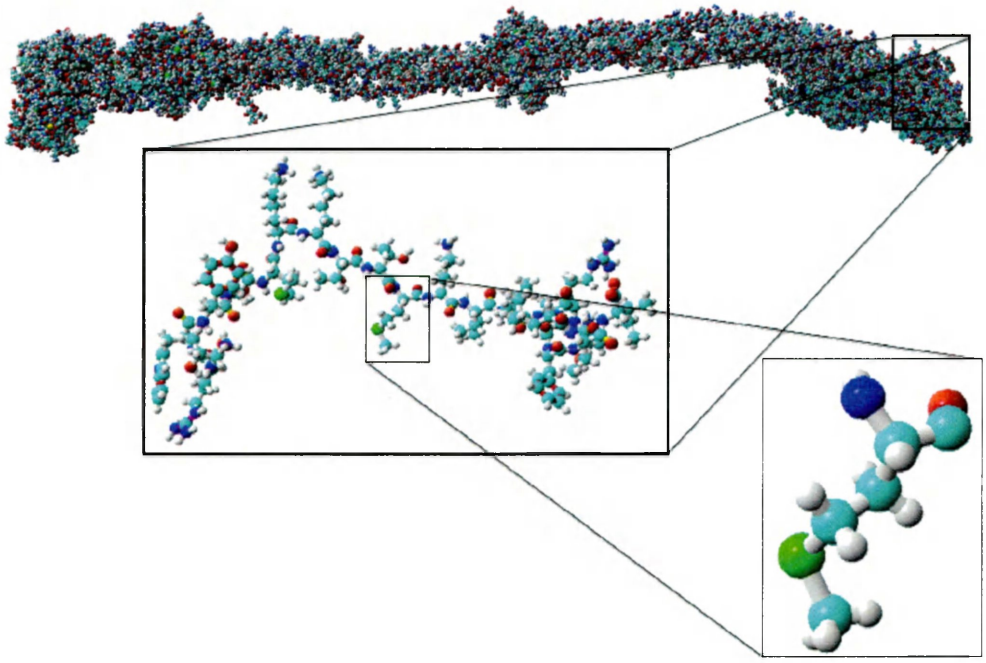

Figure 2.1: Zoom into protein (fibrinogen): peptide and amino acid.

der Waals interactions as well as hydrogen and disulphide bonds [130]. The quaternary structure consists of more than two polypeptide chains. It is an association of subunits: dimers, trimers.

If shape of the protein is significantly modified, its function is also disrupted. Denaturation is a process that alters a protein shape through some form of external stress (by heat, acid or alkali). The called 'native' structure of a protein is the form of a protein in an active state from a natural source. If the protein irreversibly loses its structure, for example by unfolding, it loses the biological activity too.

A protein has size and shape as well as unique arrangement through hydrogen, ionic, hydrophobic and disulfide interactions. Polypeptide chains contain numerous proton donors and acceptors both in their backbone and in the side-chains of the

amino acids. The environment in which proteins are found also contains hydrogen bond donors and acceptors such as water molecules. Hydrogen bonding, therefore, occurs not only within and between polypeptide chains but with the surrounding medium.

Water is a poor solvent for non-polar substances. The hydrophobic effect is a passive interaction between groups with hydrophobic properties causing them to aggregate and exclude water molecules. It is due to the self-assembly features of water resulting from strong directional and complementary interactions between individual water molecules. It controls the folding of proteins as well as leads to denaturation of proteins at the hydrophobic biomaterial surface. Proteins are composed of amino acids that may contain hydrophilic and hydrophobic side-groups. It is the nature of the interaction of different side-groups with the aqueous environment that plays the major role in shaping protein structure. The spontaneous folded state of globular proteins is a reflection of a balance between the opposing energetics of hydrogen-bonding between hydrophilic groups and the aqueous environment and the repulsion from the aqueous environment by the hydrophobic side driving them into the interior.

Electrostatic forces are mainly of three types: charge-charge, charge-dipole and dipole-dipole. Typical charge-charge interactions that favor protein folding are those between oppositely charged side-groups. A substantial component of the energy involved in protein folding is charge-dipole interactions. This refers to the interaction of ionized side-groups of amino acids with the dipole of the water molecule. The slight dipole moment that exist in the polar side-groups of amino acid also influences their interaction with water. It is, therefore, understandable that the majority of the amino acids found on the exterior surfaces of globular proteins contain charged or

polar side-groups.

There are attractive van der Waals forces that control protein folding. Attractive van der Waals forces correspond to the interactions among induced dipoles that arise from fluctuations in the charge densities that occur between adjacent uncharged non-bonded atoms. Although van der Waals forces are weak, relative to other forces governing conformation such as electrostatic or hydrophobic interactions, it is the huge number of such interactions that occur in large protein molecules that make them significant to the folding of proteins. Based on the structure and solubility, proteins can be grouped into three large classes: globular, membrane and fibrous.

2.1.2 Fibrinogen

Fibrinogen is a soluble fibrous protein that is synthesized in a liver [131] (Fig. 2.1). It controls bleeding after injury by creating fibrin network (thrombus formation) [132]. Fibrinogen is also responsible for initiation of acute inflammation, fibrous capsule formation and implant rejection as a response to foreign material as mentioned in Sec. 1.3.3 [92]. Fibrinogen's main function is to identify and isolate the foreign material surface in the body. It is a regulator of innate inflammatory response.

Fibrinogen is a dimer consisting of two sets of three chains (Aα, Bβ and γ) that are joined together by five disulphide bridges [92]. The chains consist of 610, 461, and 411 amino acids, respectively [133]. The chains are coiled-coil together and create two hydrophobic D-domains at the ends that are linked by a central hydrophilic E domain. The fibrinogen is about 47.5 nm in length and 6.5 nm in diameter [134]. Upon convergence to fibrin, fibrinogen releases two fibrinopeptides (A, B), and par-

ticipates in fibrin network formation binding of each other through specific regions in D-domains [132].

Polarity and hydrophobicity of the surface influences fibrinogen's structure. In its natural state, fibrinogen has a trinodular structure. However, fibrinogen tends to spread out on hydrophobic and positively charged surfaces in contrast to hydrophilic and negative charged. As a result, fibrinogen's geometric properties such as length, width and height change [135]. This behaviour can be explained by strong fibrinogen/surface bonds that significantly dominate fibrinogen's structural internal forces. In support of this, fibrinogen has been found to adsorb for much shorter period of time, low strength and adhesion forces to highly wettable surfaces in contrast to poorly wettable [84].

In the framework of molecular dynamics, fibrinogen is a very complex biomolecule consisting of more than 30,000 atoms. However, it can be cut into smaller units i.e. functional fragments that maintain their natural properties. Fibrinogen D-domain is an individual functional domain that contains P1 and P2 hidden sites that bind to phagocyte integrin Mac-1(CD11b/CD18) when exposed. Their exposure is directly related to severity of inflammatory responses. The cryptic motifs are placed far apart in the polypeptide chain, but appear to be close neighbours, antiparallel β strands, in a folded protein. Soluble fibrinogen does not cause unmasking of P1 or P2 motifs. Therefore, one can expect, that surfaces inducing significant exposure of P1 and P2 might trigger maximal inflammatory reaction.

2.2 Density functional theory

Density functional theory (DFT) is a computational tool for materials modelling problems [136]. DFT is able to predict a great variety of molecular properties such as molecular structures, vibrational frequencies, atomization energies, ionization energies, electric and magnetic properties. It is an approach to finding solutions to the fundamental quantum-mechanical Schrödinger equation that describes the quantum behaviour of atoms and molecules. In contrast to Newton's equations, solution of the Schrödinger equation does not provide unique trajectories, but only probabilistic statements about the positions and impulses of the particles. All statements related to a quantum mechanical system can be derived from the state function (or wave function) Ψ which is given as the solution of the Schrödinger equation.

2.2.1 Basics of quantum mechanics

The particles in quantum mechanics are described by the wave-function

$$\Psi(\mathbf{R}, \mathbf{t}). \tag{2.1}$$

Instead of a defined position of the particle, there is a probability distribution function of finding the particle at a particular position and time [137]

$$|\Psi(\mathbf{R}, \mathbf{t})|^2. \tag{2.2}$$

For each nucleus in the system, there are several electrons, therefore, the wave-function depends on all the nuclei (R_N) and electronic (r_N) coordinates with time

$$\Psi(\mathbf{R}_1, \mathbf{R}_N, \mathbf{r}_1, \mathbf{r}_N, \mathbf{t}). \tag{2.3}$$

The wave function captures all the observable behaviour of the particle. To compute a particular property, the corresponding operator needs to be applied, the property is extracted as an observable. Time-dependent Schrödinger equation is the following

$$H\Psi(\mathbf{R}, \mathbf{t}) = \mathbf{i}\hbar\frac{d}{d\mathbf{t}}\Psi(\mathbf{R}, \mathbf{t}). \tag{2.4}$$

The time-independent Schrödinger equation has the form

$$H\Psi(\mathbf{R}, \mathbf{r}) = E\Psi(\mathbf{R}, \mathbf{r}) \tag{2.5}$$

Here E is the energy eigenvalue, $\Psi(R, r)$ is the corresponding eigenstate or the wave function.

The full Hamiltonian of the system consists of the sum of Coulomb electrostatic interactions for all nuclei and electrons that is

$$H(\mathbf{R}, \mathbf{r}) = T_n(\mathbf{R}) + U_n(\mathbf{R}) + T_e(\mathbf{r}) + U_e(\mathbf{r}) + U_{n-e}(\mathbf{R}, \mathbf{r}) \tag{2.6}$$

or

$$\hat{H} = -\sum_{n=1}^{K} \frac{\hbar^2}{2M_n} \nabla_n^2 + (8\pi\epsilon_0)^{-1} \sum_{n=1}^{K} \sum_{n' \neq n}^{K} \frac{Z_n Z_{n'} e^2}{|\mathbf{R}_n - \mathbf{R}_{n'}|}$$
$$- \sum_{i=1}^{N} \frac{\hbar^2}{2m_0} \nabla_i^2 + (8\pi\epsilon_0)^{-1} \sum_{i=1}^{N} \sum_{j \neq i}^{N} \frac{e^2}{|\mathbf{r}_i - \mathbf{r}_j|}$$
$$- (4\pi\epsilon_0)^{-1} \sum_{i=1}^{N} \sum_{n=1}^{K} \frac{Z_n e^2}{|\mathbf{r}_i - \mathbf{R}_n|} \quad (2.7)$$

Here, $\hbar$ is an angular momentum, ϵ_0 is the vacuum permittivity, Z_n - the atomic number of nucleus, M_{n} is nucleus mass at R_{n}, and m_0 - electron mass at rest; K and N are the numbers of nuclei and electrons in the system, respectively. The first two terms describe kinetic and potential energies for nuclei, the third and forth are corresponding energies for electrons interactions, and the last term represents potential energy between electrons and nuclei [137].

The many-body wave-function is a non-trivial and cannot be solved directly. Therefore, a few approximations and theories have been developed in order to find solution for the complex Schrödinger equation [138]. One of them is the Born-Oppenheimer approximation. According to this theory, the nuclei mass are much more higher than electrons and as a result, nuclei move with lower velocities.

The Hamiltonian for time-independent Schrödinger equation consists of kinetic energy for the electrons (for nuclei the velocities are zero because they are stationary) and potential energy that is divided into two terms: potential energy of the electrons that interact with the nuclei and electrons interacting with other electrons.

$$\hat{H} = -\sum_{i=1}^{N} \frac{\hbar^2}{2m_0}\nabla_i^2 + (8\pi\epsilon_0)^{-1}\sum_{i=1}^{N}\sum_{j\neq i}^{N} \frac{e^2}{|\mathbf{r}_i - \mathbf{r}_j|} - (4\pi\epsilon_0)^{-1}\sum_{i=1}^{N}\sum_{n=1}^{K} \frac{Z_n e^2}{|\mathbf{r}_i - \mathbf{R}_n|} \quad (2.8)$$

Although now the quantum many-body equation is much simpler after applying the Born-Oppenheimer approximation [139], it is still challenging to solve due to the fact that locations of all electrons need to be defined to calculate the electronic potential energy. A few methods on reducing this equation without significant affect on the quality of the result exist. The Born-Oppenheimer approximation is usually very useful, but it breaks down when two (or more) electronic states are close in energy at particular nuclear geometries.

Hartree (1928) suggested to use electron density of the system instead of time-independent electron interactions [140]. According to Hartree theorem, electron interacts with average electron density, not with every single electron i.e. mean-field approximation.

$$U_H = \frac{e^2}{4\pi\epsilon_0}\int \frac{n(\mathbf{r})}{|\mathbf{r_i} - \mathbf{r_j}|}d\mathbf{r} \quad (2.9)$$

Where, $n(\mathbf{r})$ is the time averaged electron density of the system. The ground state density for N electrons in the system is the following

$$n(\mathbf{r}) = \sum_{i=1}^{N} |\Psi_i(\mathbf{r})|^2 \quad (2.10)$$

As a result, the simplified Hamiltonian is expressed in the next equation

$$H_H = T_0(\mathbf{r}) + U_H\left[n(\mathbf{r})\right] + U_{n-e}(\mathbf{r}, \mathbf{R}) \tag{2.11}$$

Where, T_0 represents the kinetic energy of a non-interacting electron gas (the ground state density), U_{n-e} is electron-nuclei potential. A set of orbitals that is a solution to the Hartree-Fock equations are called self-consistent field orbitals [137].

In order to eliminate electron interactions with itself (as a part of averaged electron density), the exchange potential was introduced into Hartree equation by Fock (1930) [139]. This term modifies the self-interaction of electrons. Electron-electron repulsion is included as an average effect. The electron repulsion felt by one electron is an average potential field of all the others, assuming that their spatial distribution is represented by orbitals, however, the electron correlation has been neglected. The Hartree-Fock theorem limitation include the basic assumption that electrons move independently in some average potential produced by all the electrons [137]. The popular quantum-mechanical method that takes into account correlation of electrons is density functional theory.

The density functional theory is an outcome of Hohenberg-Kohn method. Based on the Hohenberg-Kohn theorems (1964) [137], the external potential is a unique functional of the electron density and this functional has its minimum at the ground-state density [140]. In other words, if a three-dimensional electron density is defined, the properties of the Eq. 2.5 can be calculated. The ground state energy functional is

$$E_{U_{n-e}}[n(\mathbf{r})] = F_{HK}[n(\mathbf{r})] + \int n(\mathbf{r})\, U_{n-e}(\mathbf{r})\, d\mathbf{r} \tag{2.12}$$

$$E[n(\mathbf{r})] = T[n(\mathbf{r})] + E_H[n(\mathbf{r})] + E_{xc}[n(\mathbf{r})] + U_{ext}[n(\mathbf{r})] \tag{2.13}$$

Here, U_{ext} is an external potential due to atomic nuclei. However, the exact forms of T_{n} and E_{xc} are not defined yet.

The Kohn-Sham method (1965) [137] is a practical procedure to get the ground state electron density. It claims that instead of the many-body system of interacting electrons, set of Kohn-Sham orbitals (i.e. wave functions) of non-interacting electrons that move in an effective potential can be defined

$$H_{KS} = T_0(\mathbf{r}) + U_H + U_{xc} + U_{ext}(\mathbf{r}) \tag{2.14}$$

Here, U_{xc} consists of U_{x} that is electron gas, and U_{c} (correlation energy potential). The exchange-correlation potential defines electron-electron interactions. The exchange-correlation potential describes the effects of the Pauli principle and the Coulomb potential beyond a pure electrostatic interaction of the electrons. The exchange-correlation potential is defined by the functional derivative

$$U_{xc} = \frac{\delta U_{xc}[n]}{\delta n} \tag{2.15}$$

Self-consistent field theory algorithm starts with guessing a ground-state density, than computing the Kohn-Sham potential, solving Kohn-Sham equations to obtain

Kohn-Sham orbitals, and finally calculate density from the orbitals. If the result is not converged, repeat an iterative procedure from computing Kohn-Sham potential [139].

To sum up, the Kohn-Sham theory gives an accurate approximation for all terms presented in Schrödinger equation, and it has become widely used approach (DFT) for electronic structure calculations.

2.2.2 LDA and GGA exchange-correlation functionals

The exact functionals for exchange and correlation components are not defined. However, there are local density (LDA) and generalized gradient (GGA) approximations that make it feasible to calculate. The LDA depends only on the density at the position where the functional is evaluated [139]. The LDA approximates the functionals T_0 (or the kinetic energy of a non-interacting electron gas) and U_{xc} (or exchange-correlation) by the corresponding energies of a homogeneous electron gas of the same local density.

The LDA has proven to be a useful approximation. The LDA is able to define a variety of properties such as structure, vibrational frequencies, elastic moduli and phase stability with an acceptable error. However, when computing binding energy the LDA can have significant errors by overestimating the result [137].

GGA is also a local approximation, however, it also takes into account the gradient of the density at the same position. In comparison to LDA, GGA gives a reasonable binding and formation energy estimation. The GGA has been chosen for the calculations in this work because its ability to provide accurate bond lengths for small

molecules.

2.2.3 Pseudopotentials

The Schrödinger equation can be further simplified by dividing electrons into valence and inner core electrons. The electrons in the inner shells are strongly bound and do not play a significant role in the chemical binding of atoms; they also partially screen the nucleus, thus forming with the nucleus an almost inert core. It should be noted that affinity properties are almost completely due to the valence electrons. This statement claims that inner electrons can be ignored, thereby reducing the atom to an ionic core that interacts with the valence electrons. A pseudopotential replaces all-electron interaction by effective interaction (only that the valence electrons feel) [137].

2.2.4 Shortcomings of DFT

However, it needs to be emphasized that although DFT in principle is an exact theory, its functional form is not defined yet. DFT has issues in defining band-gap and neglects strong correlations. Also, DFT is computationally very intensive, therefore, it is not capable to calculate systems with more than few hundreds of atoms as well as for not more than few hundreds of picoseconds simulation time. For modelling large systems, molecular dynamics method has been proved to be more useful.

2.3 Molecular Dynamics (MD) simulations

Theoretical studies require the use of large-scale computer simulations. MD is able to compute macroscopic behaviour of the system using microscopic inputs [141]. In MD, atoms are approximated with mass and charge, and chemical bonds as springs. The atoms in the system interact as classical particles through a potential energy function moving according to Newton's second law [142]. Velocities are often calculated using the velocity Verlet algorithm [142].To run a MD simulation, initial positions $r_0(t = 0)$ and velocities are assigned, and a short time step δt is chosen. The forces acting on each particle in the system are defined from Newton's law of motion

$$F_i = m_i a_i \qquad i = 1, 2, ..., N \tag{2.16}$$

Forces can be also determined as a gradient of the potential energy function:

$$F_i = -\nabla_i U \tag{2.17}$$

at this point the acceleration can be found from

$$-\nabla_i U(r_1, r_2, ..., r_n) = m_i \ddot{r}_i \tag{2.18}$$

Here $r_i = (x_i, y_i, z_i)$ is the vector of Cartesian coordinates of the i atom, $\ddot{r}_i$ is the corresponding acceleration, F_i is the vector of forces acting on the i atom, N is the number of atoms, and ∇ is an operator:

$$-\nabla_i U(r_1, r_2, ..., r_n) = -\left(\frac{dU}{dx_i}, \frac{dU}{dy_i}, \frac{dU}{dz_i}\right) \tag{2.19}$$

The acceleration allows the calculation of new positions of the particle r_{i+1} [143]. The position of the particle at time $(t + \delta t)$ can be determined by position at time t and $(t - \delta t)$, and by the acceleration at time t. Controls for temperature and pressure are applied at this point to keep required simulation conditions [144]. For more details regarding thermodynamic ensembles please refer to the Sec. 2.3.3. After that, the positions and velocities of the particles are updated [143]. The Verlet algorithm, which is simple to implement, accurate and stable, can be explained by the following equations:

$$r_i(t + \delta t) = r_i(t) + v_i \delta t + \frac{1}{2} a(t) \delta t^2 + \frac{1}{6} b(t) \delta t^3 + O(\delta t^4) \tag{2.20}$$

Here **a** is acceleration, and **b** is a third derivative of **r** with respect to **t**

$$r_i(t - \delta t) = r_i(t) - v_i \delta t + \frac{1}{2} a(t) \delta t^2 - \frac{1}{6} b(t) \delta t^3 + O(\delta t^4) \tag{2.21}$$

$$r_i(t + \delta t) = 2r_i(t) - r_i(t - \delta t) + a(t) \delta t^2 + O(\delta t^4) \tag{2.22}$$

$$a(t) = -\frac{1}{m} \nabla U(r(t)) \tag{2.23}$$

$$v_i(t) = \frac{r_i(t+\delta t) - r_i(t-\delta t)}{2\delta t} \tag{2.24}$$

According to velocity Verlet scheme, where positions, velocities and accelerations at time $t + \Delta t$ are obtained at time t in the following way:

$$r_i(t-\delta t) = r_i(t) + v_i(t)\delta t + \frac{1}{2}a(t)\delta t^2 \tag{2.25}$$

$$v_i(t+\frac{\delta t}{2} = v_i(t) + \frac{1}{2}a(t)\delta t \tag{2.26}$$

$$a(t+\delta t) = -\frac{1}{m}\nabla U(r(t+\delta t)) \tag{2.27}$$

$$v_i(t+\delta t) = v_i(t+\frac{\delta t}{2}) + \frac{1}{2}a(t+\delta t)\delta t \tag{2.28}$$

The procedure has to be repeated until the set time is reached.

In classical MD method, the atom-centred point charges replace system of nuclei and electrons. Unfortunately, most potential energy functions are not able to represent chemical reactions, due to its inability to break/create covalent bonds, which limits the use of MD to non-reactive molecular systems. Despite this limitation, MD is found to be an accurate and highly-successful approach for describing protein

folding/unfolding processes [145]. This knowledge can be used for analysis of protein-surface interactions [146], that are found to be critical in choosing of proper candidate material for biomedical applications. MD simulations are a powerful tool that is frequently used to study both structural and dynamical properties of biomolecules. In contrast to experiments, MD simulations are able to provide details on molecular mechanisms of biomolecule behaviour that are inaccessible by experimental tools [147]. At the same time, MD simulations show a good quantitative agreement with experimental results for macro parameters that can be measured.

Today's research of materials for implants is based on trial-and-error method. Instead, we propose to understand protein-surface interactions by using molecular dynamics (MD) simulations to facilitate the design of materials exhibiting improved biocompatible and bioadhesive properties.

MD simulations of the adsorption behaviour of biomolecules at the surface of graphene-based nanomaterials were conducted in this work.

2.3.1 Strengths and limitations of MD

One of the challenges of using MD simulations for protein folding/unfolding modelling is that it requires a great amount of computational resources. Although, MD is computationally much cheaper than DFT calculations, there is always a dilemma in MD calculations between required accuracy and available computational power [148]. The smaller the size of the system, the better degree of freedom can be achieved. MD also fails to reproduce any properties that involve electron transfer, for example, electrochemistry. However, MD approach has been found to be a very popular and

sophisticated tool allowing to understand the general proteins features and behaviour that they exhibit under interactions with the substrates [149]. Accuracy of the MD results depends on the quality of the potential energy function, also called a force field.

2.3.2 Force fields

A force field is a mathematical equation that expresses the potential energy acting on atom as a function of the positions of other atoms [150]. Force field-based methods use higher level of approximation in comparison to *ab initio* (quantum-mechanical) methods. Molecules are represented as set of atoms held together by harmonic, periodic and electrostatic forces. Parameters, such as bond lengths and angles, that are necessary for force fields are derived from *ab initio*, semi-empirical quantum mechanical calculations, as well as from experimental data. The main goal of a force field is to describe all interactions in classical terms. The forces are divided into intramolecular (bonded) and intermolecular (non-bonded) forces operating in a molecular system. As such force fields are simplified models, and their accuracy depends on the quality of parameters from experiment and rigorous quantum-mechanical calculations.

A classical force field consists of internal (bonded) and external (non-bonded) contributions (Fig. 2.2, Eq. 2.29).

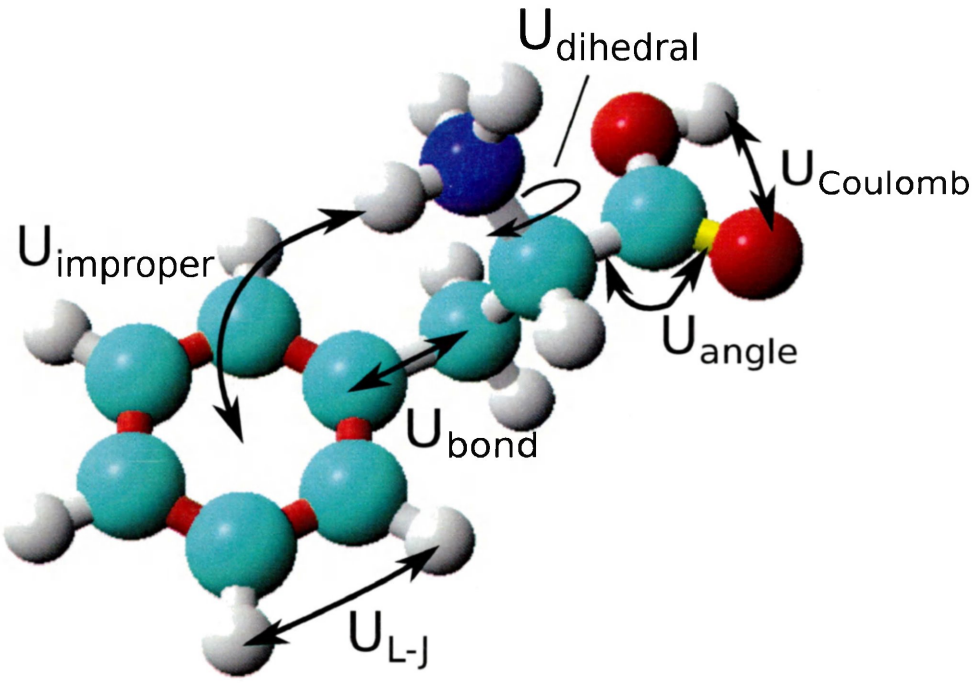

Figure 2.2: Schematic view of bonded and non-bonded forces acting between atoms as an example for the amino acid phenylalanine. The colours refer to an oxygen atom (red), carbon (blue), nitrogen (blue) and hydrogen (white). The bonded interactions are represented by U_{bond} (depends on the distance between two bonded atoms), U_{angle} (calculates based on the angle between three bonded atoms), U_{dihedral} (is torsional rotation of four atoms about a central bond) and U_{improper} (controls the planarity of aromatic rings); the non-bonded interactions include U_{Coulomb} (takes into account electrostatic interactions) and U_{LJ} (is used to compute van der Waals term).

$$E_{\text{total}} = \sum_{\text{bonds}} K_{\text{r}}(r - r_{\text{eq.}})^2 + \sum_{\text{angles}} K_\theta(\theta - \theta_{\text{eq.}})^2 + \sum_{\text{dihedrals}} \frac{V_n}{2}[1 + \cos(n\phi - \gamma)] + \sum_{\text{improper}} K_\chi(\chi - \chi_{\text{eq.}})^2 + \sum_{i<j} \left\{ \varepsilon_{\text{ij}} \left[\left(\frac{R_{\text{ij}}}{r_{\text{ij}}} \right)^{12} - 2 \left(\frac{R_{\text{ij}}}{r_{\text{ij}}} \right)^{6} \right] \right\} + \sum_{i<j} \frac{q_{\text{i}} q_{\text{j}}}{\epsilon r_{\text{ij}}} \quad (2.29)$$

Here, $r_{\text{eq.}}$, $\theta_{\text{eq.}}$, $\chi_{\text{eq.}}$ are structural parameters at equilibrium; K_{r}, K_θ, K_χ are force constants; n is number of particles, γ is phase angle for torsional angle parameters, V_n is torsional barrier height, ε_{ij} is the Lennard-Jones well depth, ϵ is the effective dielectric constant, r_{ij} is the distance between atoms i and j. The force field parameters for bond length ($r_{\text{eq.}}$), bond angles ($\theta_{\text{eq.}}$), torsional angles ($\chi_{\text{eq.}}$) are usually derived from X-ray and neutron diffraction and high level *ab initio* calculations. The force constants are estimated using empirical functions. Interactions between pairs of atoms (ij) separated by more than two bonds are defined by a sum of van der Waals and electrostatic contributions, given by the Lennard-Jones ($R_{\text{ij}}{}^{12}$ and R_{ij}^6 represent repulsion and attraction coefficients, respectively) and Coulomb (atomic partial charges: $q_{\text{i}}q_{\text{j}}$) functions.

The intramolecular forces hold atoms together to form molecules. Bonded contributions are presented by bond stretching, bond bending (angle), dihedral and improper terms between covalently bonded atoms. Bond stretching controls length of covalent bonds. Bond angles keep angle between two bonds at equilibrium. Dihedral term represents force between atoms separated by three bonds. Improper dihedral term keeps the aromatic ring planar and rigid by considering bonds between four

atoms. The intermolecular (non-bonded) terms describe forces between molecules. Protein structural behaviour is affected by bonded force field parameters. However, protein adsorption behaviour is dominated by non-bonded parameters such as van der Waals and electrostatic interactions.

The Lennard-Jones potential accounts for repulsive interactions due to Pauli exclusion Principle as well as attractive van der Waals interactions for atom pairs [151, 152]. The van der Waals interaction arises from the electrostatic interaction between two fluctuating dipoles [153]. Although electrons tend to repel one another due to electrostatic interaction, their movements in the molecules are correlated. Motion of electrons in neighbouring atoms create temporary dipoles of the same orientation, as a result attractive interaction occurs.

Electrostatic interactions are calculated by using Coulomb potentials [154] (see also Chapter 4 Sec. 4.3.2). In order to accurately calculate long-range Coulomb forces in a simulated system, the Particle Mesh Ewald (PME) method was used in this work. The general idea of PME technique is to describe the direct summation of interaction energies between point particles by two summations such as a direct sum of the short-ranged potential in real space (PME part) and a summation in Fourier space of the long-ranged part. The electrostatic interaction energy of a system consisting of N particles can be defined by the sum of the pairwise Coulomb interactions:

$$E = \sum_{i=1}^{N-1} \sum_{j>i}^{N} \frac{q_i q_j}{r_{ij}} \tag{2.30}$$

Here q_i is the charge of the i particle and r_{ij} the distance between the i and j particles. The PME summation method re-expresses E as the sum of three potentials

$$E = E_{\text{real}} + E_{\text{recipr}} + E_{\text{self}} \tag{2.31}$$

Here E_{dir} is a summation over all pairs in real space, E_{recipr} is a summation in reciprocal space and E_{self} is a corrective term that represents the self-energy of the system, respectively [155]. Overall, PME is a sum of a finite number of terms, but this sum converges faster than the Coulomb sum in the real space [156]. Therefore, the same number of terms gives higher accuracy in the case of PME. It is always a finite number of terms, which implies an effective cutoff on the Fourier space. PME gives accurate results; however, PME is computationally expensive requiring $Nlog(N)$ complexity for evaluating electrostatic energies and forces of large MD periodic systems [157].

To prevent edge effects, boundary conditions were applied for each system in this work. Periodic boundary conditions is when a simulation box is surrounded by infinite number of its copies [158]. However, only atoms inside the main simulation cell are explicitly considered.

A large number of force fields have been developed, which differ in the number of bonded and/or non-bonded terms in Eq. 2.29, the exact functional form as well as the force constants. For our purposes, AMBER03 force field was used for all calculations presented in this dissertation. The justification will be discussed in Chapter 3.

The AMBER force field is one of the most widely-used force fields used for all-atom MD simulations of protein behaviour [159, 160]. AMBER force field parameters are derived from experimental as well as *ab initio* data [161, 162]. The AMBER force field is meant for simulations in explicit solvent. This force field is for amino acids and,

therefore, can maintain an accurate description of the simulated system providing realistic protein-substrate, solute-substrate and protein-solute interactions. Other popular force fields include CHARMM [163], OPLS [164], GROMOS [165].

2.3.3 Description of the water models in the force field

It should be noted that in order to get a realistic description of the system in MD, the importance of the chosen water model and simulation conditions can not be underestimated. Water is known to have a profound effect on protein structure, function and stability. The presence of physiological environment is extremely important in modelling the behaviour of biomolecules because of desolvation effect that represents competitive interactions between protein, solute and substrate. There are two types of solvation schemes used in MD simulations: explicit and implicit water models. In implicit models, solvent is represented as a continuous medium instead of individual water molecules [166]. This is a simple, unphysical, but computationally efficient technique. However, explicit hydrogen bonds with water molecules are not accounted for the implicit water model [167]. The second model includes water molecules explicitly. The solvent molecules are described using empirical (based on fitted parameters) or *ab initio* potentials. Although modelling of explicit solvent is computationally more expensive, it gives a realistic physical picture of the system and more accurate results, because it considers the molecular details of each solvent molecules and includes explicit solute-solvent interactions. Although implicit water model saves computational simulation time, the explicit water model was chosen for protein behaviour description in this work due to its ability to realistically reproduce solvent details and properties.

The simple dielectric or implicit model for water, that does not account for its molecular nature, is not able to predict proper protein-surface interactions due to water contribution at the interface. The explicit TIP3P [168] water model was used in this work due to its ability to accurately reproduce thermodynamic properties of water [167].

2.3.4 Thermodynamic ensembles

At each chosen time step, number of particles (N), pressure (P), temperature (T) or energy (E) are calculated to control simulation. An ensemble is a large collection of microscopically defined states of a system, with certain constant macroscopic properties. The monitoring is performed by implementation of thermodynamic ensembles (set of configurations) called NVE, NVT and NPT. Biological systems are subjected to constant pressure more than constant volume. Consequently, NPT ensembles are realistic protein simulations. In this work, the NPT framework, an isobaric-isothermal ensemble, was used, which means that the number of particles, pressure, and temperature are kept constant, while the scaling volume varies; temperature is changed by modifying velocity of particles [144]. The NPT ensemble requires particles to interact with a thermostat and barostat. A barostat is a method when the pressure is weakly coupled to a 'pressure bath' and the volume is periodically rescaled. A number of different barostat techniques exist for maintaining a target pressure by adjusting the simulation volume. A thermostat is a tool that is used to modify the Newtonian MD scheme with the purpose of generating a statistical ensemble at a constant temperature in order to match experimental conditions.

Velocities are described by Maxwell-Boltzmann distribution at a given temperature

$$\mathbf{P}(v_i) = \sqrt{\frac{m}{2\pi k_B T}} \exp\Big(-\frac{m{v_i}^2}{2\pi k_B T}\Big) \tag{2.32}$$

Here, $\mathbf{P}$ is a probability that an atom i has a velocity v_i at a temperature T; k_B is a Boltzmann constant. The aim is to adjust instantaneous temperature by scaling all velocities. The instantaneous temperature can be calculated from the velocities using the relation

$$\frac{3}{2}k_B T_{inst} = \frac{1}{N}\sum_i \frac{1}{2}m{v_i}^2 \tag{2.33}$$

Where, T_{inst} is an instantaneous temperature of the system, which fluctuates according to the amount of thermal energy in the system at any particular time. The rescaling of velocities continue until T_{inst} is equal to required T

$$v_i' = \sqrt{\frac{T}{T_{inst}}} v_i \tag{2.34}$$

$$v_i' = \lambda v_i \tag{2.35}$$

This is an isokinetic thermostat. Linear and angular velocities of the particles in the system are multiplied at periodic intervals by a factor

$$\lambda = \sqrt{1 + \frac{\Delta t}{\tau_T}\Big(\frac{T}{T_{inst}} - 1\Big)} \tag{2.36}$$

Here, T is the set temperature, Δt is the integration time step, τ_T is called 'rise-time' of the thermostat that describes the strength of the coupling of the system to a hypothetical heat bath. The larger τ_T, the longer it takes to achieve a given T after an instantaneous change from some previous T. Repeatedly setting the instantaneous temperature T_{inst} during the simulation and correcting particle velocities, the average kinetic energy can be brought to the constant set point value.

Pressure coupling is usually introduced in the form of the Berendsen thermostat and barostat [169] that rescales the system volume and the atoms coordinates within the simulation box every time step. A global pressure is computed for all atoms. Similarly, when the size of the simulation box is changed, all atoms are re-scaled to new positions. Modifying the box size in one of the coordinate direction in every step guarantees control of pressure during the simulation. In this work, Berendsen barostat and thermostat [169] are used because they are efficient tools for bringing the system to a desired temperature such as they are proven to be good in directing the system close to equilibrium. The Berendsen barostat is analogous to the Berendsen thermostat. The coordinates are scaled at each MD step

$$\mathbf{r}' = \chi^{\frac{1}{3}}\mathbf{r} \tag{2.37}$$

$$\chi = 1 - k\frac{\Delta t}{\tau_P}(P - P_{\text{inst}}(t)) \tag{2.38}$$

where $k = -\frac{1}{V}(\frac{\partial V}{\partial P})_{\text{T}}$ is isothermal compressibility, and τ_{P} is relaxation time for the coupling, P_{inst} is an instantaneous pressure of the system. The Berendsen method drives the system pressure according to equation

$$\frac{dP_{\text{inst}}(t)}{dt} = \frac{1}{\tau_P}(P - P_{\text{inst}}(t)) \tag{2.39}$$

To sum up, ensembles and thermo or barostats are methods to account for the influence of temperature and pressure on atomic motions. Procedures for MD simulations performed in this work will be given in Chapter 3, 4 and 5.

Chapter 3

Simple building blocks at the surface of graphene: significance of solvent and motifs termination

The first study of this thesis is a complete reproduction of the article published in *Journal of Chemical Physics* by the author [170]. None of the work presented in this and the following chapters is exclusively my work. The script utilized to run the calculations was developed by me, and its basic concepts are described in the methods chapter. I participated in system selection, performed the simulations, analyzed the data, created the figures. This chapter provides a validation of the methodology and uncover the significance of desolvation effect for the simulations of all of basic biological molecules. The results presented in this chapter demonstrate that the minimum requirement for protein-surface interactions based on adsorption of single amino acids is to use terminated amino acids as they mimic polypeptide chain.

Favorable adsorption of capped amino acids on graphene substrate driven by desolvation effect

N. Dragneva, W. B. Floriano, D. Stauffer, R. C. Mawhinney, G. Fanchini, and O. Rubel *J. Chem. Phys.*, 139(174711), 2013

3.1 Abstract

The use of graphene-based nanomaterials is being explored in the context of various biomedical applications. Here we performed a molecular dynamics simulation of individual amino acids on graphene utilizing an empirical force field potential (Amber03). The accuracy of our force field method was verified by modelling the adsorption of amino acids on graphene in vacuum. These results are in excellent agreement with those calculated using *ab initio* methods. Our study shows that graphene exhibits bioactive properties in spite of the fact that the interaction between graphene and amino acids in a water environment is significantly weaker as compared to that in vacuum. Furthermore, the adsorption characteristics of capped and uncapped amino acids are significantly different from each other due to the desolvation effect. Finally, we conclude that when assessing protein-surface interactions based on adsorption of single amino acids, the minimum requirement is to use capped amino acids as they mimic residues as part of a peptide chain.

3.2 Introduction

Graphene or a single layer of graphite is considered a promising material for various applications in engineering and medicine [111]. Graphene is a flexible substrate that can be functionalized with peptides, proteins, and small biomolecules [112, 114]. A detailed understanding of protein interaction with graphene may facilitate the development of advanced biological applications such as biosensors for detection of biomolecules [171–179] and living cells [125, 180], drug delivery systems [181], and cell imaging [181–184]. In particular, an insight into molecular mechanisms of the adsorption of plasma proteins on the biomaterial surfaces may help to understand the reasons for foreign body reactions and implant rejection [44]. This is important knowledge as the properties of implanted biomaterial defines safety of the medical device. In addition, the adsorption capacity of graphene oxide functionalized with RNA can be utilized for self-assembling graphene flakes [185] and purifying contaminated drinking water [186]. Therefore, modelling the interactions between graphene and individual amino acids that constitute biomolecules can advance the development of methods for noncovalent functionalization of graphene and its derivatives as well as provide insight into bioactivity of graphene-based materials.

The very first theoretical studies of the interaction between amino acids and graphene were performed in vacuum using density functional theory (DFT) with local and semi-local exchange correlation functionals [187–189]. These methods underestimate the adsorption energy by a factor of 2 to 4 in comparison to results obtained using post-Hartree-Fock methods, such as a second-order Møller-Plesset (MP2) [187, 189]. The reason for the discrepancy is that MP2 provides a more accu-

rate assessment of the van der Waals interaction [187, 189]. These studies have shown that the MP2 perturbation method is able to quantitatively capture the relevant interactions in graphene-amino acid systems.

One of the most comprehensive force field-based molecular dynamic studies of the adsorption energies for 20 proteinogenic amino acids on a graphene sheet in vacuum and aqueous environment was performed by Pandey et. al [190]. Their results for adsorption energy in vacuum reproduce *ab initio* data [187, 189] with a 16% average error. According to Pandey et. al [190], the adsorption energy of an amino acid on graphene is minimally affected by the presence of water (the average change of adsorption energy is less than 1%). However, the definition of adsorption energy used in their work accounts only for the adsorbate-substrate interaction and excludes the solvent contribution. In order for the solute to be considered bound to an interface, a solutes association with the surface and surrounding solvent must be more energetically favorable than when the solute remains solvated in the bulk solution [191, 192]. Desolvation effects are a common phenomenon that governs molecular adsorption at all solid-liquid interfaces. For instance, the affinity of oligopeptides for metal surfaces changes from adsorption in the gas phase to desorption under aqueous conditions [193]. Therefore, neglecting the desolvation effect can lead to a significant error in estimation of binding energies between amino acids and surfaces in general.

Here a detailed theoretical study of the adsorption energies of the 20 proteinogenic amino acids on graphene in vacuum and in explicit water using a force-field molecular dynamics approach is reported. It is shown that the desolvation effect plays an important role in determining the amino acid – graphene interaction. When desolvation is accounted for, the uncapped amino acids do not adhere to the graphene surface,

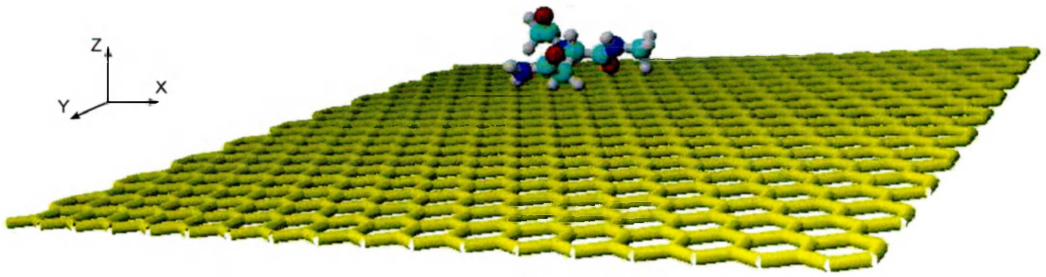

Figure 3.1: Structure of optimized graphene sheet and initial position of Asparagine before molecular dynamics.

which is evident from the fact that they all desorb (i.e., drift by more than 10 Å away from the surface) within the simulation time frame (40 ns). However, when a more realistic capped amino acids model is used, they adsorb to the graphene surface even when desolvation effects are incorporated.

3.3 Method

3.3.1 Graphene structure

A graphene sheet consisting of 720 carbon atoms was constructed with periodic boundary conditions using experimental C-C distance of 1.418 Å [194]. The structure was minimized in vacuum and then kept fixed (Fig. 3.1).

3.3.2 Amino acid structure

The initial (zwitterionic) structures of the 20 genetically encoded amino acids were imported from the YASARA [195] database. Two different forms of amino acids were

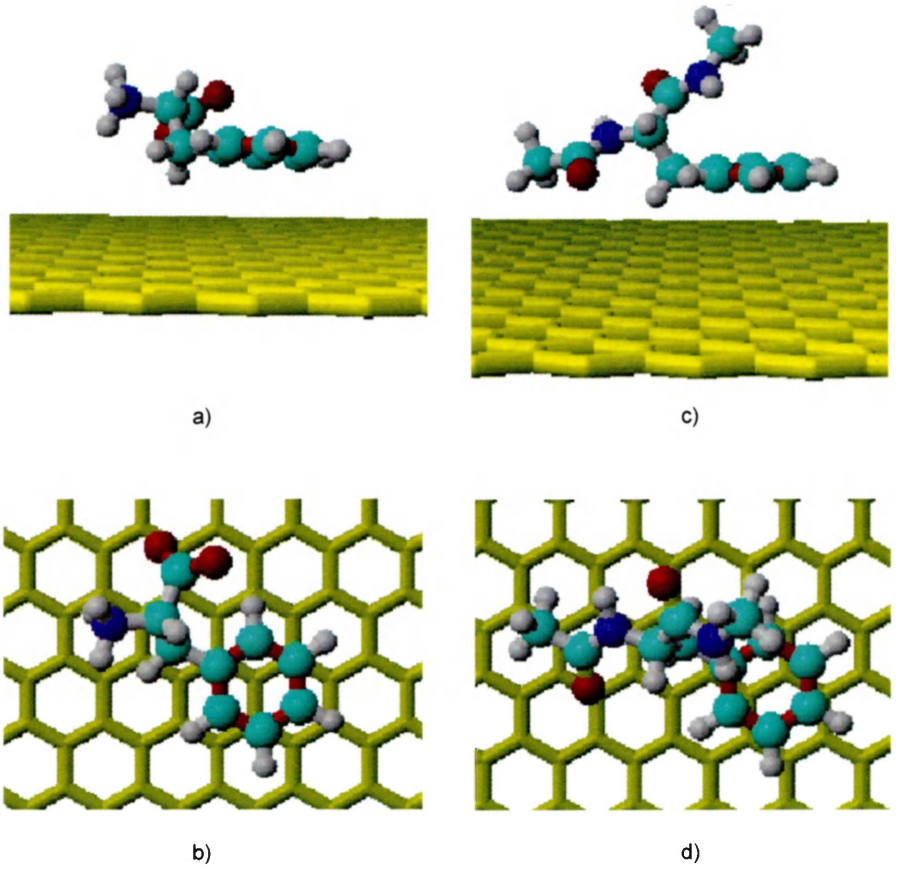

Figure 3.2: Optimized structure of Phenylalanine on graphene in vacuum: uncapped (a,b) and capped (c,d).

considered: capped and uncapped. The uncapped amino acids were used in their zwitterionic form. In calculations of the capped amino acids, the N-terminal of each amino acid was capped with an acetyl group, and the C-terminal was capped with a N-methyl group (Fig. 3.2c and d).

3.3.3 Molecular dynamics

Graphene and each of the 20 proteinogenic amino acids were placed in a simulation cell with dimensions of $44.2 \times 42.5 \times 50$ Å^3. The interaction of 20 amino acids and graphene sheet in vacuum was modeled. Following Qin et. al [188], all 20 amino acids were consecutively put on the top of graphene parallel to the surface because this arrangement was found to be energetically more favorable. Molecular dynamics NPT calculations were performed using the Amber03 force field [196] as implemented in the YASARA package. The default cutoff radius of 7.86 Å was used for dispersion interactions. Long-range Coulomb forces were evaluated using a particle-mesh Ewald approach. Periodic boundary conditions were applied in all directions. The simulation time for molecular dynamics was 40 ns, which is sufficiently long to achieve equilibrium as determined based on the stable values of the potential energies of amino-acid–graphene system. The simulations were performed using physiological pH (7.0), one atmosphere pressure, body temperature (310 K), and the density of water 0.993 g/ml that corresponds to the chosen pressure and temperature. TIP3P water model [168] was used, which implies that the water molecules had a rigid geometry, but were allowed to move in the cell. In order to make solvent parameters closer to human blood, 0.9% of NaCl molecules were added to the cell. The simulation cell size was constrained in the x and y directions, but was unconstrained in the z direction in order to enable the constant pressure control.

3.3.4 Bound and unbound states

In the calculations that represent the bound state of amino acids to graphene, the carbon-α of amino acid was initially placed 3−4 Å above the graphene sheet (Fig. 3.1) and then allowed to relax freely. The unbound state is represented by the corresponding amino acid and the graphene each simulated individually under the same environment and conditions as their bound state. The adsorption energy was calculated as the difference between the sum of the potential energies of the amino acid and graphene in the bound and unbound state, respectively

$$E_{\text{ads}} = \langle E_{\text{a.a.}} + E_{\text{graphene}} \rangle_{\text{bound}} - \langle E_{\text{a.a.}} \rangle_{\text{unbound}} - \langle E_{\text{graphene}} \rangle_{\text{unbound}} \, . \tag{3.1}$$

Here the individual energies of amino acid and graphene include their interaction with the surrounding environment (solvent and counterions). The angle brackets $\langle \ldots \rangle$ represent time averaged values

$$\langle E \rangle = (\tau/\delta t)^{-1} \sum_{i=1}^{\tau/\delta t} E_i \, . \tag{3.2}$$

calculated every $\delta t = 10$ ps over the simulation time frame $\tau = 40$ ns. Here E_i corresponds to a particular energy parameter at the simulation snapshot time $i\delta t$. The average is obtained over 4000 snapshots. The accumulated statistics allows us to determine the adsorption energy with the accuracy of ± 0.007 eV, which is sufficient for the purpose of our study and no further refinement of δt is needed. The equilibration period (approximately 50 ps) was included in the calculation of adsorption energies, which had only minor impact on the final result for the adsorption energy (less than the statistical error of ± 0.007 eV). A negative value of E_{ads} indicates that the solute prefers binding to the surface.

The adsorption energies are slightly sensitive (5% or less) to the chosen initial position of the amino acid with respect to graphene in water. Therefore, two simulations, corresponding to different starting configurations, were performed for each amino acid and the lowest adsorption energy value was selected for further analysis.

3.4 Results and discussion

To validate our method of calculation, adsorption energies of several uncapped amino acids on graphene in vacuum were compared to the *ab initio* data reported by Rajesh et. al [187] and Cazorla et. al [189] (Table 3.1). Our results for the adsorption energy of uncapped amino acids are in good agreement (less than 6% deviation) with *ab initio* calculations. Amber03 adsorption energies for capped amino acids are within 28% average deviation from the previous molecular dynamics simulation using Amber ff99SB by Qin et. al [188] (selected values are shown in Table 3.1). This deviation is likely due to the differences in dihedral potentials and φ/Ψ backbone torsions in Amber03 compared to Amber99SB. Dihedral potentials were fit to new quantum mechanical calculations using a low-dielectric continuum model in Amber03 [196], whereas φ/Ψ backbone torsions were fit to *ab initio* calculations of tetrapeptides in Amber99SB [162].

Table 3.1: Adsorption energy (eV) of amino acids (capped and uncapped) and water molecule on graphene sheet in vacuum calculated using empirical force fields.

Amino acid	Amber ff99SB[1] (capped)	Amber03[2] (uncapped)	Amber03[3] (capped)	MP2 (uncapped)
GLY	−0.34	−0.41	−0.72	−0.38[4]
PHE	−0.78	−0.66	−0.84	−0.62[5]
TRP	−1.01	−0.83	−0.79	−0.84[6]
TYR	−0.87	−0.72	−0.91	−0.76[7]
HIS	−0.73	−0.62	−0.51	−0.55[8]
Water molecule	···	−0.072[9]		−0.103[10]
				−0.174[11]
				−0.250[12]

[1]Ref.[190]

[2]This work

[3]This work

[4]Ref. [189]

[5]Ref. [187].

[6]Ref. [187].

[7]Ref. [187].

[8]Ref. [187].

[9]The corresponding experimental values are 0.105 ± 0.004 eV (Ref. [197]) and 0.097 ± 0.012 eV (Ref. [198])

[10]Ref. [199]

[11]Ref. [200]

[12]Ref. [201]

3.4.1 Capped vs. uncapped amino acids on graphene in vacuum

In order to mimic the behaviour of amino acids as a part of a peptide chain, the ends of the amino acids were terminated with acetyl and methyl groups. The calculated adsorption energies are presented in Fig. 3.3. Since the graphene sheet is neutral, the van der Waals interaction is the main contributor to the adsorption energy followed by Coulomb and bonding terms. Our results suggest that the interaction of capped amino acids with graphene is stronger (with only few exceptions) in comparison to uncapped amino acids. This trend can be attributed to a larger number of atoms in the residue that contribute to the dispersion interaction with the graphene substrate.

Adsorption of small biomolecules on artificial surfaces is often studied using electronic structure methods, such as DFT or post Hartree-Fock techniques. These studies, although more accurate, require large computational resources. The difference in CPU time performance can reach 12 orders of magnitude when comparing MP2 and force field total energy calculation for a medium size of the simulation system ($\sim$100 atoms). Therefore, electronic structure calculations are often performed in a gas phase, i.e. without explicit solvent. Particular examples include studies of the adsorption of amino acids on quartz [202], nickel [203], silica [204], and hydroxyapatite [205]. Attempts to partly account for the solvent contribution by including a limited number of solvent molecules (for instance, 8 water molecules when modelling peptide-hydroxyapatite interaction) are not able to give a realistic description of biomolecule-surface interactions either [206]. Nevertheless, *ab initio* calculations provide an important benchmark for testing the accuracy of empirical potential molecular

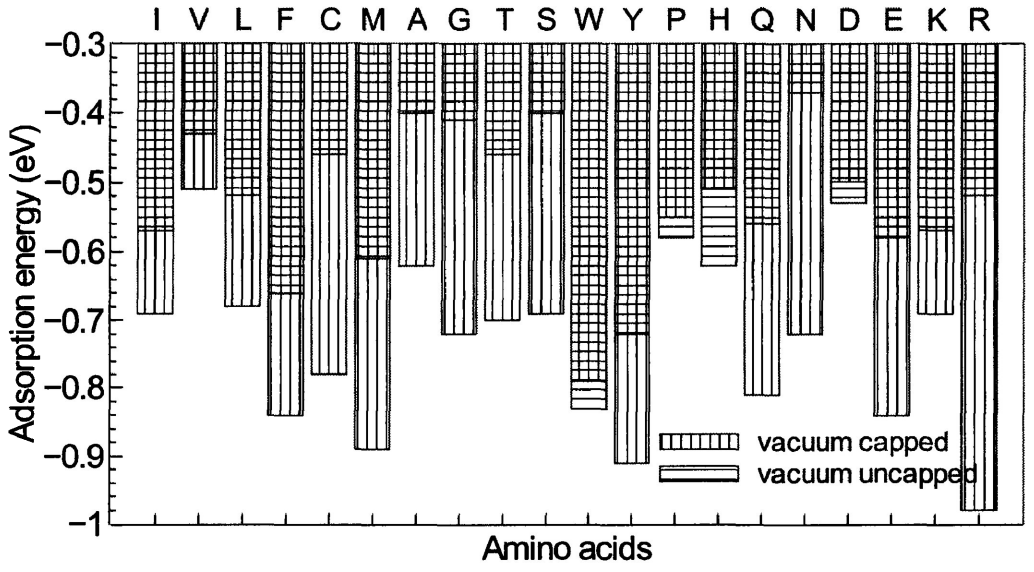

Figure 3.3: Adsorption energy of capped and uncapped amino acids to graphene in vacuum. The amino acids are arranged according to their hydrophobicity index (from most hydrophobic to most hydrophilic). In most cases, the adsorption energies for the capped amino acids are higher in comparison to uncapped due to a larger number of atoms in the residue that contribute to the dispersion interaction with the graphene.

dynamics. Since the natural environment of plasma proteins is aqueous, it is important to investigate how the building blocks of proteins behave on graphene in explicit water.

3.4.2 Capped amino acids on graphene in water

The next step is the simulation of capped amino acids on graphene in aqueous conditions. First, we tested the force-field by calculating the interaction between graphene and water. For this purpose, a single water molecule was placed on the top of graphene in vacuum. The obtained adsorption energy of -0.072 eV is in good agreement with both *ab initio* calculations and experimental values (Table 3.1). Figure 3.4 compares the adsorption energies for single amino acids on graphene in vacuum and in water. The binding affinity of capped amino acids to graphene is reduced in the presence of water on average by a factor of two. The lower values of adsorption energies in aqueous environment can be attributed to a desolvation effect. We anticipate that desolvation effects will also play a profound role in determining the interaction between proteins and graphene substrate as indicated by Camden et. al [207].

The analysis of individual contributions to the adsorption energy indicates that in explicit water, the dispersion component of the amino-acid–graphene interactions is partially compensated by the amino-acid–water interaction, which is not present in vacuum. The adsorption energy consists of three main contributions: van der Waals, electrostatic and bonding terms. The Coulomb component favors solvation of amino acids and amounts to 30% of the dispersion contribution (on average). The bonding terms show an opposite trend with an average magnitude of 15% relative to

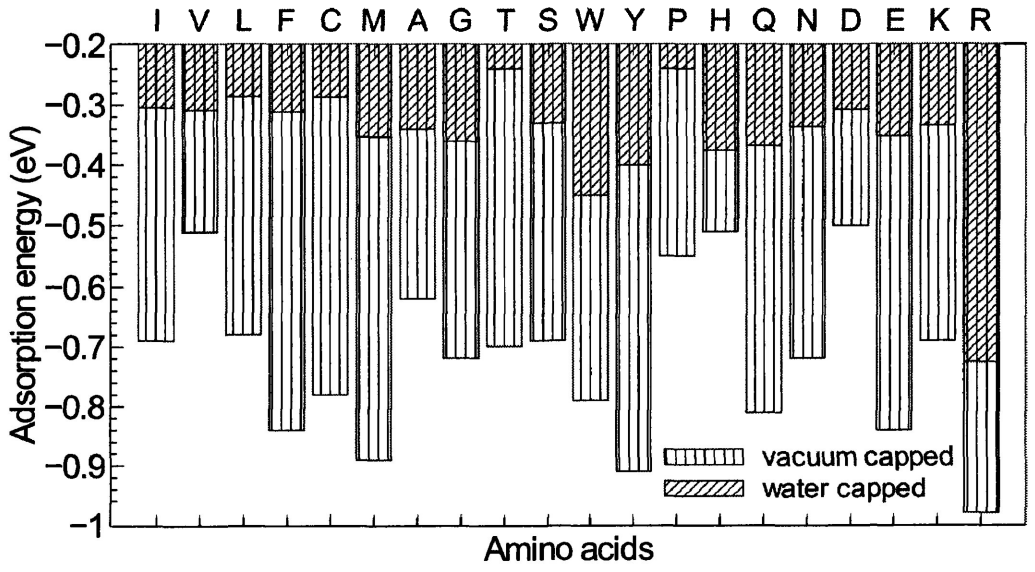

Figure 3.4: Adsorption energy of capped amino acids to graphene in water and in vacuum. The adsorption energies for the capped amino acids in water are significantly lower than that in vacuum because of the desolvation effect presented in aqueous environment.

the dispersion contribution. Therefore, the resultant adsorption energy for capped amino acids in water is mostly governed by the change in the corresponding van der Waals contribution. This contribution correlates with the molecular mass of amino acids as shown in Fig. 3.5.

Our results are also in good agreement with adsorption energies calculated for glycine tripeptides [207]. The adsorption energies of amino acids (as a part of tripeptides G-X-G) on graphene in water was reported very recently in Ref. [207]. When the peptide was constructed from identical amino acids, such as glycine, the reported binding energy of -0.33 eV per one glycine agrees well with our result of -0.36 eV for the capped amino acids. The good agreement here is likely due to a minimal distortion of the peptide chain since all amino acids are identical. However, the adsorption energy of other amino acids as a part of heterogeneous tripeptides are 2-3 times weaker than our data. For example, the adsorption energy of arginine (as a part of G-R-G peptide) is found to be -0.45 eV compared to our result of -0.73 eV. The reduced adhesion can be attributed to additional distortions of the peptide backbone and need to be taken into account at the coarse-grained molecular dynamics level by parametrized angle potentials [208].

3.4.3 Uncapped amino acids on graphene in water

The molecular dynamics trajectories (Fig. 3.6) indicate that uncapped amino acids tend to float away from the surface by the distance more than van der Waals cutoff radius. This behaviour is indicative of the weak binding affinity of uncapped amino acids to graphene. For this reason, the potential energy for the bound state of un-

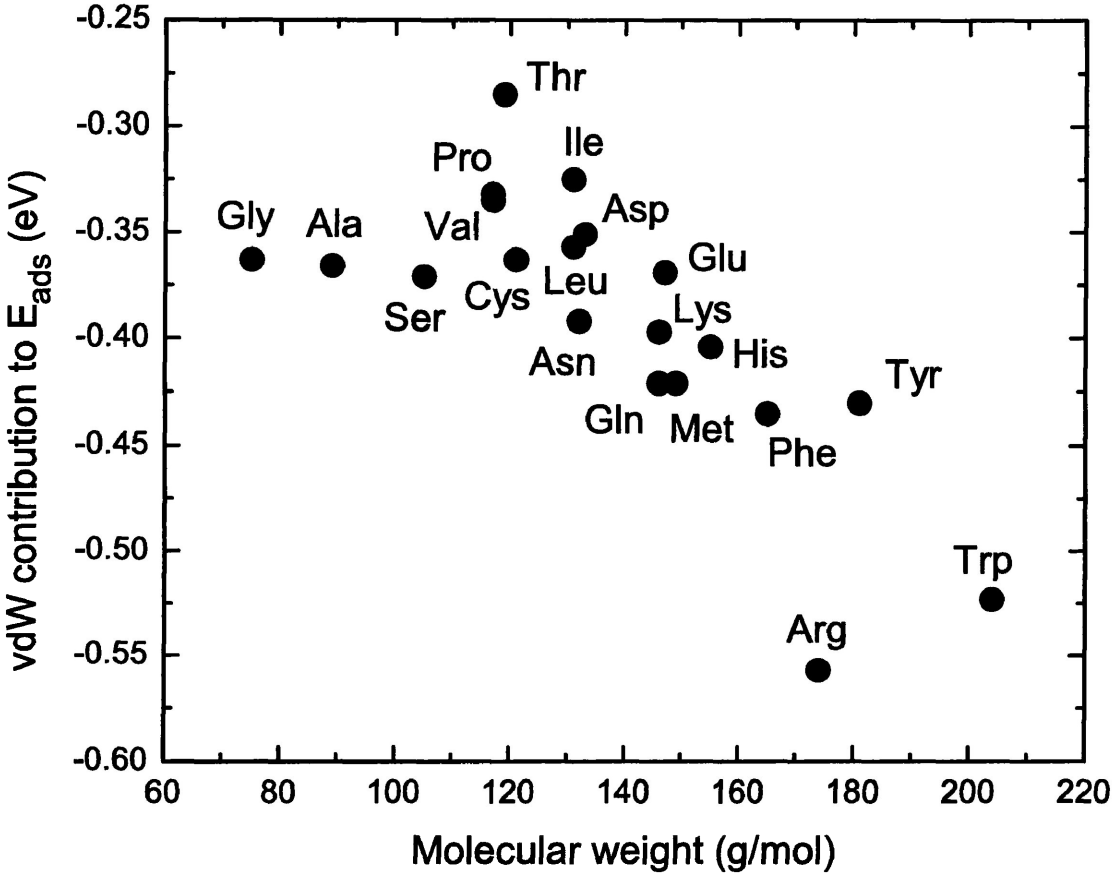

Figure 3.5: The correlation between the amino acid atomic weight and the dispersion (van der Waals) component of the adsorption energy. Results are shown for capped amino acids in water. Larger amino acids exhibit a stronger dispersion interaction with the substrate.

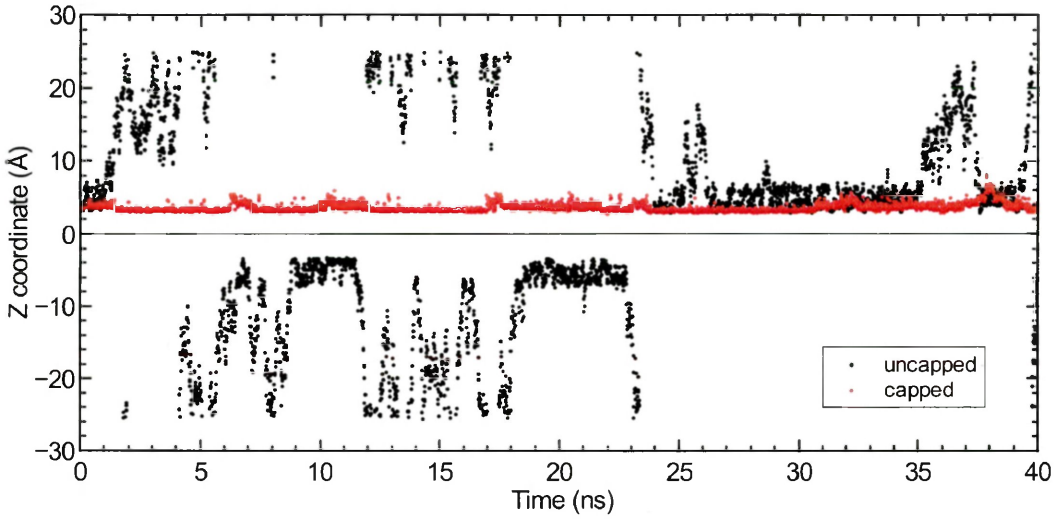

Figure 3.6: Position of carbon-α atom in Leucine (capped/uncapped structure) on graphene sheet in the simulation cell with water. The z-axis is perpendicular to the graphene layer with the origin assigned to the graphene plane. The graph shows that capped Leucine adsorbs to the surface and remains in the bound state during the entire simulation time span. In contrast to that, the uncapped version of Leucine frequently desorbs from the surface, which indicates a weaker adhesion to the substrate. This trend was also observed for the remaining 19 amino acids studied here.

capped amino acids was taken as the average energy during the time periods when the amino acid stays at a distance closer than 4 Å from the surface. It is the weak retention of zwitterionic amino acids that justifies a relatively long simulation time of 40 ns used here in order to ensure that enough statistics is accumulated to represent the bound state.

The reason for preferred solvation of the uncapped amino acid is likely their zwitterionic character. The charges at the terminals of the amino acid prefer the polar water environment instead of the neutral surface of graphene. The interaction of un-

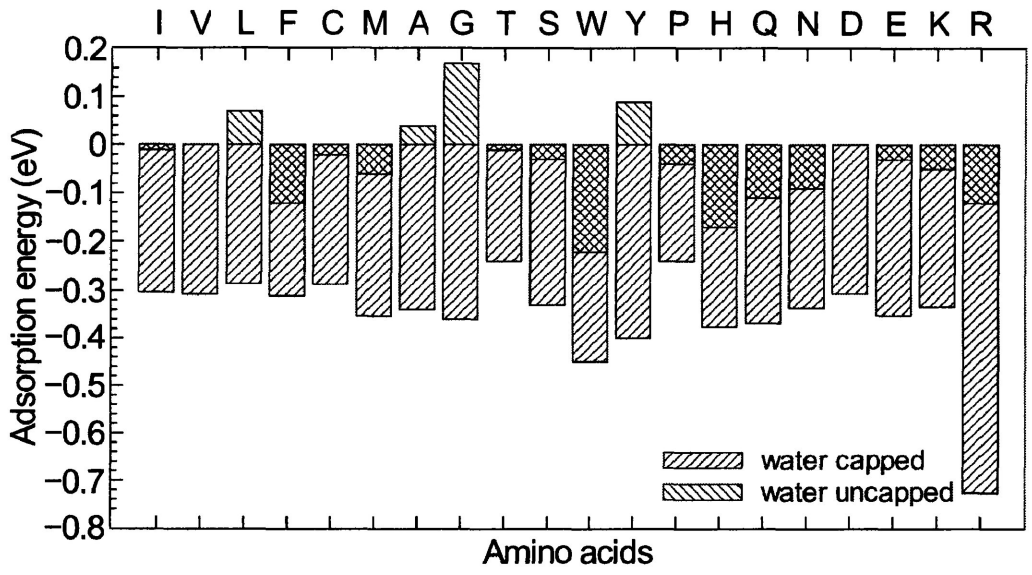

Figure 3.7: Adsorption energy of capped and uncapped amino acids to graphene in water. The uncapped amino acids are unable to bind permanently to the surface of graphene because of the stronger interaction (attractive Coulomb and dispersion interaction of the amino acid) with water competing with the amino-acid–graphene interaction.

capped amino acids with water facilitates increasing the solvent accessible surface area of the zwitterionic dipole [209]. In this case, the attractive Coulomb and dispersion interaction of the amino acid with water dominates over the dispersion component of the amino-acid–graphene interaction. Capped amino acids exhibit an opposite trend, i.e. they adhere to the surface during the entire simulation time (Fig. 3.6). As a result, the adsorption energy for capped amino acids is several times stronger than for uncapped ones (see Fig. 3.7). No correlation is observed between adsorption energy and hydrophobicity index of amino acids, as indicated in Fig. 3.7.

Finally we would like to note that at this level of modelling it is impossible to

conclude on the role of π-electrons in the desorption of the uncapped amino acids from graphene. Although force fields employed in molecular dynamics simulations are capable of describing π-π interactions [210], a quadrupole charge distribution responsible for π-interaction is not explicitly present in the empirical potential model.

3.5 Conclusions

The interaction energy of 20 proteinogenic amino acids and graphene were studied in vacuum and explicit water using the YASARA molecular dynamics package and the Amber03 force field. The proposed method of calculation was justified by comparing the adsorption energies for individual amino acids and single water molecule on graphene with that obtained from first-principle calculations and experiments. Two types of amino acids were modeled: uncapped (zwitterionic form) and capped. The latter form mimics the behaviour of amino acids as a part of a protein and, therefore, provides a more realistic model for describing biomolecular interactions with artificial substrates. Our results suggest that uncapped amino acids do not adsorb to the graphene surface in aqueous environment due to their ionic nature (the average adsorption energy is only -0.04 eV). In contrast, capped amino acids adsorb and remain at the surface of graphene in explicit water. The average adsorption energy of capped amino acids in water is twice lower than that in vacuum. This result can be attributed to a desolvation effect, which is generally expected to reduce the affinity of amino acids to a surface in the presence of solvents. We presume that the desolvation effect will play an important role in protein–graphene interaction studies. The desolvation effect can be further enhanced at the interface between polar solvents and

polar surfaces, such as graphene oxide.

Chapter 4

Development of charge model for graphene oxide, its interactions with amino acids

This chapter is an exact reproduction of an article published in *Journal of Chemical Physics* by Dennis Stauffer et al. [211]. With help of an undergraduate student, Dennis Stauffer, Coulomb potential to reproduce electrostatic potential with DFT was calculated. The script for running the calculations was developed by me, and its basic concepts are described in the methods chapter. I participated in system selection and contributed about half of the data production, data analysis and graphics processing required for this study. This chapter emphasizes the development of an atomic charge model for graphene oxide surface. In addition, it validates the methodology for simulating residues interactions with a graphene oxide sheet.

An atomic charge model for graphene oxide for exploring its bioadhesive properties in explicit water

D. Stauffer, N. Dragneva, W. B. Floriano, R. C. Mawhinney, G. Fanchini, S. French, and O. Rubel *J. Chem. Phys.*, 141(044705), 2014

4.1 Abstract

Graphene Oxide (GO) has been shown to exhibit properties that are useful in applications such as biomedical imaging, biological sensors and drug delivery. The binding properties of biomolecules at the surface of GO can provide insight into the potential biocompatibility of GO. Here we assess the intrinsic affinity of amino acids to GO by simulating their adsorption onto a GO surface. The simulation is done using Amber03 force-field molecular dynamics in explicit water. The emphasis is placed on developing an atomic charge model for GO. The adsorption energies are computed using atomic charges obtained from an *ab initio* electrostatic potential based method. The charges reported here are suitable for simulating peptide adsorption to GO.

4.2 Introduction

Properties of carbon-based nanomaterials in the context of biomedical applications continue to be a subject of extensive research due to the biocompatibility of these materials after functionalization [212]. Graphene-oxide (GO)—or graphene function-

alized with epoxy, hydroxyl, and carboxyl groups—has been shown to exhibit properties that are useful in applications such as biomedical imaging, biological sensors, drug delivery, and biocompatible platforms for cell transfer and growth [90, 114, 213]. However, there is evidence of toxicity in cell-based as well as animal model studies [112, 114, 214]. The ability of GO to trigger adverse reactions when in contact with living tissue remains poorly understood [90]. In order to better assess the potential of GO in biomedical applications, it is useful to investigate its interactions with biomolecules.

Experimental studies report favorable adsorption of individual amino acids, peptides, proteins, and more complex biomolecules on the surface of GO [176, 181, 215, 216]. The adsorption of seven peptides, ranging from 8 to 20 amino acids, to a GO surface was studied experimentally [176] by determining the concentration change in a solution before and after incubation with GO. Out of seven peptides tested, all except two exhibited a high adsorption ratio. This behaviour is in line with the definition of bioadhesion proposed by Woodley et al. [102]: "Bioadhesion means the adherence of molecules (bioadhesives) to biological surfaces. ... bioadhesion does not normally involve the material forming covalent bonds with its target". Another evidence of GO-biomolecules interactions is provided by studying the quenching of an intrinsic fluorescence of isolated amino acids (tryptophan and tyrosine), peptides (amyloid peptide 40 ($A\beta_{40}$) and human islet amyloid polypeptide (hIAPP)), and proteins (Bovine serum albumin (BSA) and human serum albumin (HSA)) [217]. The observed quenching indicates binding interactions between GO and free amino acids Trp and Tyr, the 40 amino acids $A\beta_{40}$ (one Tyr, no Trp), the 37 amino acids hIAPP (one Tyr, no Trp), BSA (two Trp), and HSA (one Trp). It was suggested that the

quenching effect could result from $\pi - \pi$ interactions between Trp/Tyr and GO, similar to what is observed for Trp adsorption to graphene [187], and/or to changes in peptide/protein conformation induced by the GO surface.

The molecular interactions of proteins with synthetic surfaces is a first step in the process of the integration of biomaterials with tissue [218]. Since amino acids are the building blocks of proteins, understanding their individual behaviour on the surface can lead to a better understanding of the protein-surface interactions, and may aid the development of strategies for investigating those interactions. Recent studies showed progress in modelling the adsorption of amino acids and peptides to graphene surfaces such as carbon nanotubes [187], boron-doped carbon nanotubes [181], as well as calcium and hydrogen-doped graphene [189]. To the best of our knowledge, the only available data examining the binding of individual amino acids to GO are from an experimental study in which a mixture of all 20 amino acids was incubated with GO, and the concentration changes of each amino acid were assessed before and after incubation [176]. In this work, we simulate the adsorption of amino acids to GO in order to analyze its potential biocompatibility.

However, a difficulty in the modelling of GO is related to the ambiguity of its structure. Several models for the atomic structure of single hydroxyl or epoxy functional groups on the surface of GO have been proposed in literature. These models include well-established parameters such as bond distances and angles [219–221] as well as the density and spacial distribution of the functional groups [222]. In addition to the structure, it is also important to provide atomic charges that most accurately represent a GO surface in order to capture the electrostatic contributions to the interaction energy. The present work focuses on identifying an atomic charge model

for GO that will provide the most consistent description for studying the interaction between GO and biomolecules in their natural environment (water). First, a method for the development of a charge model for GO based on analysis of the electrostatic potential (ESP) is discussed. In the second part of the work, we report the results of simulations of the adsorption of the 20 proteinogenic amino acids onto the surface of GO using the atomic charges developed in this study. Simulations are performed using a force-field molecular dynamics approach in an explicit aqueous environment. The obtained adsorption energies are in line with the only available experimental data [176] and consistent with other theoretically computed results [223, 224]. We show that the binding affinity of amino acids to the GO surface is slightly greater than to a pristine graphene surface. These results indicate that GO and graphene may exhibit similar bioadhesive characteristics.

4.3 Method

4.3.1 First principle calculation of electrostatic potential

A layer of GO was constructed with 60 carbon atoms arranged in a honeycomb pattern using an experimental value for the nearest-neighbor distance of 1.418 Å [194], resulting in a 12.280×12.762 Å^2 block. Single epoxy and hydroxyl functional groups were placed at the surface as illustrated in Fig. 4.1. Periodic boundary conditions were applied in all three directions. GO layers were separated in the z-direction by adding a vacuum of 16 Å.

The electronic structure calculations were performed in the framework of den-

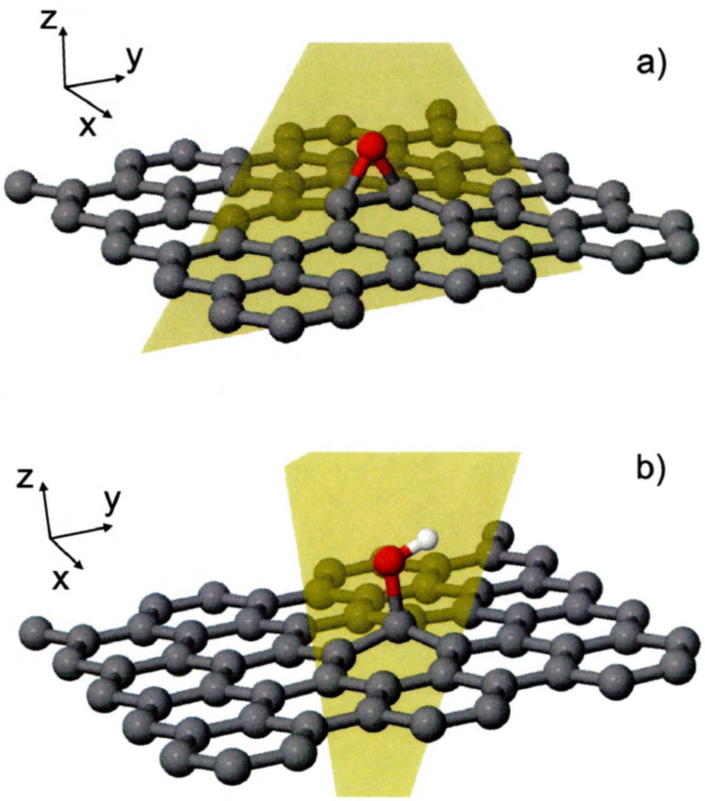

Figure 4.1: Structural model of (a) epoxy and (b) hydroxyl functional groups at the surface of graphene used to determine point charges. Calculations of the electrostatic potential were performed within the yellow plane passing through the centres of C-O-C and C-O-H atoms in the case of epoxy and hydroxyl functional groups, respectively.

sity functional theory (DFT) implemented in the ABINIT package [225, 226]. A plane wave basis set with a cutoff energy of 30 Ha was used in conjunction with Troullier-Martins pseudopotentials [227]. Perdew-Burke-Ernzerhof generalized gradient approximation was employed for the exchange-correlation functional [228]. The reciprocal space was sampled with a single k-point. A special distribution of the electrostatic potential was obtained by subtracting the exchange-correlation potential from the total Kohn-Sham potential. To confirm the completeness of the chosen basis set, a convergence test was performed for the water molecule in vacuum by computing its geometry, the electrostatic potential in the vicinity of the molecule, and the dipole moment. Less than 1% variation was observed when comparing the characteristics obtained using cutoff energies of 30 and 50 Ha.

The full relaxation of internal degrees of freedom was performed by minimizing the Hellmann-Feynman forces acting on individual atoms below 5×10^{-4} Ha/Bohr. The obtained structure and geometry of the functional groups on the GO surface is consistent with *ab initio* calculations reported elsewhere [220, 229].

4.3.2 Point charge model

The point charges for the functional groups of the GO surface were chosen to reproduce the electrostatic potential (ESP) calculated with DFT. This approach is known in literature as the ESP charge model [230–237]. The Coulomb potential was calculated at grid points with a spacing of 0.05 Å on a two-dimensional plane constructed as shown in Fig. 4.1. The electrostatic potential at point $\mathbf{r}$ due to a point charge distribution is evaluated as

$$V(\mathbf{r}) = \sum_i \frac{q_i}{4\pi\varepsilon_0 |\mathbf{R}_i - \mathbf{r}|} \tag{4.1}$$

where ε_0 is the permittivity of free space, q_i and $\mathbf{R}_i$ are the point charge and the position vector of atom i, respectively.

A least-squares algorithm was employed to determine a set of charges that most accurately reproduces the ESP within a region of interest [238, 239]. The region of interest included grid points located at a distance of $1.5 \leq R \leq 5$ Å from atoms in the functional group as well as bonded carbon atoms (Fig. 4.2, Fig. 4.3, Fig. 4.4). The lower bound excluded points within the van der Waals radius of each functional group atom [235]. It was also the shortest distance for non-bonded interactions between the atoms of the amino acid and of the GO surface observed in our simulations. The upper bound was the distance beyond which the Coulomb potential of the functional group was less than 0.01 Ry/e [240]. The zero net charge imposed an additional constraint $\sum_i q_i = 0$. Atomic charges were assigned only to atoms in a functional group and carbon atoms directly bonded to the functional group. Other neighbouring carbon atoms were given no charge, as it was found by Li et al. [241] that the charge is mostly localized at the carbon atoms bridged to the oxygen atom. We assume that the charge values of functional groups do not affect the charge values of neighboring functional groups [119, 242]. The difference in charges for the functional groups obtained with the two-dimensional model and with a three-dimensional model was less than 5%. This difference can be considered negligible for the purpose of our simulations. An identical procedure was used to calculate ESP point charges for a single water molecule in vacuum.

All ESP charges were then scaled up by a factor of 1.5 in order to match the charges

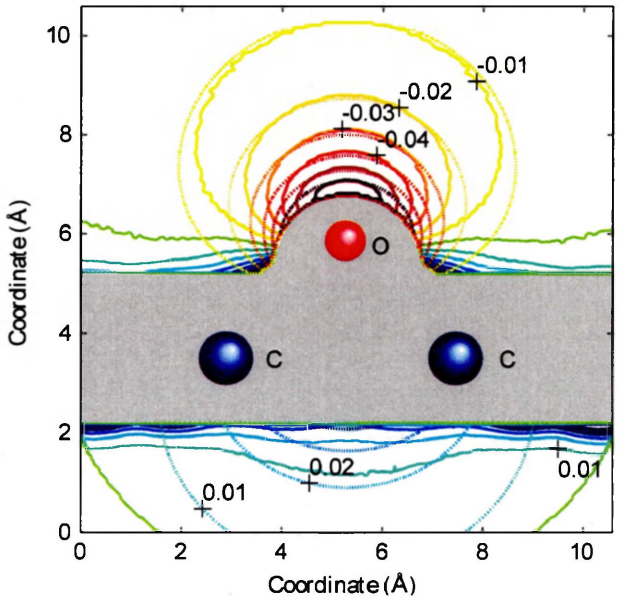

Figure 4.2: Electrostatic potential (Ry/e) calculated with DFT (solid contours) and obtained from the ESP point charge model (dashed contours) for an epoxy functional group. Contour lines are shown within the region of interest discussed in the text. The shaded area depicts the excluded region with the proximity of less than 1.5 Å to atoms.

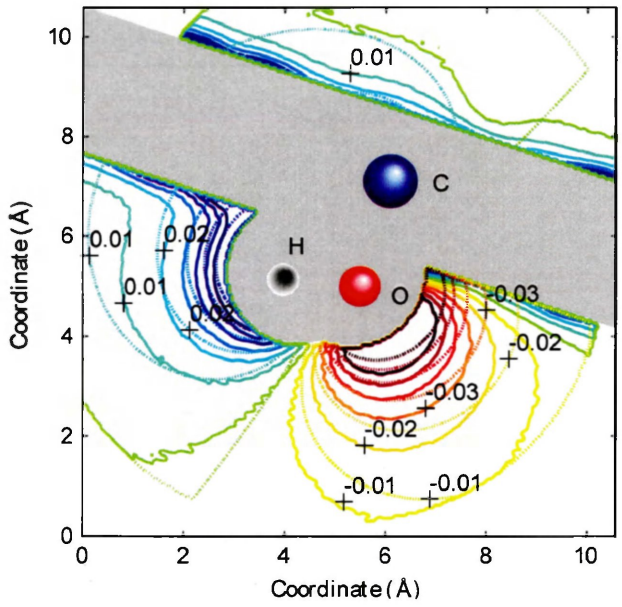

Figure 4.3: Electrostatic potential (Ry/e) calculated with DFT (solid contours) and obtained from the ESP point charge model (dashed contours) for a hydroxyl functional group. Contour lines are shown within the region of interest discussed in the text. The shaded area depicts the excluded region with the proximity of less than 1.5 Å to atoms.

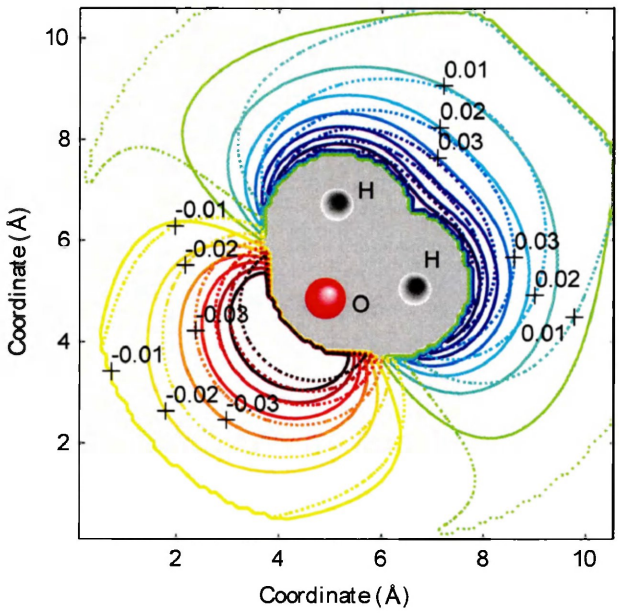

Figure 4.4: Electrostatic potential (Ry/e) calculated with DFT (solid contours) and obtained from the ESP point charge model (dashed contours) for a water molecule. Contour lines are shown within the region of interest discussed in the text. The shaded area depicts the excluded region with the proximity of less than 1.5 Å to atoms.

of the TIP3P water model (see Sec. 4.4.1), which is included in the Amber03 force-field and accurately reproduces the dipole moment as well as other thermodynamic properties of water [243–245]. This method was originally introduced in Ref. [231]. The charge correction accounts for the polarization effect of an aqueous environment [230, 231, 234, 244], which leads to an increase in the experimental dipole moment of liquid water as compared to its gaseous state [234, 246]. It is the scaled charge model (abbreviated as SESP) that will be used later in the modelling of GO.

4.3.3 Graphene oxide structure

The GO structure used in the molecular dynamics simulation was a 38×50 Å^2 section of graphene functionalized with epoxy and hydroxyl groups. The model consisted of a lattice of 768 carbon atoms with 96 hydroxyl and 60 epoxy groups distributed on both sides of the surface. A carbon to oxygen atom ratio of 5:1 and a hydroxyl to epoxy group ratio of 3:2 was chosen in accordance with the GO model proposed by Bagri et al. [222]. The spatial distribution of the functional groups was also taken from Bagri et al. [222]. The GO surface was built by repeating the unit cell shown in Fig. 4.5. The initial geometry for the functional groups was based on the works of Yan et. al. [229] and Xu et. al. [220]. The bond distance between carbon atoms was initially set at 1.418 Å (Fig. 4.5). In the hydroxyl group, the initial C-O bond length was 1.47 Å, the O-H bond length was 0.98 Å, and the C-O-H bond angle was 107.9°. For the epoxy group, the C-O bond distance was 1.44 Å, and the C-O-C bond angle was 63.9°.

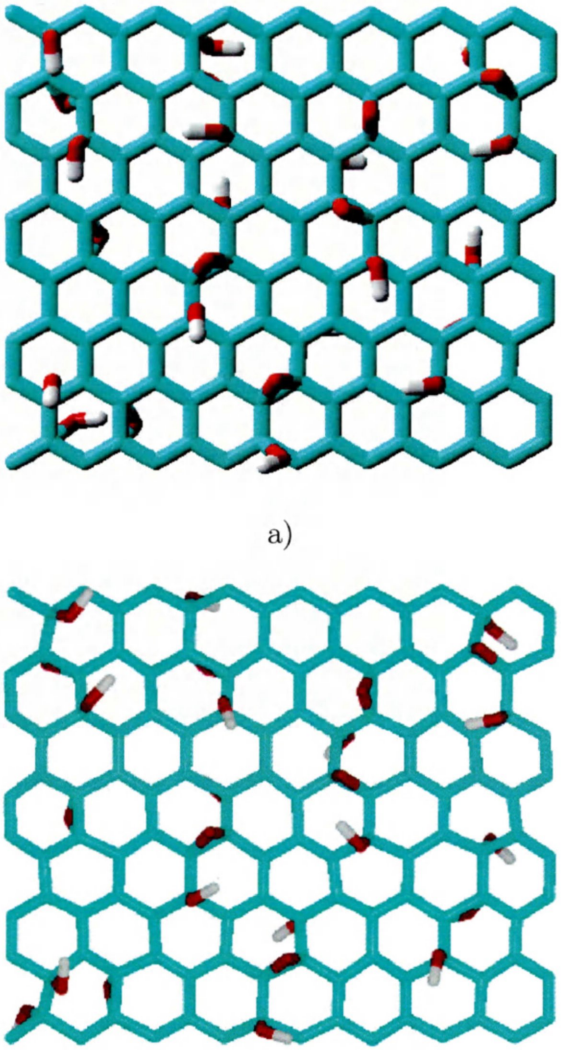

a)

b)

Figure 4.5: The unit cell of the GO surface used for the simulation (a) before and (b) after minimization. The carbon atoms are shown in blue, the oxygen atoms in red, and the hydrogen atoms in white. After minimization, the cell shows some distortion due to the lengthening of the bond between the carbon atoms bound to the epoxy groups. The positively charged hydrogen atoms in the hydroxyl groups cause them to orient towards the negatively charged epoxy groups.

4.3.4 Molecular dynamics simulation

GO and each of the 20 proteinogenic amino acids were placed in a simulation cell with dimensions of $38 \times 50 \times 60$ Å^3. Periodic boundary conditions were applied in all directions. Each amino acid was placed on the GO surface and the resulting system was energy-minimized in vacuum. This minimized structure was solvated with explicit water and used as the starting configuration for MD simulations. To mimic the behaviour of the amino acids as a part of a peptide chain, the ends of the amino acids were terminated with acetyl and methyl groups, which is a recently proposed procedure for modelling amino acids [170, 190]. All 20 amino acids were consecutively placed on the top of GO with the longest axis parallel to the surface because this arrangement was found to be energetically more favorable [188]. Molecular dynamics NPT calculations were performed using the Amber03 force field [196] and the TIP3P water model [168] as implemented in the YASARA package [195].

The simulations were carried out using the same methodology as in our previous study [170]. The simulation time for molecular dynamics was 40 ns, which is sufficiently long to achieve equilibrium as determined by stable values for the potential energy of the amino-acid–GO system. The simulations were performed using physiological parameters, such as 1 atm. pressure, body temperature (310 K), and the standard sodium chloride concentration of blood (0.9%).

In the calculations that represent the bound state of the amino acids to GO, the carbon-α atom of the amino acid was initially placed $3-4$ Å above the GO sheet and then the whole amino-acid–GO system was allowed to relax freely. The unbound state is represented by the corresponding amino acid and GO each simulated individually

in the same environment and under the same conditions as the bound state. The adsorption energy was calculated as the difference between the sum of the potential energies of the amino acid and GO in the bound and unbound states, respectively

$$E_{\text{ads}} = \langle E_{\text{a.a.}} + E_{\text{GO}} \rangle_{\text{bound}} - \langle E_{\text{a.a.}} \rangle_{\text{unbound}} - \langle E_{\text{GO}} \rangle_{\text{unbound}} \tag{4.2}$$

Here the individual energies of the amino acid and GO include their interactions with the surrounding environment (solvent and counterions). The angle brackets $\langle \ldots \rangle$ represent time averaged values obtained with the same method as in our previous study [170].

The adsorption energies were sensitive (up to 10% variation) to the initial position of the amino acid with respect to the GO surface. Therefore, a minimum of three simulations, corresponding to different starting configurations, were performed for each amino acid. The average of the adsorption energies of each amino acid over multiple simulations was calculated. Additional simulations were performed when needed to reduce the variation of the average adsorption energy to less than 0.05 eV.

4.4 Results

4.4.1 Atomic point charge model for graphene oxide

Since molecular dynamics simulations are strongly influenced by the choice of atomic point charges [247], we present a rigorous method for determining the partial charges of GO. The point charges calculated from *ab initio* electrostatic potential (ESP) are

summarized in Table 4.1 along with the results obtained using alternative methods. The atomic charge of $-0.56e$ for the oxygen atom was found to best reproduce the electrostatic potential in the vicinity of the water molecule. The point charge for oxygen in the hydroxyl group has a lower value of $-0.38e$ in comparison to that in water. This result can be attributed to the higher electronegativity of carbon in comparison to hydrogen. For to the same reason, the charge of oxygen in the epoxy group is even weaker ($-0.24e$).

It should be noted that the point charge obtained for oxygen in water is about 15% weaker than other *ab initio* ESP charges reported in the literature [248] (see Table 4.1). In order to elucidate the reason, we computed the dipole moment of a water molecule using the *ab initio* electron density (not the point charges) in the framework of the modern theory of polarization (Berry phase) [249]. The resulting dipole moment of 1.83 D agrees well with the experimental value of 1.86 D for a water molecule in the gas phase [250], which gives us confidence in the calculated electron density and resulting potential. The discrepancy between *ab initio* ESP charges may therefore be attributed to differences in the definition of the region of interest and the distribution of sampling points (Sec. 4.3.2).

Table 4.1: Partial charges (in units of the elementary charge) for the water molecule as well as epoxy and hydroxyl groups of GO determined using various charge models.

Functional group or molecule	Atom	Charge model			
		ESP (this work)	SESP (this work)	RESP [1]	Modified AM1-BCC [2]
Water molecule	O	−0.56	−0.84	−0.68	−0.834
	H	+0.28	+0.42	+0.34	+0.417
Epoxy	O	−0.24	−0.36	···	−0.36
	C	+0.12	+0.18	···	+0.18
Hydroxyl	O	−0.38	−0.57	···	−0.58
	C	+0.12	+0.18		+0.16
	H	+0.26	+0.39		+0.42

[1]Based on *ab initio* (MP2/aug-cc-pV6Z) electrostatic potential in conjunction with the RESP algorithm (Ref. [248])

[2]AM1-BCC charges corrected with known RESP charges for related functional groups Ref. [159, 160]

In molecular dynamics simulations of molecular adsorption at the solid-liquid interface, solute-solvent and substrate-solvent interactions play an important role [191, 251]. Therefore, special care should be taken in choosing a *mutually compatible* charge model for both solute and solvent. The YASARA software package with the Amber03 force field was chosen for the simulations because of its accuracy in modelling organic molecules in an aqueous environment [150]. This force field uses the TIP3P water model, which is a non-polarizable three-point water model [168]. The partial charges are fixed at the value of $-0.834e$ for the oxygen atom (Table 4.1) and are not affected by proximity to other molecules [230]. The increase in the charge value relative to the gas phase is due to the polarization effect present in liquid water, which is implicitly included in the TIP3P model [234]. However, the ESP-derived charges for GO do not account for the charge increase due to polarization, which leads to an underestimation of the strength of the electrostatic interactions at the solute-solvent interface [244].

This inconsistency can be resolved by the use of linearly scaled atomic point charges. The ESP-charges calculated in our work were scaled by a factor of 1.5 in order to match the charges on the TIP3P water model. The scaling factor is the ratio of the atomic charge on the oxygen atom of the TIP3P model ($-0.834e$) to the atomic charge for the oxygen atom in a water molecule calculated by the method described above ($-0.56e$). The scaled charges are listed in Table 4.1 under the SESP charge model. The scaling accounts for the additional polarization induced by the aqueous solution and ensures compatibility of the SESP atomic charges with the TIP3P water model. The polarization effects are also implicitly built into the charges employed by the AMBER force field for parametrization of amino acids. By applying

the uniform scaling factor we essentially imply that identical elements with identical hybridization (e.g., hydrogen in water and in the hydroxyl group) exhibit identical atomic polarizability [252] resulting in a similar dipolar enhancement produced by the polar solvent.

Finally, we ensure that the proposed charges for the GO surface are compatible with the charge model that is used in our simulation to assign partial charges in unparameterized substrates. For this parametrization, YASARA relies on an `autoSMILES` program that uses the AM1-BCC algorithm [159] combined with known RESP charges [238]. The use of AM1-BCC charges in conjunction with the TIP3P water model has been show to accurately reproduce experimental values for hydration free energies of certain compounds [253]. This approach also reproduces TIP3P charges for the water molecule (Table 4.1). The atomic charges generated by the `autoSMILES` code are listed in Table 4.1 under "Modified AM1-BCC". Their close agreement with SESP atomic charges gives us confidence in the compatibility of the charge models employed for the solvent, solute, and surface in this study.

4.4.2 Adsorption of amino acids on graphene oxide

Once point charges were assigned to all functional groups, an energy minimization for the GO surface was performed in vacuum. After minimization, the surface had an undulating (sinusoidal) shape, which agrees with the model suggested by Tung et al. [254]. This non-planar shape can be explained by the electrostatic interactions between the functional groups attached to the surface as well as the change in coordination, from sp^2 to sp^3, for the carbons attached to the functional groups [255]. The

bond distances and angles of the functional groups remained in good agreement with values calculated with DFT [176, 220, 256]. By giving a three-dimensional computer-generated molecular model of GO and chemically converted graphene, the authors suggest that the removal of the -OH and -COOH functionalities upon reduction of GO restores the planar structure of the graphene surface.

Next, we simulated the adsorption of individual capped amino acids on the surface of GO in water. The corresponding average adsorption energies E_{ads} for each 20 capped amino acids obtained with the SESP charges are shown in Fig. 4.6. The average adsorption energy values are also presented in the Table 4.2 in Sec. 4.7. Overall, the adsorption of all amino acids on the surface of GO was energetically favorable, which is indicative of bioadhesive properties of the GO substrate. The adsorption energies of the amino acids on GO are 25% stronger (on average) in comparison to their adsorption energies on graphene [170].

In order to better understand the origin of bioadhesive properties of GO, we split E_{ads} into two components: solute $\langle E_{\text{a.a.}}\rangle_{\text{bound}} - \langle E_{\text{a.a.}}\rangle_{\text{unbound}}$ and surface $\langle E_{\text{GO}}\rangle_{\text{bound}} - \langle E_{\text{GO}}\rangle_{\text{unbound}}$ contributions. The adsorption of amino acids on GO is primarily driven by the favorable interaction energy of the solute with the surface and with the environment. The amino acid contributes more than half to the total binding energy, as it is shown at the Fig. 4.8 in Sec. 4.7, and defined by the Eq. (5.1). Among various energy components (van der Waals, Coulomb, bond stretching, angle, dihedral, and planarity), the van der Waals contribution prevails in the adsorption energy (see Sec. 4.7 - Fig. 4.9). The van der Waals component correlates with the size of the amino acid: the larger the amino acid, the stronger the dispersion contribution to E_{ads} [170, 224] (see Fig. 4.10 in Sec. 4.7). In contrast, the Coulomb component,

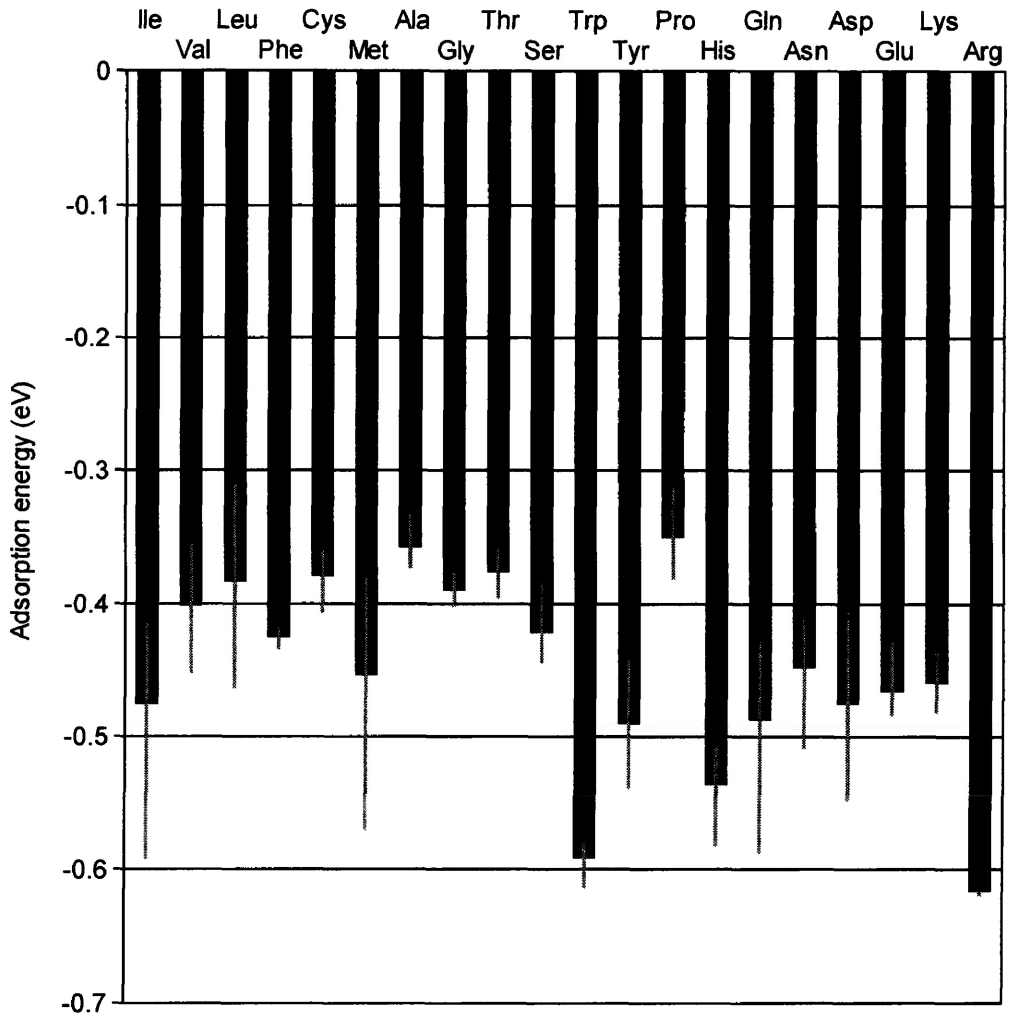

Figure 4.6: Adsorption energies for 20 amino acids on the surface of GO calculated with the SESP charge model. The amino acids are arranged according to their hydropathy index. The data represent average values over multiple simulation runs with the grey error bars corresponding to minimum and maximum adsorption energies. In spite of the various adsorption strength, all amino acids remained bound to the surface within 99.7% of the simulation time.

which can be attributed to the presence of polar groups at the GO surface as well as in the amino acids, favours solvation of amino acids and disfavours their binding to the surface.

4.5 Discussion and comparison with experiments

Comparison of the binding affinity of amino acids to the GO surface with their binding affinity to other biomaterials could provide further insight into the potential biocompatibility of GO. Materials such as gold and hydroxyapatite have been used in medical and, particularly, in dental devices as coatings for biomedical implants [223, 224]. According to Pan et al. [223], B3LYP calculations show that glycine readily binds to hydroxyapatite in water. Our results also show that amino acids favor binding to the GO surface over remaining in water, indicating the potential for GO to exhibit bioadhesive features similar to hydroxyapatite. In another study, Feng et al. [224] calculated the adsorption energies of the twenty amino acids to a gold surface with molecular dynamics using the CHARMM force field. The relative binding energies are similar to our results, with stronger energies for large amino acids, such as arginine, tryptophan, glutamine, methionine, asparagine, and tyrosine; and weaker energies for amino acids with smaller side chains, such as threonine, glycine, and alanine [224]. The similarities in the adsorption behaviour of the amino acids to GO and to gold suggest similar bioadhesive characteristics for the two surfaces.

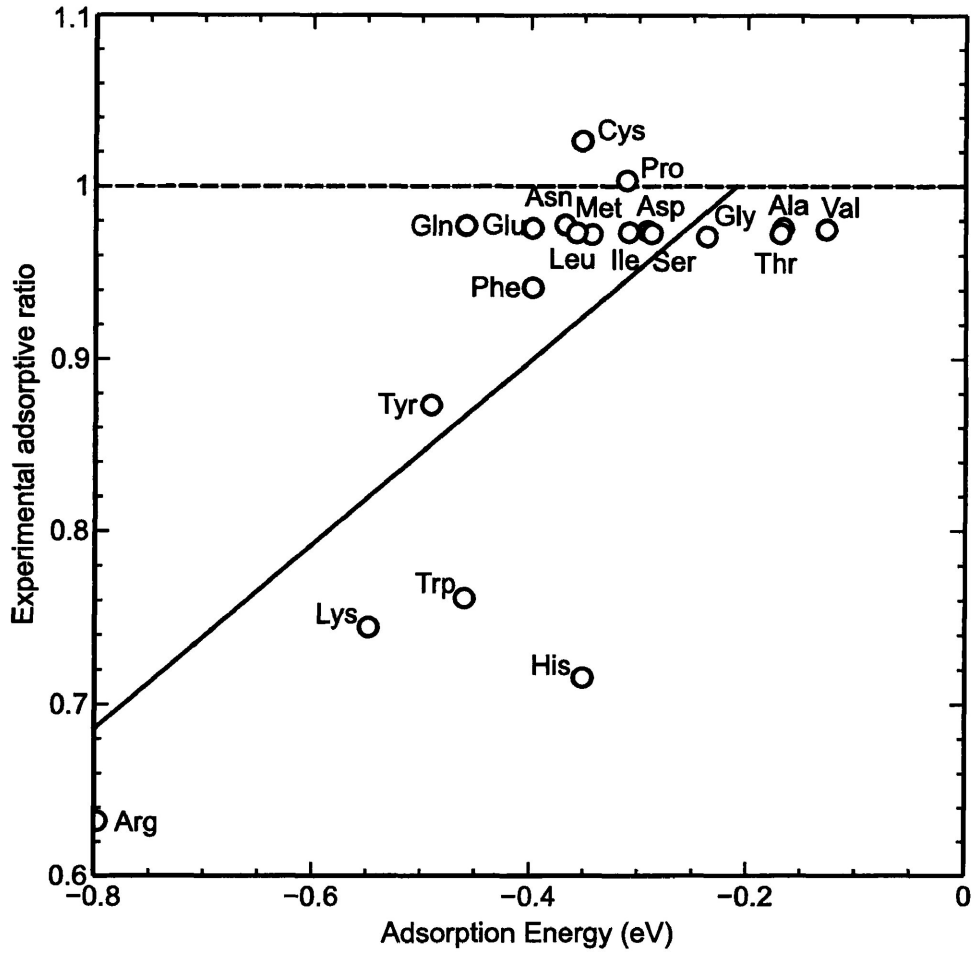

Figure 4.7: Correlation of adsorption energies of uncapped amino acids at the surface of GO to the corresponding experimental adsorptive ratio [169]. Linear fit represents a general trend. The dashed line shows the upper limit in the ratio of the non-bound amino acids according to experimental results.

4.5.1 Adsorption of individual amino acids

Experimental literature reporting a quantitative evaluation of amino acid – GO interactions is scarce. To the best of our knowledge, the most comprehensive study was performed by Zhang et al. [176]. The authors examined the binding of twenty uncapped amino acids to a GO surface by recording an adsorptive ratio, i.e., the ratio of the concentration of each amino acid in solution before and after incubation with the GO surface. A lower ratio for an individual amino acid indicates stronger binding to the GO surface.

Figure 4.7 shows the correlation between our calculated adsorption energies for uncapped amino acids and the experimental adsorptive ratios reported by Zhang et al. [176]. The coefficient of determination for the linear regression fit to the data in Fig. 4.7 is $r^2 = 0.50$. This indicates that our model captures the general trend, i.e., stronger adsorption energies correspond to lower experimental adsorptive ratios. Approximately 50% of the variation in the data is not accounted for by the linear regression model. The experimental ratios for the 14 non-binding amino acids are close to 1, whereas the adsorption energies calculated for the corresponding amino acids in our simulations follow a continuous distribution. Comparison of the experimental adsorptive ratios and our adsorption energies is also effected by structural differences between the GO used experimentally by Zhang et al. [176] and the GO model in our simulations.

The present work is focused on the modelling of a high-quality, idealized GO structure with epoxy and hydroxyl functional groups at the surface (Fig. 4.5). However, structural defects (such as vacancies) can be present in experimental GO samples as

governed by specifics of the production technique [257, 258]. In particular, carboxyl groups, which decorate the edges of GO fragments, can also be present near vacancies within the basal plane [259]. These carboxyl groups are negatively charged and, therefore, are highly reactive at physiological conditions. Experimentally [176], positively charged amino acids (Arg and Lys) exhibit the highest affinity to GO surface followed by aromatic amino acids (Trp and Tyr). In our calculations, the protonated residues favorably interact with the epoxy and hydroxyl groups at the surface. The attractive electrostatic interaction with carboxyl groups present at defects and edges of the surface would contribute further to the favorable binding between GO and positively charged amino acids. GO-amino acid interactions are also influenced by the density of functional groups on the GO surface. The graphene oxide used in the experiment by Zhang et al. [176], which was produced by the modified Hummer's method [260], has a carbon to oxygen atomic ratio of 1.78:1 [261], compared to a C:O atomic ratio of 5:1 in our GO structure [222]. By taking into account this difference in the density of functional groups, as well as the effects of charged edges and/or defects and the synergetic interactions of multiple types of amino acids present in the solution, the agreement with experiment (Fig. 4.7) can potentially be improved.

The ability of biomolecules to cross-link carbon nanostructures is utilized for their self-assembling [262]. The strength of such a link can also be used as an indirect measure of substrate-biomolecule interaction. A recent experimental study by Ahn et al. [263] examines the gelation of single layer sheets of GO induced by various groups of amino acids, which provides a qualitative measure of amino acid–GO interactions. Among six amino acids (Arg, Gly, Asn, Asp, Cys, Trp) tested experimentally, only arginine induce gelation at pH = 7.5. It is arginine that shows the strongest affinity

to GO surface among all 20 amino acids in our calculations (Fig. 4.6).

4.5.2 Interaction with peptides

The influence of defects on adsorption can be illustrated by the seven peptides studied in Ref [176]. Two out of the 7 peptides studied have negative net charges at physiological conditions, and both of them have worse adsorption than neutral or positively charged peptides. The observed weaker binding of negatively charged peptides is presumably related to the mutual electrostatic repulsion between the peptides and GO, which is also negatively charged due to defects as discussed above. One of these peptides (ELAGAPPEPA), with a net charge of -2 at pH 7, showed no significant adsorption onto GO, whereas another peptide (RRREEETEEE) with a net charge of -3 exhibited weak binding. Although the behaviour of a peptide on a surface is a function not only of its composition but, especially, of the particular sequence the amino acids appear within the peptide, a simple composition analysis of these peptides may provide useful insights into their interactions with GO. Based on amino acid composition and using our calculated adsorption energies for a pristine GO, average adsorption energies per amino acid can be estimated. This rough estimate of peptide-GO interaction suggests that the second peptide interacts more strongly with the surface (average adsorption energy per amino acid of -0.50 eV/residue) than the first (-0.38 eV/residue), due to the presence of the positively charged amino acids (Arg, R) which exhibit strong interactions with GO in our calculations even in the absence of carboxyl defects.

4.6 Conclusions

We present an atomic charge model for GO based on the *ab initio* electrostatic potential (ESP) of epoxy and hydroxyl functional groups at the surface of GO. The proposed charge model is tailored to the TIP3P water model and includes polarization effects. Molecular dynamics simulations with the Amber03 force field were performed in order to assess the adsorption capacity of GO. The adsorption energies for 20 proteinogenic amino acids on the surface of GO were calculated using the scaled ESP charge model proposed above. The scaled ESP charges lead to the stable adsorption of amino acids to the surface. The bioadhesive properties of GO are similar to that of gold, however they can be weakened due to the presence of defects. Experimental evidence for the binding affinity of peptides to GO supports our proposed charge model.

4.7 Appendix

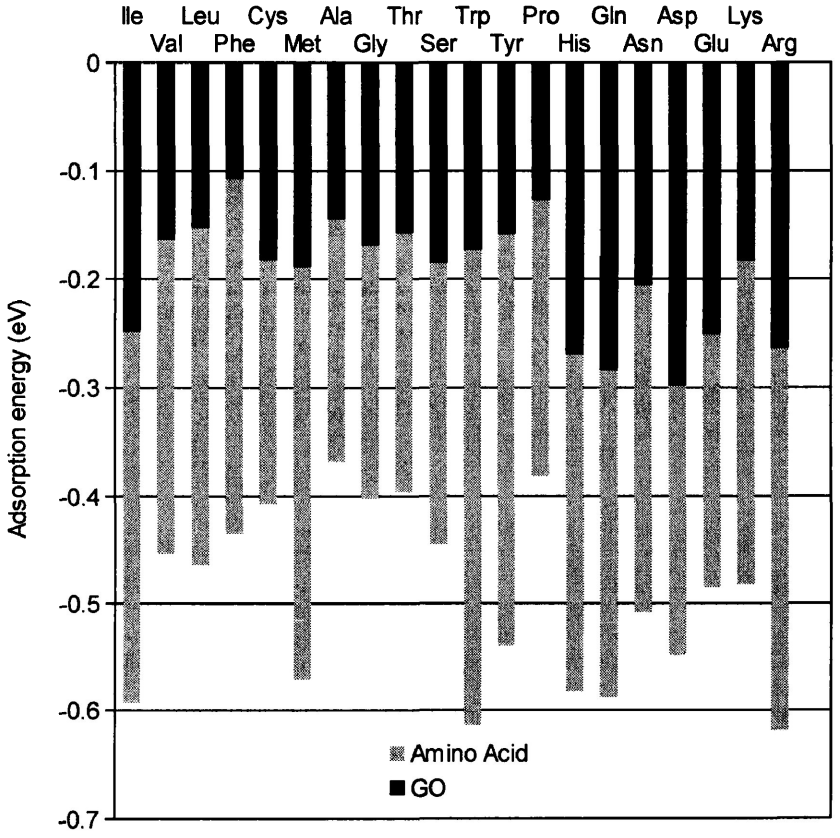

Figure 4.8: Partitioning of the strongest adsorption energies calculated with SESP charge model for 20 amino acids on GO according to amino acid/GO contributions. Amino acids contribute to more than 50% of the total adsorption energy.

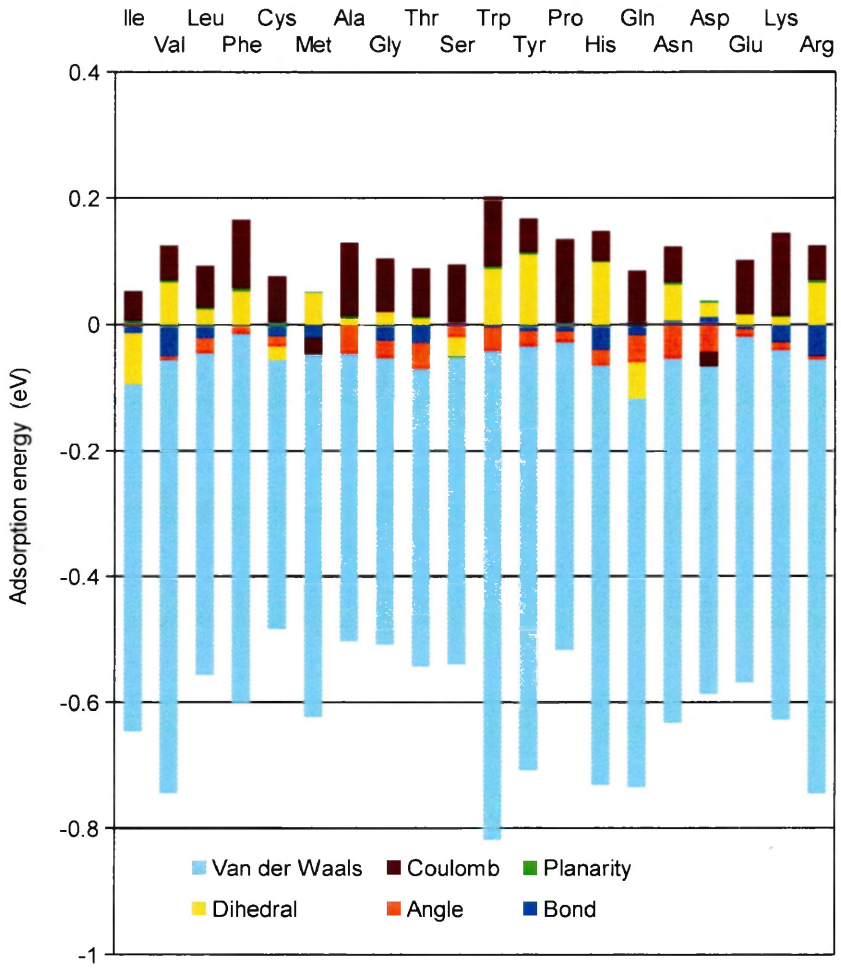

Figure 4.9: Individual components of the adsorption energies calculated with the SESP charge model for 20 amino acids on GO surface. The van der Waals component is a dominant component that favors adsorption at the surface and is governed by the size of the amino acid. The Coulomb and dihedral components are weaker and mostly reduce the binding energies.

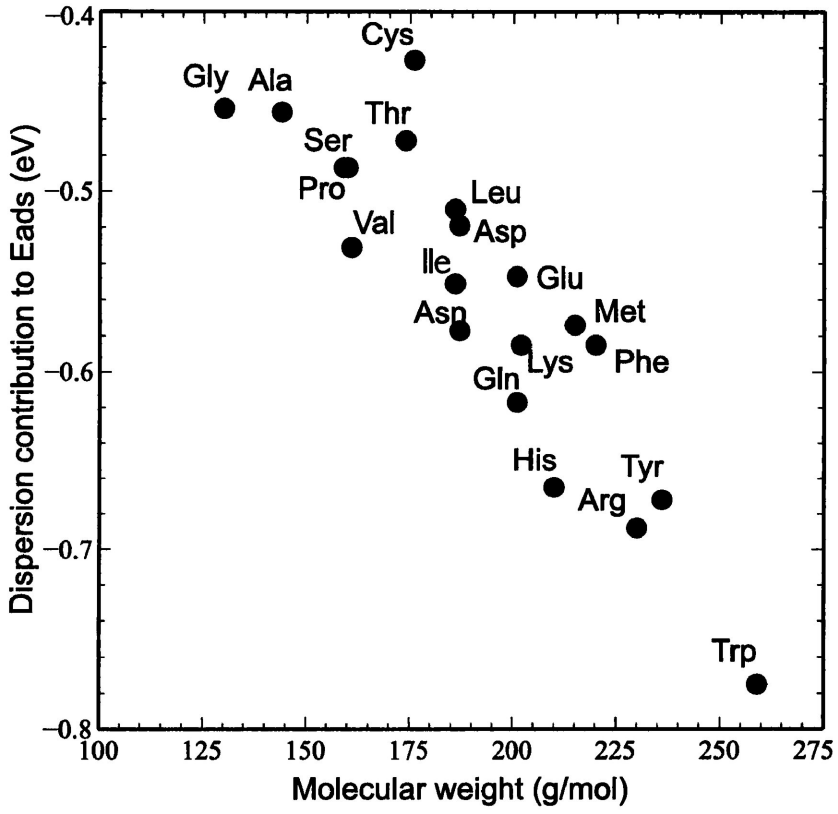

Figure 4.10: Correlation of the dispersion contributions to the adsorption energies of 20 amino acids to GO. Larger amino acids exhibit a stronger van der Waals attraction.

Table 4.2: Average adsorption energies in eV for the capped and uncapped amino acids at the surface of graphene oxide with a variation less than 0.05 eV.

Amino acid name	Capped	Uncapped
Ile (I)	−0.48	−0.31
Val (V)	−0.40	−0.13
Leu (L)	−0.38	−0.36
Phe (F)	−0.43	−0.40
Cys (C)	−0.38	−0.35
Met (M)	−0.45	−0.34
Ala (A)	−0.36	−0.17
Gly (G)	−0.39	−0.24
Thr (T)	−0.38	−0.17
Ser (S)	−0.42	−0.29
Trp (W)	−0.59	−0.46
Tyr (Y)	−0.49	−0.49
Pro (P)	−0.35	−0.31
His (H)	−0.54	−0.35
Hip [3]	...	−0.40
Gln (Q)	−0.49	−0.46
Asn (N)	−0.45	−0.37
Asp (D)	−0.48	−0.29
Glu (E)	−0.47	−0.40
Lys (K)	−0.46	−0.55
Arg (R)	−0.62	−0.80

[3]For the comparison to experimental data, the average adsorption energy for the uncapped protonated histidine is also calculated and shown here.

Chapter 5

Foreign body reaction puzzle: fibrinogen adsorption onto graphene surface

This chapter is dedicated to results on fibrinogen D-domain interaction with graphene as well as poly(ethylene) glycol surfaces. It corresponds to a manuscript prepared for publication by the author. The script used to perform the simulations was developed by me, and its basic concepts are described in the methods chapter. I participated in system selection, performed the simulations, analyzed and interpreted the data, as well as created the figures. This chapter provides an overview of the analysis of structural rearrangements of fibrinogen D-domain as a result of adsorption to highly hydrophobic graphene surface. As a negative control, the interactions of the fibrinogen D-domain with a hydrophilic poly(ethylene) glycol (PEG) surface was modelled and simulated. The results presented in this chapter support a methodology to prelimi-

nary investigate potential biocompatible properties of artificial surfaces that depend on their wettability.

5.1 Abstract

Change in the conformation of blood proteins due to their binding to artificial surfaces is the initial step in the chain of immunological reactions to foreign bodies. Despite the large amount of experimental studies that have been performed on fibrinogen adsorption, a clear picture describing this complex process has eluded researchers thus far. Developing a better understanding of the behaviour of bioactive fibrinogen motifs upon interaction with the surface may facilitate the design of advanced materials with improved biocompatibility. This is especially important within the context of medical implants. Here, we present results of the simulation of fibrinogen D-domain adsorption onto a graphene surface. Graphene is an example of a highly hydrophobic surface that is susceptible to non-specific protein binding. Results of molecular dynamics calculations in an explicit solvent show that the fibrinogen D-domain structure undergoes significant reorganization of its initial conformation. The structural rearrangements are driven by non-covalent hydrophobic interactions between the protein and graphene. The adsorption of the fragment to the graphene surface was found to be stable and directly affected the secondary structure content of the D-domain, with the subsequent exposure of the functional cryptic sites (P1 γ190-202, P2 γ377-395, and P2-C portion γ383-395). The interaction of the D-domain to a well known biocompatible hydrophilic poly(ethylene) glycol surface was also simulated. The PEG monolayer shows a resistance to the D-domain adsorption causing some secondary

structure changes.

5.2 Introduction

The interactions between blood proteins and artificial surfaces have attracted much attention recently due to their importance in medical applications. Fibrinogen is one of the most abundant adhesive plasma proteins and is responsible for initiating foreign body reactions, triggering a series of inflammatory and wound-healing responses. Fibrinogen also participates in blood clot formation, which may be one of the reasons for implant rejection [44, 49, 264]. Within a few nanoseconds after implantation, plasma proteins diffuse to the surface of the implant and start to interact with the surface [42, 81, 90, 265]. The conformational changes of the fibrinogen structure after its adsorption to the surface may result in exposure of specific fragments, cryptic sites P1 and P2 [47, 266]. Their chain and residue range correspond to: P1 γ190-202 and P2 γ377-395 (see Fig. 5.1). Immune cells adhere to bioactive sites that are exposed on the adsorbed fibrinogen and promote a cascade of immune reactions [49, 58, 77, 81]. According to Ugarova et al. [53], changes in the structure of the segment P1 (γ190-202), P2 (γ377-395) and, specifically, the P2-C portion (γ383-395) may lead to an increase in fibrinogen binding to immune cells, which is mediated by a phagocyte integrin Mac-1 (CD11b/CD18) [52, 76, 92, 267, 268].

Numerous experimental studies link the adsorption and structural changes of fibrinogen to the surface hydrophobicity. Hydrophobic surfaces (Fig. 5.2 (a)) promote fibrinogen adsorption and significant irreversible reorganization of its secondary structure [86, 93–100, 135, 269–276]. In particularly, fibrinogen flattens with time on

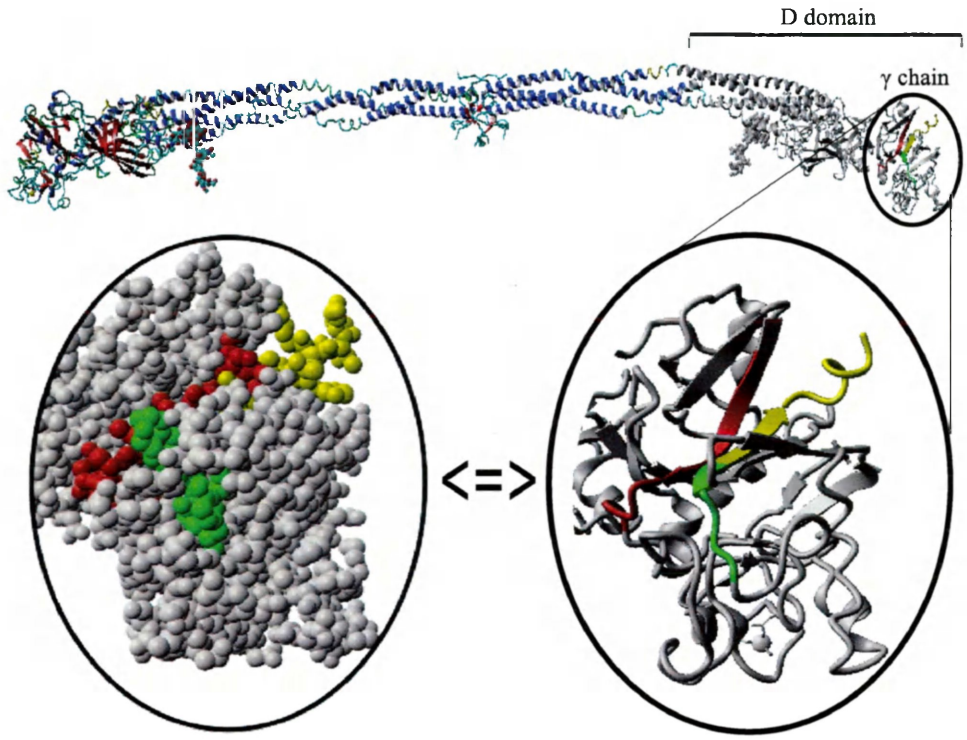

Figure 5.1: Fibrinogen structure (PDB code 1FZA, front view). The γ chain is depicted as ribbon as well as space-filled representation to show the location of hidden binding sites that are found to be responsible for triggering foreign body reaction. The colours refer to the D-domain (grey) and its cryptic motifs P1 γ190-202 (red), P2 γ377-395 (green and yellow), and P2-C γ383-395 (yellow).

graphite [269], highly ordered pyrolytic graphite [99, 270], pure Ti [97, 135], nickel titanium alloy [135], stainless steel [135, 271], poly-L-lysine coatings [269, 277] and other self-assembled monolayers [272–274]. In contrast, similar studies report that the adsorbed fibrinogen repels, adsorbs in reduced amount and preserves its dimensions on hydrophilic surfaces including PEG [278–280], poly(methyl methacrylate) [275],

mica [99, 100], titanium dioxide [86], and silicon dioxide [276]. In addition to changes in the tertiary structure of fibrinogen, significant changes in its secondary structure can be induced due to the interaction with hydrophobic surfaces [93–95]. In contrast, fibrinogen adsorbed on hydrophilic surfaces tends to keep its secondary structure in the native state [93, 96–98].

The experimental studies listed above consistently show that the degree of fibrinogen's conformational changes is larger on hydrophobic surfaces. However, the experimental works provide limited molecular level information on the protein-surface interactions. Better knowledge of the molecular mechanisms responsible for triggering foreign body reactions can advance and guide the development of new surfaces with combined biocompatible and bioadhesive properties.

Molecular dynamics (MD) simulations is an approach that explores details of protein interactions with a surface at the atomistic level. Attempts to understand the protein-surface interactions have been made for different blood proteins. Shen et. al [281] have modelled fibronectin (an extracellular matrix protein) adsorption onto hydroxyapatite to show the correlation between its conformational change and rate of bone cells adhesion. At the time of this writing, there was only one theoretical study on the characterization of fibrinogen-surface interactions using MD simulation method [282]. This study focused on investigating the effects of various types of surface hydrophobicities on their interactions with the γ-chain fragment of fibrinogen (Fig. 5.1). Fibrinogen consists of 5,768 amino acids, 84 of them are included in the γ-chain [283]. Agashe et. al [282] found surface-induced rotational and translational motions of the fragment. Their results show no major difference in the conformational structure of the initial and final adsorbed state of the fragment. It should be noted

that a detailed analysis of the structural changes in P1 and P2 sites due to the adsorption to the hydrophobic surface is not provided. While this is the first comprehensive MD simulation of the fibrinogen fragment adsorption on various surface chemistries, their work does not show differences in the fragment adsorption behaviour at surfaces with various hydrophobicity. This may be due to either insufficient simulation time scale (only 5 ns) and/or the limited fragment size.

The size of whole fibrinogen molecule precludes its all-atom MD modelling in an explicit solvent. The question arises as to what is the minimal size of fibrinogen fragment that captures its immune response characteristics. Several experimental studies [47, 51–54, 76] of fibrinogen inflammatory binding sites were performed on a purified D-domain (Fig. 5.1). These works indicated a paramount importance of the inaccessible binding sites in the recruitment of phagocytes during the inflammatory response. The authors performed antigen-antibody tests as well as measured a concentration of phagocytes accumulated on the surfaces that were pre-adsorbed with fibrinogen D-domains. These studies also confirm fibrinogen D-domain as an individual functional unit that may be used to investigate fibrinogen bioactive binding sites responsible for biocompatible properties of a surface.

Graphene is one of the most widely investigated materials with a variety of potential biomedical applications [110, 112, 114]. Experimental studies show that graphene can stimulate bone [284] and stem cell growth [125]. On the other hand, cytotoxicity studies indicate that graphene causes cell apoptosis in macrophages [285, 286] as well as size-, shape-, and concentration-dependent cytotoxicity in mast cells [215], erythrocytes, and fibroblasts [287]. Overall, the biocompatibility of graphene seems controversial [114, 128]. This may be due to the fact that graphene exhibits hydrophobic

and/or hydrophilic properties depending on the production method as well as degree of oxidation [110]. Pristine graphene is an example of highly hydrophobic surface that according to multiple studies is supposed to induce significant conformational changes on adsorbed proteins and, as a result, is a good model to investigate the molecular mechanisms responsible for foreign body reactions.

In this study, all-atom MD simulations in explicit water is performed to model fibrinogen D-domain/graphene interactions. The emphasis is placed on studying the D-domain as a representative functional unit responsible for the foreign body immune reaction. The calculations are performed using AMBER03 force field, which was validated for biomolecule-graphene interactions in our previous studies [170, 211] (see also Chapter 3,4). The temporal evolution of protein structural parameters is analyzed over the time scale of 60 ns (unless otherwise specifically noted). The data presented in the Results Sec. 5.4 for all D-domain positions at the surface of graphene corresponds to 60 ns of the simulation time, while the 'perpendicular' orientation of the D-domain onto PEG self-assembled monolayer was simulated for 30 ns. Our results provide insight into the protein's affinity for the surface and the stability of its structure on the graphene and PEG surfaces. These properties are related to the biocompatible characteristics of graphene and PEG.

5.3 Method

5.3.1 Simulated system

The model of graphene surface consisted of 10,944 carbon atoms arranged in a hexagonal structure with 1.418 Å initial distance between bonded atoms [194] (Fig. 5.2 (b)). The initial structure of the D-domain of fibrinogen used in our MD simulations was taken from Protein Data Bank (PDB identification code 1FZA) as determined to 2.90 Å resolution using X-ray diffraction [283]. Spraggon et. al [283] showed that the D-domain contains three tightly coiled together chains, α, β and γ, which are 107.72 Å, 48.08 Å and 167.56 Å in length, respectively. It consists of a coiled-coil and two homologous globular regions. The D-domain contains 734 amino acids: 87 residues in the α polypeptide chain (Valα111 - Proα195), 328 in the β-chain (Lysβ148 - Glnβ460), and the 319 amino acids in γ polypeptide chain (Lysγ88 - Gluγ396). As previously mentioned, the crystal structure of fibrinogen consists of two D-domains and one E-domain or 5,768 amino acids: 562 residues in the α-chain, 461 in the β-chain and 411 in the γ-chain [283]. In general, the globular structure of the D-domain is 130 Å long, which is about one-third of the whole fibrinogen structure with 450 Å length. Only coiled coil region in the D-domain consists of residues Valα111 - Serα160 (α-chain, 50 residues), Aspβ134 - Tyrβ192 (β-chain, 59 residues), and Lysγ88 - Glnγ134 (γ-chain, 47 residues). Two-stranded parallel β-sheet is formed from β and γ-chains. There are 8 disulphide bonds present: 3 interchain and 5 intrachain [283]. The cryptic sites responsible for the binding to leukocyte integrin are located within the γ-chain: P1 (190-202: GWTVFQKRLDGSV), and P2-C (383-395: TMKIIPFNRLTIG), and P2 (377-395: YSMKKTTMKIIPFNRLTIG). To complete

the D-domain structure for simulation purposes, hydrogen atoms were added to the structure taken from the PDB.

A simulation box of $176.84 \times 161.65 \times 250$ Å^3 with periodic boundary conditions was chosen for graphene sheet based on the three-dimensional size of the D-domain (130 Å), to allow for its free orientation while precluding interactions between the periodic images (Fig. 5.2 (b)).

A PEG surface was modelled with 1,296 units arranged in a hexagonal pattern (Fig. 5.2 (c,d)) [288, 289]. The size of the simulation box for PEG was set to $182.84 \times 158.00 \times 250$ Å^3. The basic unit of PEG was taken from Ref. [290], and reduced to 20 atoms: 5 carbons, 3 oxygens and 12 hydrogens. The shorter length of the chain helped to save simulation time without compromising the quality of of D-domain/PEG-monolayer interactions. It should be noted that in this model, only upper hydroxyl groups played an active role through interactions with the D-domain. An individual PEG chain was minimized in vacuum first. The multiple PEG chains were organized in self-assembled monolayer by fixing of 12 atoms starting from the bottom of the layer (Fig. 5.2 (b)). The remaining 6 atoms, including hydrophilic hydroxyl groups, were allowed to move freely and interact with the D-domain (Fig. 5.2 (d)). The chains were placed in close-packed hexagonal arrangement with 4.97 Å length between carbon atoms (located at the bottom of the monolayer) that are close neighbours (Fig. 5.2(c)) [288, 289]. All chains were parallel to each other and oriented at 30 ° angle with respect to the surface normal (Fig. 5.2(d)) [288]. As a result, a maximum hydroxyl group density on the surface interacting with the D-domain was achieved. The surface thus modelled is highly hydrophilic (a contact angle about 0 °), protein-resistant and biocompatible [291]. The PEG monolayer, an excellent example

of protein-repelling or non-fouling surface, used in this study as a negative control for a reference of biocompatible properties of the surface. It should be noted that bioadhesive characteristics of the surface do include partial protein adsorption that is not accompanied by its crucial structural changes.

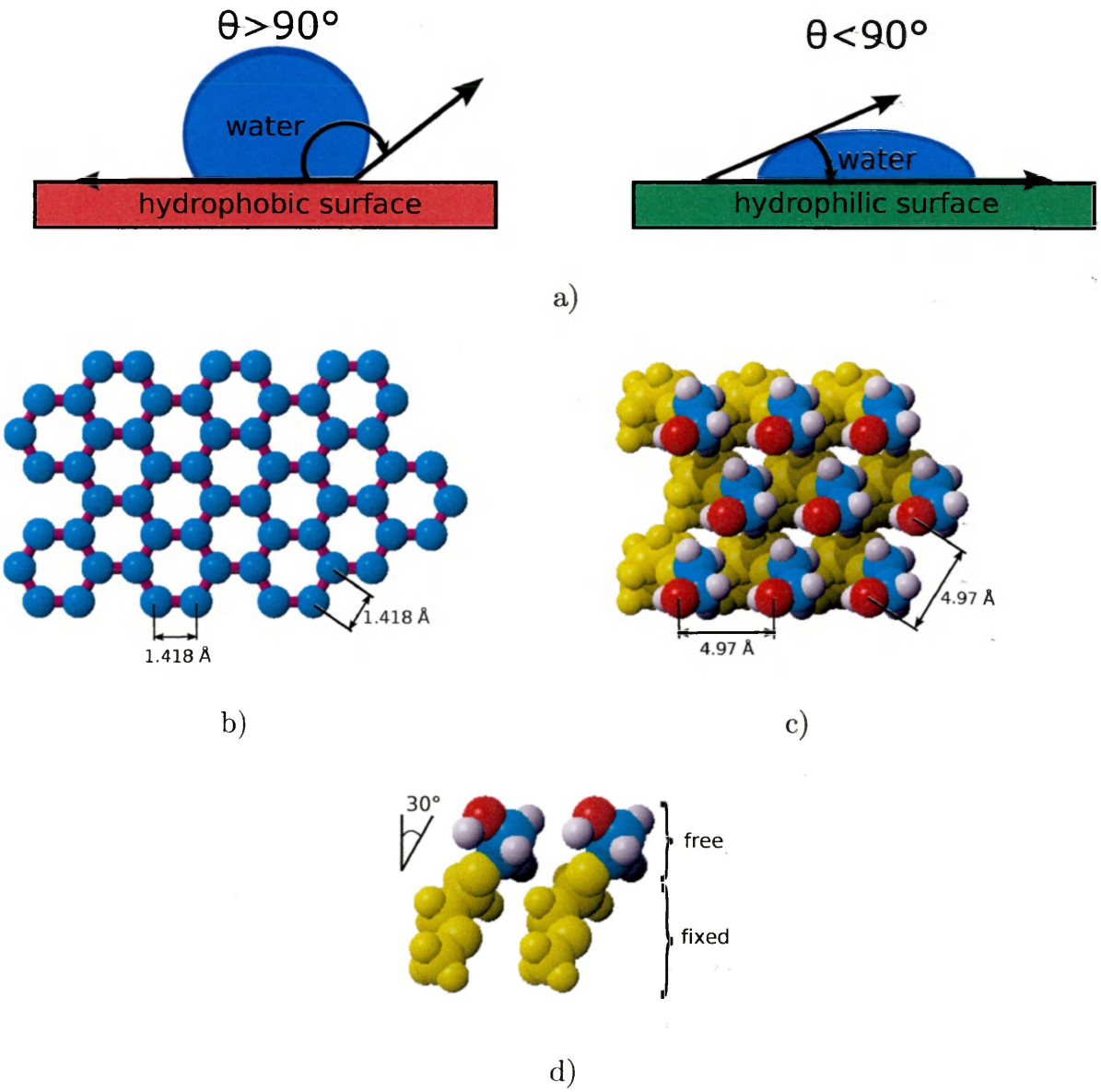

Figure 5.2: Water droplet on hydrophobic vs hydrophilic surfaces (a): θ is a contact angle (see Sec. 1.3.1 for details); top view: hexagonal structure of graphene surface (b) and PEG self-assembled monolayer (c); front view: two representative PEG chains (d): yellow colour refers to fixed atoms, red is oxygen, blue is carbon, and white is hydrogen.

5.3.2 Molecular dynamics simulation strategy

The graphene model was first minimized in vacuum, than an individual fibrinogen D-domain was placed at the surface in three different orientations that correspond to 'top', 'side' [274] and 'perpendicular' positioning of the fragment with respect to the surface (Fig. 5.3, Fig. 5.4, Fig. 5.5). As a negative control for the developed methodology, the graphene layer was replaced by PEG, a highly hydrophilic (25° contact angle) [292] synthetic polymer [293], and the simulation was repeated with initial conditions identical to those used for the case of graphene surface. For PEG monolayer, 'perpendicular' orientation of D-domain was chosen (Fig. 5.7) because according to experimental studies [274, 294], the density of adsorbed fibrinogen is 7 times higher for end-on in comparison to side-on orientation. Next, the minimization procedure was repeated for D-domain/surface system in vacuum. The upper limit for the initial contact distance between the domain and the surface was set at a single distance within a range of 2.5-5.5 Å. This distance was chosen so that the most energetically favorable interactions are included, while the fragment is still reasonably far from being adsorbed to the surface. Single amino acids were already found to be favourably interacting with the surface at 3 Å distance (see Chapter 3 for details) [170].

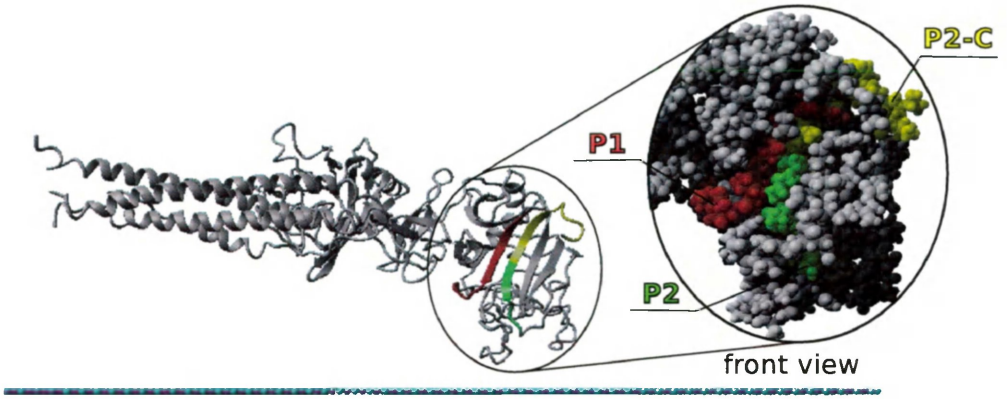

a)

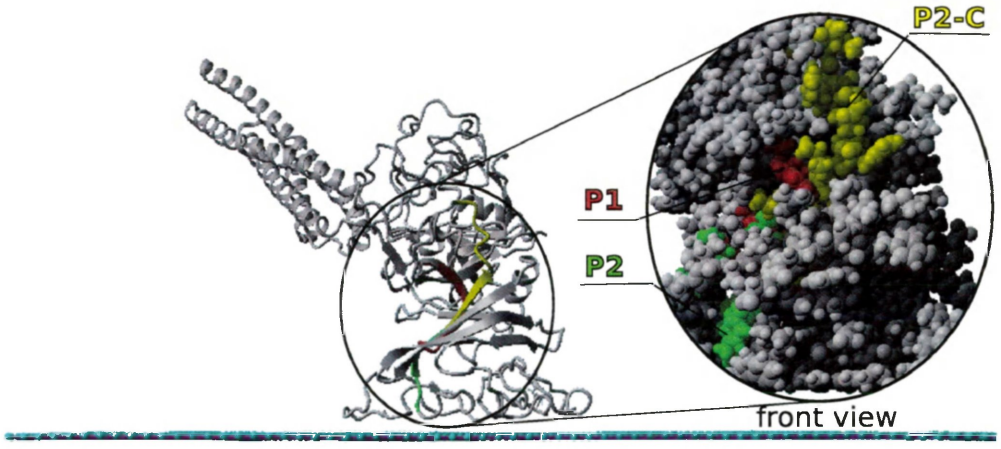

b)

Figure 5.3: Top orientation. Initial (a) and final (b) positions of the fibrinogen D-domain on the surface of graphene after simulation time of 60 ns (front view). The colours refer to the domain's cryptic motifs P1 γ190-202 (red), P2 γ377-395 (green and yellow), and P2-C portion γ383-395 (yellow). The initial distance between the fragment and surface was set at 5 Å. The fragment initially positioned at the 'top' orientation adsorbs to the surface during the 60 ns simulation time.

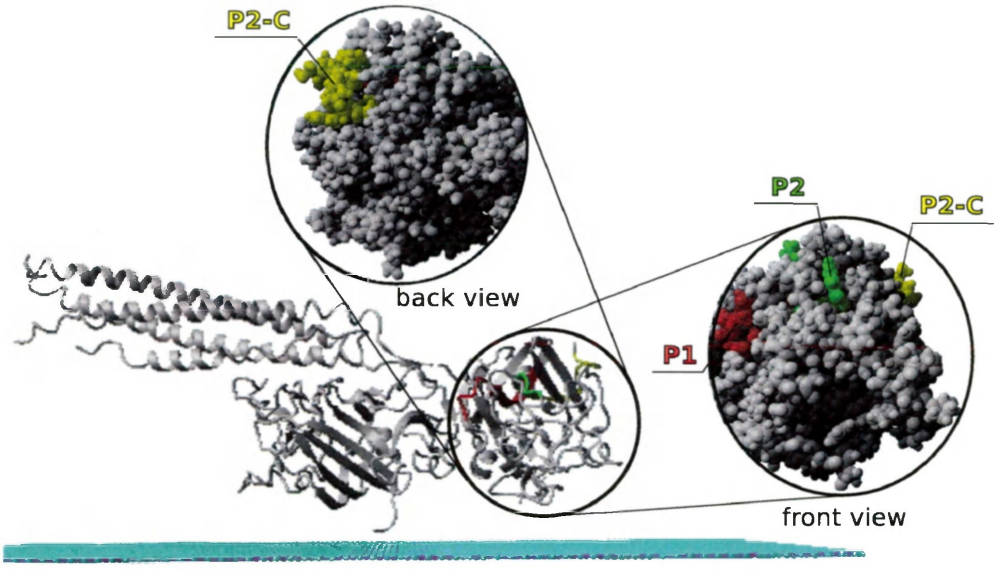

a)

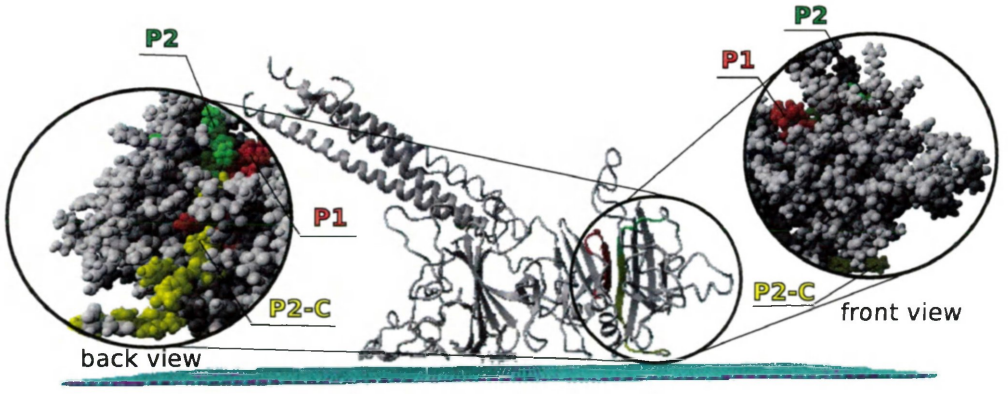

b)

Figure 5.4: Side orientation. Initial (a) and final (b) of the fibrinogen D-domain on the surface of graphene after simulation time of 60 ns (front view). The colours refer to the domain's cryptic motifs P1 γ190-202 (red), P2 γ377-395 (green and yellow), and P2-C portion γ383-395 (yellow). The initial distance between the fragment and surface was set at 3 Å. The fragment initially positioned at the 'side' orientation adsorbs to the surface during the 60 ns simulation time.

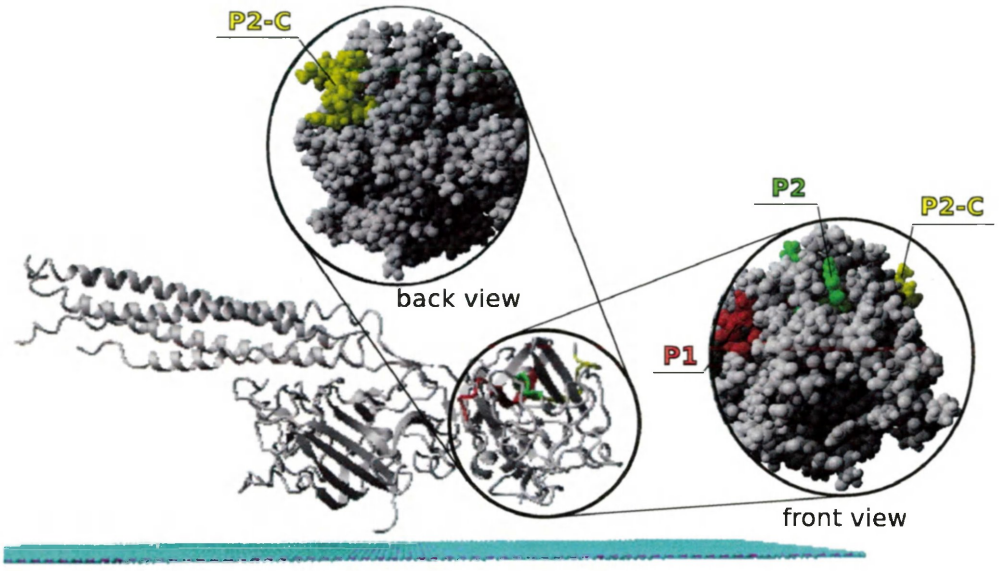

a)

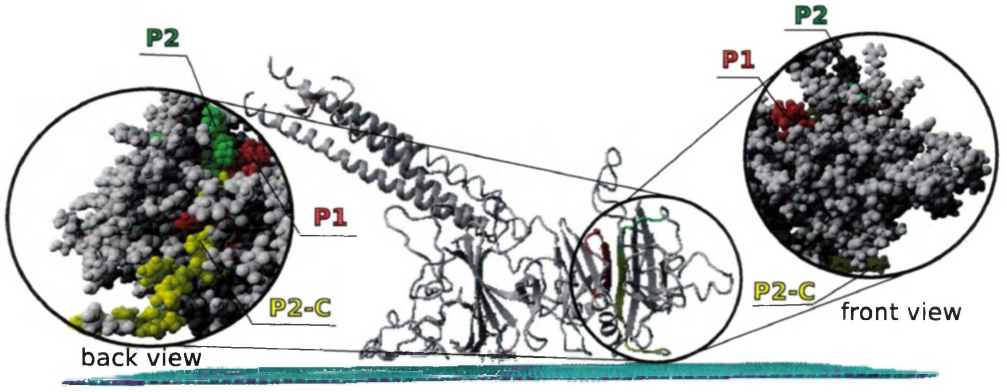

b)

Figure 5.4: Side orientation. Initial (a) and final (b) of the fibrinogen D-domain on the surface of graphene after simulation time of 60 ns (front view). The colours refer to the domain's cryptic motifs P1 γ190-202 (red), P2 γ377-395 (green and yellow), and P2-C portion γ383-395 (yellow). The initial distance between the fragment and surface was set at 3 Å. The fragment initially positioned at the 'side' orientation adsorbs to the surface during the 60 ns simulation time.

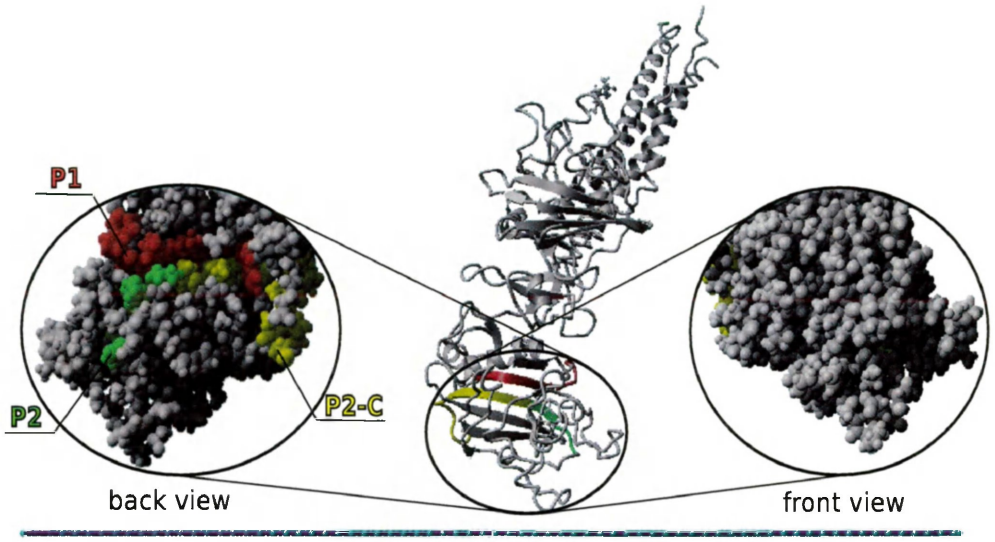

a)

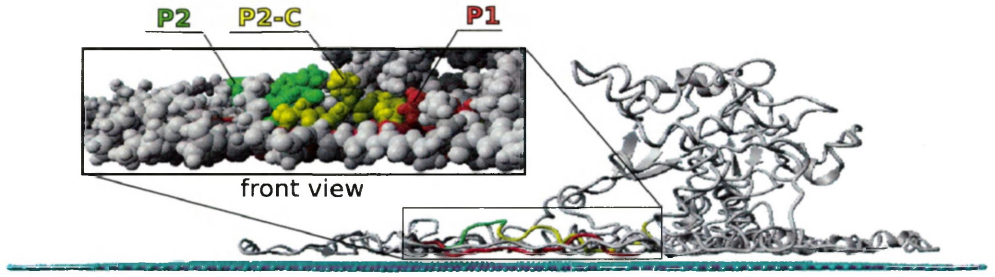

b)

Figure 5.5: Perpendicular orientation. Initial (a) and final (b) of the fibrinogen D-domain on the surface of graphene after simulation time of 60 ns (front view). The colours refer to the domain's cryptic motifs P1 γ190-202 (red), P2 γ377-395 (green and yellow), and P2-C portion γ383-395 (yellow). The initial distance between the fragment and surface was set at 5 Å. The fragment initially positioned at the 'perpendicular' orientation adsorbs to the surface during the 60 ns simulation time.

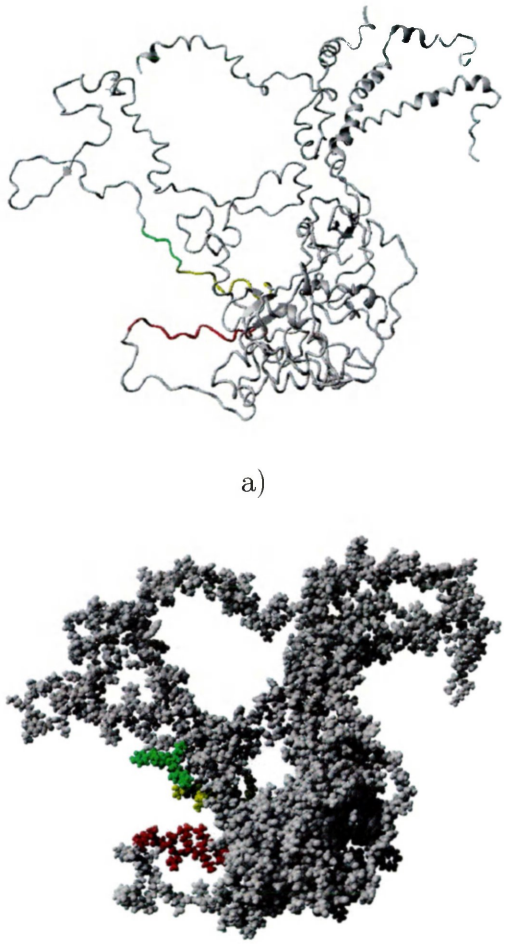

a)

b)

Figure 5.6: Perpendicular orientation. Final depicted as a ribbon (a) as well as space-filled representation (b) of the fibrinogen D-domain on the surface of graphene after simulation time of 60 ns (top view). The colours refer to the domain's cryptic motifs P1 γ190-202 (red), P2 γ377-395 (green and yellow), and P2-C portion γ383-395 (yellow). The fragment initially positioned at the 'perpendicular' orientation undergoes significant changes in its secondary structure following exposure of its binding sites.

For each initial geometry, energy minimization was performed in vacuum at 0K with a time step of 2 fs. Atom velocities were scaled down by a factor of 0.9 every 10th step until convergence was reached, i.e., the total energy improved by less than 0.05 kJ/mol per atom during 200 consecutive steps. Then the system was filled with water while keeping the fragment and graphene geometry unchanged. After that, MD simulation in explicit solvent was performed.

NPT simulations were performed under 1 atm pressure and body temperature (310 K). To mimic physiological conditions, NaCl ions were added to the simulation box with the standard sodium chloride concentration of blood (0.9%). The simulation time for molecular dynamics was 60 ns, which was found to be sufficiently long to achieve equilibrium as determined by stable values for the potential energy of the D-domain/graphene system. The D-domain onto PEG self-assembled monolayer was simulated for 30 ns. All simulations were performed using YASARA simulation package [195] and with AMBER03 force field [196]. The simulations were carried out using similar conditions as previously published studies [170, 211], with the Particle Mesh Ewald algorithm [295] to treat long-range electrostatic interactions. The simulation box was filled with 230110 TIP3P water molecules.

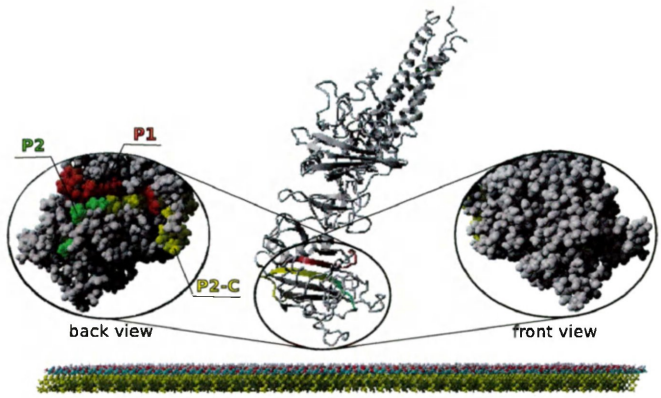

a)

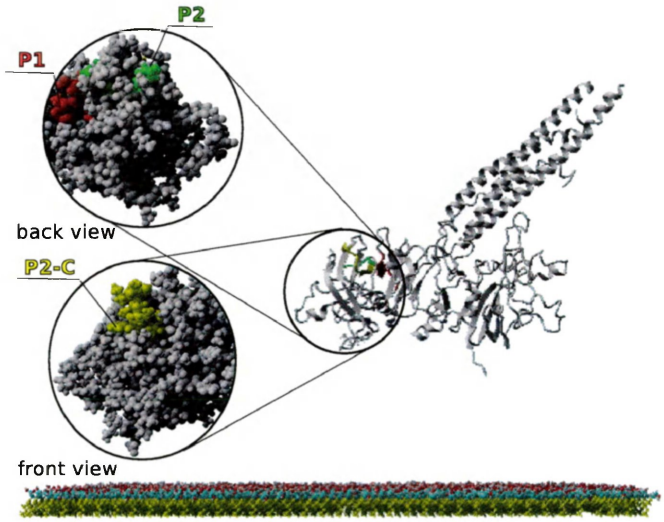

b)

Figure 5.7: Perpendicular orientation. D-domain simulation at the surface of hydrophilic self-assembled monolayer of PEG: initial (a) and final (b) (after 30 ns of the simulation). The initial distance between the fragment and surface was set at 5 Å. The domain tends to resist adsorption to the surface, which is in agreement with experimental studies showing no adsorption of fibrinogen to the hydrophilic surfaces in general, and PEG in particular [282, 283, 286, 308].

5.3.3 Analysis of simulation results

To quantify the affinity of the fibrinogen fragment to the surface and the structural changes resulting from its adsorption to graphene the following parameters, as described below, were computed: adsorption energy, radius of gyration, solvent accessible surface area, and root mean square deviation between initial (minimized in water) and final (after 60 ns of simulation) structures. Energy and structural parameters were calculated for snapshots taken every 10 ps, resulting in 6,000 snapshots for each orientation of the fragment. The 6,000 data points were smoothed over 60 points using a moving window average approach. The structure of the D-domain, after a two-step energy-minimization (individually surface and D-domain/surface systems) and before MD simulation was started, was taken as the initial (reference) structure.

For each orientation of the D-domain relative to graphene, 'top', 'side', and 'perpendicular', the bound state corresponded to the D-domain/graphene system, whereas the unbound (native) state is represented by the corresponding D-domain and graphene surface each simulated individually in the same environment and under the same conditions as the bound state (Fig. 5.3 - Fig. 5.6). The adsorption energy was calculated as the difference between the total potential energies of the D-domain and graphene in the bound and unbound states, respectively

$$E_{\text{ads}} = \langle E_{\text{D-domain}} + E_{\text{graphene}} \rangle_{\text{bound}} - \langle E_{\text{D-domain}} \rangle_{\text{unbound}} - \langle E_{\text{graphene}} \rangle_{\text{unbound}} \quad (5.1)$$

Here the individual energies $\langle E \rangle$ of the D-domain and graphene energies include

their interactions with the surrounding environment (water and counterions). The energies were averaged over the last 20 ns of the simulation in order to exclude the system equilibration period. A negative binding energy is indicative of the protein's affinity for the surface.

Radius of gyration (Rg) is a parameter that captures compactness of the protein structure, and it is sensitive to its degree of folding/unfolding. Rg is defined as the root mean square deviation in distances between each atom of the protein and the protein center of mass [296, 297]

$$R_g = \sqrt{\frac{\sum_{i=1}^{n} M_\mathrm{i} |\mathbf{R}_\mathrm{i} - \mathbf{C}|^2}{\sum_{i=1}^{n} M_\mathrm{i}}} \tag{5.2}$$

Here M refers to the atomic mass, R is a position vector of individual atoms, C represents the position vector for the protein centre of mass and the summation index runs up to the total number of atoms n in the protein. The radius of gyration was calculated for the three D-domain adsorbed orientations as well as its unbound state.

To characterize conformational changes of the D-domain resulting from adsorption, the root mean square deviation ($RMSD$) between the conformer at a time t and the initial ($t = 0$) conformer was calculated using the following formula

$$RMSD = \sqrt{\frac{\sum_{i=1}^{n} |\mathbf{R}_\mathrm{i}(t) - \mathbf{R}_\mathrm{i}(0)|^2}{n}} \tag{5.3}$$

where R_i are the Cartesian atomic coordinates and n is the total number of atoms

in the D-domain fragment. The $RMSD$ is another test to assess changes in the protein's global structure over time. The general changes in the three D-domain models were monitored computing $RMSD$ values of the C-α atoms (in this case, n in Eq. 5.3 refers to the number of only C-α atoms) compared to its initial structure minimized in water.

The solvent accessible surface area ($SASA$) is the surface area of a protein that is accessible to a surrounding solvent [298, 299]. It is computed numerically by first tessellating the surface of the protein and then summing up the area of the created polygons in $Å^2$. An atom contributes to $SASA$ if the distance between it and the water probe's oxygen nucleus does not exceed the sum of the van der Waals radii of the solute atom and the water probe [195]. Changes in $SASA$ indicate whether more or less exposure to solvent has occurred as consequence of the interactions with the graphene/PEG surface, relative to the native state of the protein [300]. $SASA$ can be calculated for the whole D-domain fragment, for particular segments or for individual residues. Thus, it can be used to assess if residues known to be involved in molecular recognition by immune cells became exposed to solvent as a result of surface adsorption.

Hydrogen interactions provide bonding network that facilitates protein folding. Specifically, hydrogen bonds are responsible for maintaining secondary structure of the protein such as α-helix and β-sheet [301]. By analyzing the number of hydrogen bonds within D-domain during the simulation, the degree of changes in its secondary structure can be investigated, as a result, studying these weak bonds can lead to a better understanding of protein/surface interactions and the influence of each on the other. The number of hydrogen bonds was estimated using a hydrogen bonding

energy cutoff of 6.25 kJ/mol, which is 25% of the optimum value 25 kJ/mol (Eq. 5.4) [195].

$$E_{\text{H\_bond}} = 25 \times \frac{2.6 - max(Distance_{\text{H-A}}, 2.1)}{0.5} \times Scale_{\text{D-H-A}} \times Scale_{\text{H-A-X}} \qquad (5.4)$$

Where the hydrogen bonding energy is a function of the hydrogen-acceptor distance ($Distance_{\text{H-A}}$) in Å as well as two scaling factors $Scale_{\text{D-H-A}}$ and $Scale_{\text{H-A-X}}$. Here, $Scale_{\text{D-H-A}}$ depends on an angle formed between donor, hydrogen atom, and acceptor. If the angle is within 0-100° range, $Scale_{\text{D-H-A}}$ is equal to zero, if the angle is between 100 and 165°, $Scale_{\text{D-H-A}}$ is between 0 and 1, and if the angle is 165-180°, $Scale_{\text{D-H-A}}$ is equal to 1. Another scaling factor, $Scale_{\text{H-A-X}}$, can be found from the angle formed by hydrogen, acceptor, and atom covalently bound to the acceptor. If the angle is within 0-85° range, $Scale_{\text{H-A-X}}$ is equal to zero, if the angle is between 75 and 85°, $Scale_{\text{H-A-X}}$ is defined between 0 and 1, and if the angle is 85-180°, $Scale_{\text{H-A-X}}$ is equal to 1. The number of inter- and intra- hydrogen bonds are calculated between initial and final D-domain, and within one D-domain i.e. between its α, β, and γ chains.

Secondary structure content was defined by calculating the percentage of the protein's current secondary structure such as α-helix, β-strand, turn and coil relatively to the whole D-domain secondary structure taken as 100%. The detailed secondary structure analysis (per residue) was calculated using the program DSSP [302, 303] and it is presented as a table of each amino acid within D-domain that were encoded by colour depending on the type of secondary structure such as α-helix (pink),

β-extended strand (orange), bend (blue), β bridge (purple), hydrogen-bonded turn (green), G-helix (yellow), and undetermined/random coil (grey), respectively. The analysis was performed for each D-domain orientation on graphene and PEG surfaces every 20 ns of the simulation time.

5.4 Results

5.4.1 Convergence of the systems and stability of its reference point

MD simulation of fibrinogen D-domain in the absence of a graphene sheet under the same conditions as other systems was performed to confirm stability of the individual D-domain in water. This system was used to get a reference fragment structure, and was named 'unbound' or native fragment state. The time-dependent structural parameters calculated for the unbound state show constant values with minimal deviations (for example, see Fig. 5.9 - Fig. 5.13). The converging potential energies for all the D-domain systems simulated indicate that the systems were equilibrated (Fig. 5.8). Although the D-domain eventually desorbs from the PEG monolayer, its potential energy includes protein-surface interactions that results in similar value of the binding energy as for D-domain adsorbed at 'top' and 'side' orientations on graphene.

The calculated binding energies for the adsorbed fibrinogen fragment can be found in Table 5.1. The D-domain shows a consistent adsorption to graphene surface due to hydrophobic interactions. According to Chapter 3 [170], the average binding energy

of a single amino acid to graphene sheet in aqueous environment is -0.35 eV or -36.42 kJ/mol. The D-domain contains 734 residues, it means that an estimated adsorption energy for D-domain at the surface of graphene is about -26,730 kJ/mol. By taking into account a complexity and composition of D-domain structure in comparison to an individual amino acid, a stronger (more negative) than -26,730 kJ/mol interaction should take place (Table 5.1).

Table 5.1: Average adsorption energies in kJ/mol for fibrinogen's D-domain on the surface of graphene with a deviation less than 15 kJ/mol.

D-domain position	Adsorption energy (kJ/mol)
top	$-36,518$
side	$-36,600$
perpendicular	$-47,412$

For the unbound (native) system, slight deviations in $RMSD$ of the D-domain structure occurred in the first 12 ns of the simulation, but than the parameter remained steady with an averaged value of less than 3 Å (Fig. 5.9, Fig. 5.10, Fig. 5.11). This is in agreement with studies showing $RMSD$ values between 2.0 and 4.0 Å for stable native protein states [304–308]. To better compare the results, the folded (native) state of the D-domain simulated in water was used as a reference for our calculations at each point during 60 ns of time evolution.

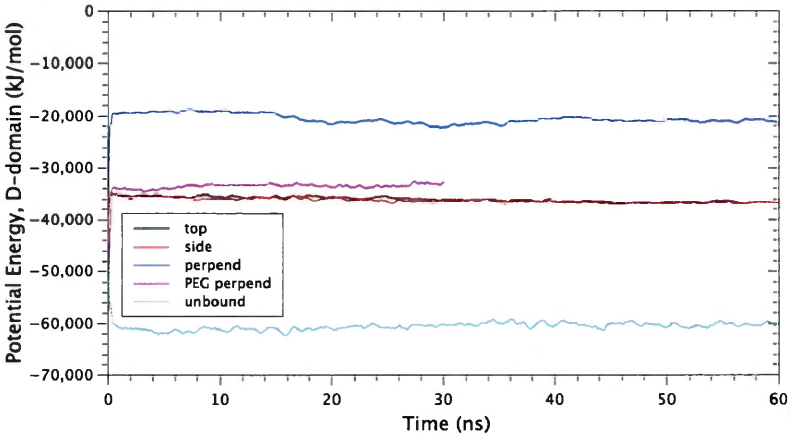

Figure 5.8: Potential energies (kJ/mol) for individual D-domain fragment in water in the absence of graphene or PEG surface (unbound), or in the presence of surface with different starting orientations.

5.4.2 Analysis of structural changes

Changes in the protein structure were analyzed by calculating structural parameters $RMSD$, $SASA$, radius of gyration and secondary structure content. These quantities capture a general structural trend as well as specific changes in structure that result from adsorption to the surface.

To investigate the hypothesis that the D-domain undergoes partial unfolding and spreading in order to maximize the interaction with the hydrophobic graphene surface (Fig. 5.3, Fig. 5.4, Fig. 5.5, Fig. 5.6), the $RMSD$ between unbound/native and adsorbed structures of the D-domain every 1 ns for total 60 ns of simulation time was obtained. $RMSD$ shows a steady increase for the 'perpendicular' orientation. Also, $RMSD$ fluctuates more for 'top' and 'side' orientations of the fragment in comparison to its native state in water (in the absence of graphene). Obviously, $RMSD$

parameter for D-domain 'perpendicular' (end-on) configuration at the surface grows markedly and steadily (Fig. 5.9, Fig. 5.10, Fig. 5.11). This increase essentially represents rearrangements in the D-domain structure, and more importantly, in the P2-C motif (Fig. 5.11), which was found to play crucial role in the initiation of inflammatory responses to the substrates [53]. There is also a faster structural change for D-domain in the 'side' adsorptive position in comparison to 'top' one, their $RMSDs$ end up in the range of 10 to 15 Å at 60 ns. The reasons for such D-domain behaviour will be discussed in more details in Sec. 5.5.

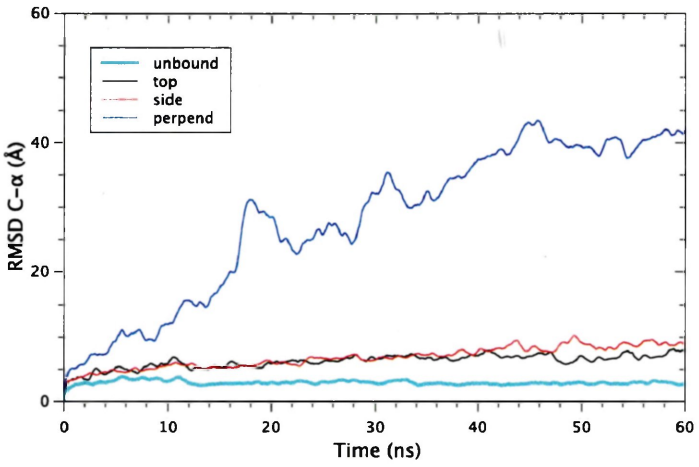

Figure 5.9: Conformational changes of D-domain residues measured by C-α $RMSD$ upon adsorption onto the surface of graphene. The figure shows $RMSD$ values relative to the initial, energy minimized, conformation from the beginning until the end of simulations (60 ns).

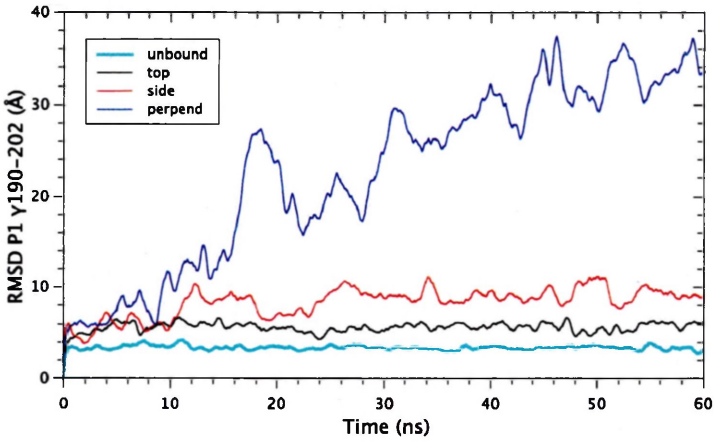

Figure 5.10: Conformational changes of D-domain residues measured for P1 binding sequence upon adsorption onto the surface of graphene. The figure shows $RMSD$ values relative to the initial, energy minimized, conformation from the beginning until the end of simulations (60 ns).

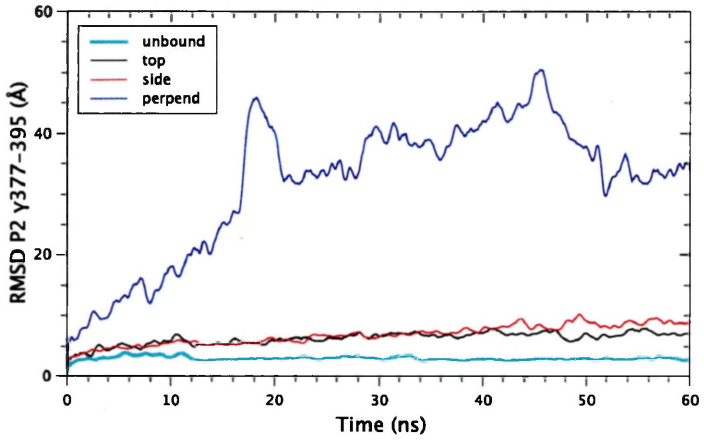

Figure 5.11: Conformational changes of D-domain residues measured for P2 binding sequence upon adsorption onto the surface of graphene. The figure shows $RMSD$ values relative to the initial, energy minimized, conformation from the beginning until the end of simulations (60 ns). $RMSD$ shows a steady increase for the 'perpendicular' orientation. Also, $RMSD$ fluctuates more for 'top' and 'side' orientations of the fragment in comparison to its native state in water (in the absence of graphene).

The protein's structural rearrangements are usually accompanied by changes in solvent accessible surface area ($SASA$) (Fig. 5.12). In the case of graphene, while $SASA$ for the unbound (native) state of the P2 sequence remains constant at approximately 100 $\pm$ 5 Å^2 throughout the simulation, $SASA$ for the 'side' orientation increases significantly starting after 30 ns of simulation time from 120 to 180 Å^2, i.e. by 50%. This indicates solvent exposure which can be also observed in Fig. 5.4. In comparison, Fig. 5.13 shows that for a PEG monolayer much less structural changes in $SASA$ value occurs for this sequence.

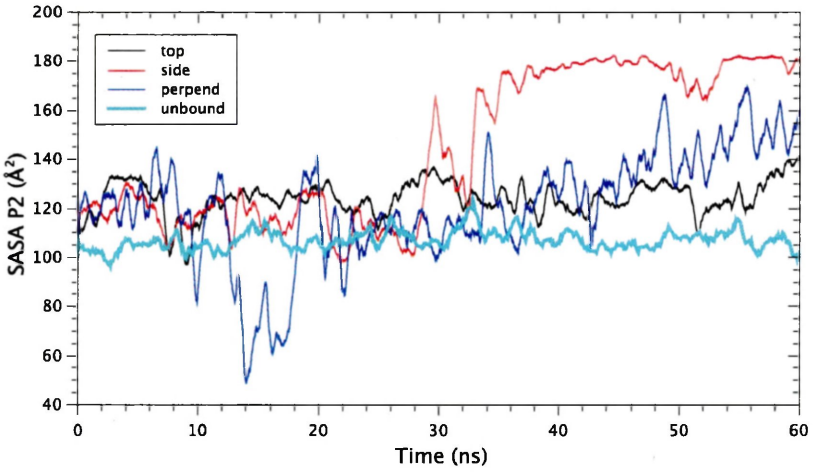

Figure 5.12: $SASA$ of fibrinogen D-domain cryptic sites P2 at the surface of graphene. The curves correspond to the 'top' (black), 'side' (red), and 'perpendicular' (blue) initial positions at the surface as well as fragment's unbound state (bold cyan) that represents its native structure.

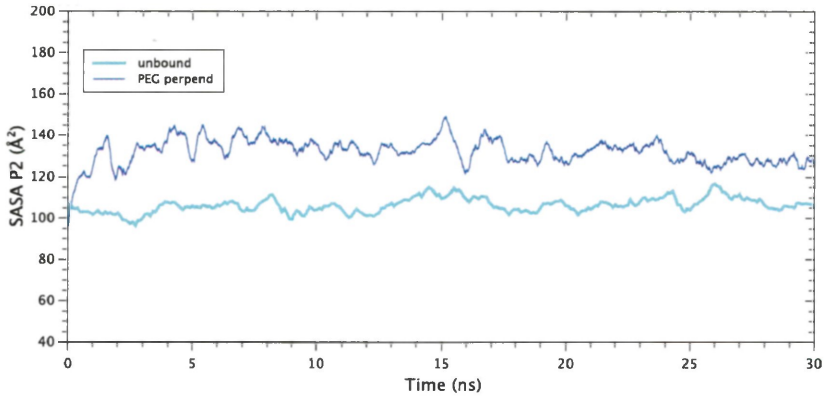

Figure 5.13: *SASA* of fibrinogen D-domain cryptic sites P2 interacting with PEG monolayer. The curves correspond to the 'perpendicular' (blue) initial positions at the surface as well as fragment's unbound state (bold cyan) that represents its native structure.

Table 5.2: Calculated structural parameters for the D-domain of fibrinogen adsorbed to a surface of graphene, with standard deviations of less than 1%. The initial and final stages correspond to t_i=0 ns and t_f=60 ns, respectively, otherwise it is specified.

Position/State	Top		Side		Perpendicular		Native (Unbound)[1]	
Parameter/Time	initial	final	initial	final	initial	final	initial	final
The closest distance[2] (Å)	5.45	2.46	2.96	2.41	5.35	2.12	···	···
Averaged over last 20 ns	···	**2.41**	···	**2.35**	···	**2.18**	···	···
Hydrophobic interactions (t_i=2ns)	273.00	3,750.00	534.00	4,268.00	**1,301.00**	**23,387.00**	···	···
Strength of hydrophobic contacts	118.08	1,655.92	230.90	1,838.88	552.27	10,204.50	···	···
Radius of gyration (Å)	36.45	36.03	36.45	38.02	**36.46**	**55.04**	36.46	37.06
Averaged over last 20 ns	···	36.81	···	38.22	···	54.96	···	36.84
Potential Energy (kJ/mol)	−43,563	−35,762	−42,701	−36,996	−43,446	−21,253	−42,222	−59,661
Averaged over last 20 ns	···	−36,696	···	−36,707	···	−20,819	···	−60,200
SASA P2 (Å^2)	**99.36**	**148.96**	**100.33**	**180.624**	**101.91**	**164.46**	100.76	102.36
Averaged over last 20 ns	···	125.40	···	178.24	···	141.34	···	106.97
RMSD P2 (Å)	0	6.90	0	8.85	**0**	**32.94**	0	2.87
Averaged over last 20 ns	···	6.98	···	8.61	···	38.74	···	2.91
α-helix [3] (%)	22.63	26.17	23.48	20.34	**23.47**	**13.57**	24.32	26.73
Averaged over last 20 ns	···	24.94	···	23.99	···	11.84	···	27.09
β-strand (%)	21.50	19.66	21.08	19.14	**20.50**	**3.40**	21.22	22.35
Averaged over last 20 ns	···	20.03	···	19.09	···	4.69	···	21.44
Coil (%)	36.77	43.42	36.91	46.96	37.91	55.16	39.03	37.91
Averaged over last 20 ns	···	42.04	···	43.55	···	56.40	···	35.97
Turn (%)	17.82	10.63	17.82	10.04	**17.53**	**25.56**	14.71	13.43
Averaged over last 20 ns	···	11.54	···	11.86	···	20.98	···	13.26
β-strand/turn (ratio)	1.21	1.85	1.18	1.91	**1.17**	**0.13**	1.44	1.66

[1] A reference D-domain structure from this work. The parameters are calculated for t_f=60 ns.

[2] With respect to the distance between an atom from the D-domain and the graphene surface.

[3] % of secondary structure content taken the D-domain as 100%

According to Fig. 5.14, all three D-domain orientations at the surface of graphene demonstrate a consistent adsorption with an averaged closest distance from the surface about 2.4 Å (Table 5.2). In contrast, self-assembled monolayer constructed of PEG units shows less consistency in terms of distance to the hydrophobic D-domain (Fig. 5.15, Table 5.3) with significantly increasing distance from 5.36 Å to 36.90 Å during 30 ns of the simulation time.

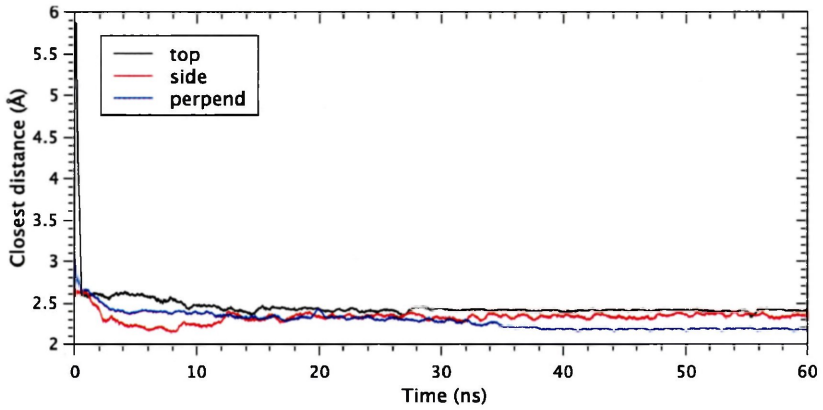

Figure 5.14: The closest distance between D-domain and the surface of graphene for three starting orientations during 60 ns of the simulation. The D-domain has a consistent adsorption, as it is shown by maintained (constant) distance.

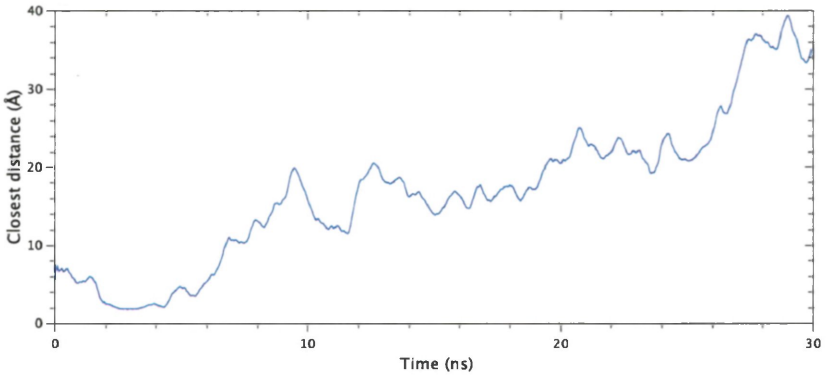

Figure 5.15: The closest distance between D-domain and the surface of PEG for 'perpendicular' orientation during 30 ns of the simulation. The D-domain repels from the monolayer, as shown by the increasing distance between them.

The radius of gyration analysis showed the most significant change in compactness for D-domain on the surface of graphene with the starting 'perpendicular' orientation (Fig. 5.16, Table 5.2). In contrast, radius of gyration for the D-domain interacting with PEG monolayer remains constant, within the same range as for the native state i.e. 36.5-37.0 Å (Table 5.2, Table 5.3). The higher *Rg* results from spreading of the protein at the surface, with consequent unfolding relative to the native structure. This apparent unfolding will be discussed further in synergy with other structural parameters below.

The percentage of conserved hydrogen bonds for 'perpendicular' orientation within D-domain is higher as a result of interactions with PEG monolayer in comparison to graphene surface, 97% and 68%, respectively (Table 5.3, Table 5.4).

Table 5.3: Calculated structural parameters for the D-domain of fibrinogen interacting with PEG self-assembled monolayer. The initial and final stages correspond to t_i=0 ns and t_f=30 ns, respectively.

Position/State	Perpendicular		Native (Unbound)[4]	
Parameter/Time	initial	final	initial	final
The closest distance[5] (Å)	**5.36**	**35.02**	...	...
Radius of gyration (Å)	36.43	36.47	36.46	36.91
Potential Energy (kJ/mol)	$-43,444$	$-32,938$	$-42,222$	$-59,387$
SASA P2 (Å^2)	94.38	117.67	100.76	108.23
RMSD P2 (Å)	0	8.02	0	2.92
α-helix [6] (%)	22.35	25.88	24.32	27.02
β-strand (%)	20.37	20.23	21.22	21.64
Coil (%)	38.33	39.88	39.03	36.02
Turn (%)	15.28	12.45	14.71	13.01
β-strand/turn (ratio)	**1.33**	**1.62**	1.44	1.66
Hydrogen bonds within D-domain (intramolecular)	706.00	**516.00**	750.00	**532.00**
Adsorbed/native (ratio)		**0.97**		

[4]A reference D-domain structure from this work. The number of hydrogen bonds are calculated for intramolecular or protein-protein (within three chains) interactions. The parameters are calculated for t_f=30 ns.

[5]With respect to the distance between an atom from the D-domain and the graphene surface.

[6]% of secondary structure content taken the D-domain as 100%

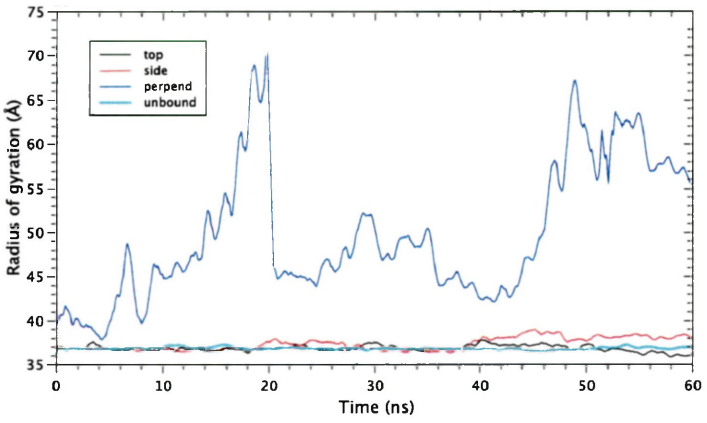

Figure 5.16: Radius of gyration for D-domain at the surface of graphene for three starting orientations during 60 ns of the simulation. The parameter indicates folding/unfolding changes in the protein by calculating its dimensions, presenting compactness and describing the general spread of the biomolecule over an area.

Graphene has a highly hydrophobic nature, with contact angle for a drop of water of 127° [309], which is much more than 90° (a contact angle higher than 90°) indicative of hydrophobic properties of the surface) (Fig. 5.2 (a)) [310]. In contrast, fibrinogen has amphipathic helices packed together in such a way that forms exposed hydrophobic surfaces (D-domains), and leaves hydrophobic regions buried in its core (E domain). Therefore, one should expect hydrophobic interactions to be the most significant contributor to the adsorption to graphene. Also, the number of hydrophobic interactions between D-domain and graphene surface at the initial and final stages of the simulation was calculated. For example, according to Fig. 5.14, fibrinogen D-domain became to interact with the surface, but have not yet started to rearrange at 2 ns simulation time (closest distance of D-domain from the surface is

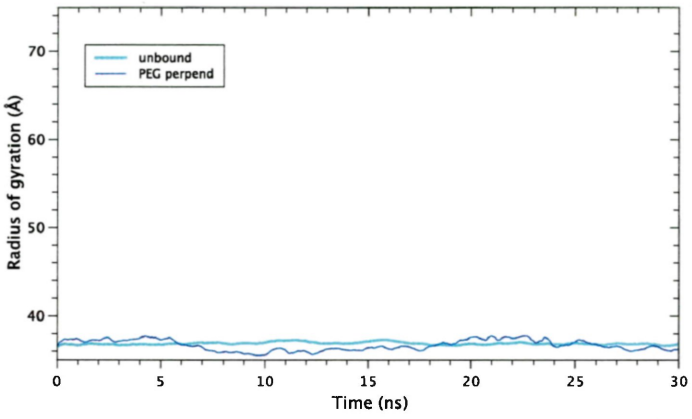

Figure 5.17: Radius of gyration for D-domain at the surface of PEG monolayer for 'perpendicular' orientation during 30 ns of the simulation. The parameter indicates no unfolding processes in the protein by presenting its maintained compactness.

about 2.5 Å). The number of hydrophobic interactions between fibrinogen D-domain and the surface for 'side' and 'perpendicular' positions within 7 Å has been significantly increased from 534 and 1,301 interactions to 4,268 and 23,387 for 2 ns and 60 ns, respectively (Table 5.2). The strength of hydrophobic contacts is based on knowledge-based potentials [311] in which each individual interaction can be scored from 0 to 1 (unitless). In summary, during the 60 ns simulation time, the D-domain attaches more tightly to the surface, for example, by exposing its hydrophobic helical segments, therefore more hydrophobic bonds were created.

To quantify the secondary structure rearrangements of the D-domain after adsorption, the numbers of intermolecular (between chains) and within the whole D-domain (includes both intermolecular (between chains) and also intramolecular (within chains)) hydrogen bonds were computed (Table 5.4). Fig. 5.18 illustrates the number of intermolecular hydrogen bonds within D-domain (count domain-domain interactions)

before and after simulation. It highlights similar behaviour of two initial ('top' and 'side') positions of the fragment as a result of adsorption, as well as a considerably reduced number of hydrogen bonds (about 1.5 times less) for adsorbed 'perpendicular' orientation in comparison to its unbound state. It also should be noted that the number of hydrogen bonds might be restored by the end of the simulation time, even if there were changes in the fragment's secondary structure. A slight difference in the values for 0 ns simulation time is attributed to two-step minimization of each individual starting system (see Sec. 5.3 for details). The numbers of the intramolecular hydrogen bonds between α, β and γ chains of the D-domain were also determined (Fig. 5.19, Fig. 5.20). Although the average number of the intramolecular hydrogen bonds for adsorbed positions as well as reference state remain at the same range, there is sharper fluctuations for the systems with D-domain bound to a graphene sheet as well as decreased values for 'perpendicular' system in comparison to the unbound state.

Table 5.4: Number of hydrogen bonds for the D-domain of fibrinogen adsorbed to a graphene surface (includes both intermolecular (between chains) and also intramolecular (within three chains) interactions) with standard deviation less than 1%. The initial and final stages correspond to t_i=0 ns and t_f=60 ns, respectively, otherwise it is specified.

Position/State	Top		Side		Perpendicular		Native (Unbound)[7]	
Parameter/Time	initial	final	initial	final	initial	final	initial	final
Hydrogen bonds within D-domain (intramolecular)	744.00	**500.00**	737.00	**513.00**	734.00	**390.00**	750.00	**575.00**
Adsorbed/native (ratio)	···	0.87	···	0.90	···	**0.68**	···	···
Hydrogen bonds (α and β-chains) (intermolecular)	19.0	10.0	19.0	16.0	**18.0**	**1.0**	19.0	14.0
Averaged over last 20 ns	···	11.17	···	14.94	···	4.29	···	11.30
Hydrogen bonds (α and γ-chains) (intermolecular)	6.0	4.0	6.0	3.0	7.0	6.0	6.0	5.0
Averaged over last 20 ns	···	4.00	···	4.22	···	4.49	···	4.82
Hydrogen bonds (β and γ-chains) (intermolecular)	19.0	10.0	19.0	16.0	21.0	16.0	22.0	15.0
Averaged over last 20 ns	···	12.06	···	8.66	···	9.30	···	12.47

[7]A reference D-domain structure from this work.

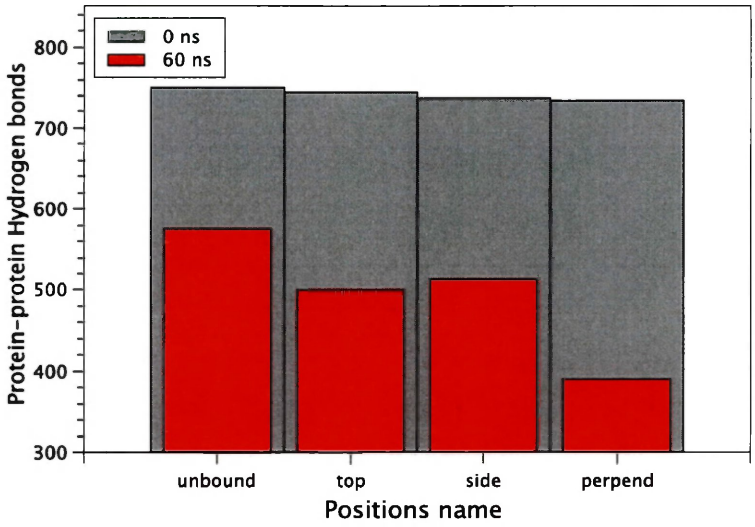

Figure 5.18: Number of the total intra- and interchain hydrogen bonds between different chains of the D-domain before and after the simulation was completed.

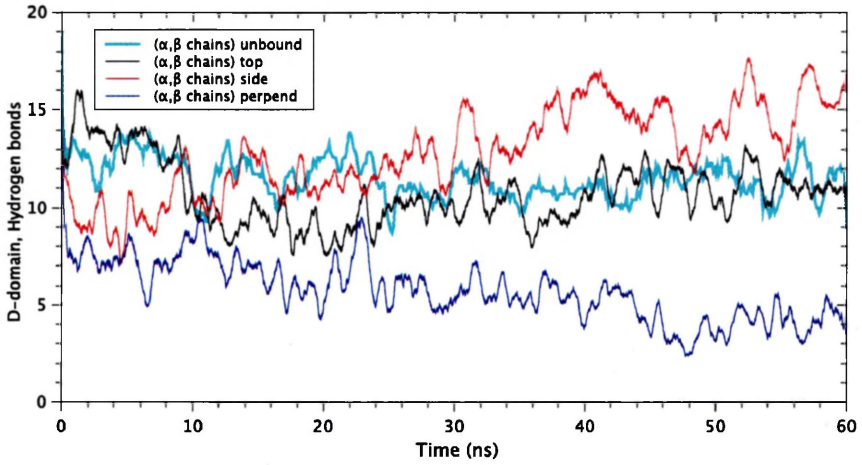

Figure 5.19: Number of hydrogen bonds between α and β chains of D-domain unbound (native) as well as with the 'top', 'side' and 'perpendicular' orientations to the graphene surface during 60 ns of the simulation.

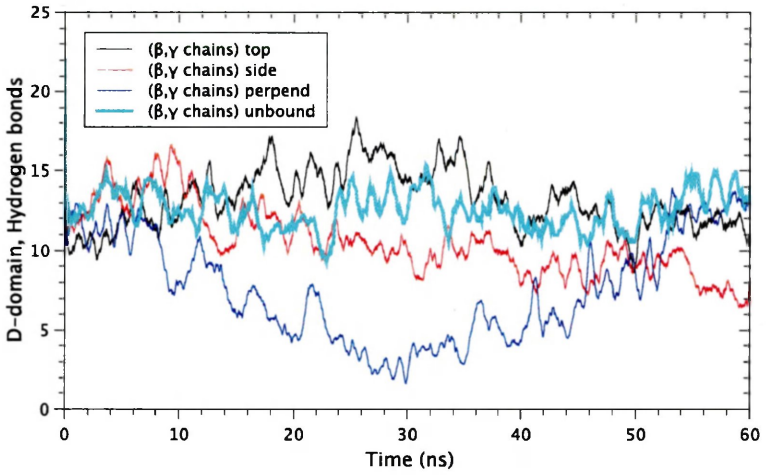

Figure 5.20: Number of hydrogen bonds between β and γ chains of D-domain unbound (native) as well as with the 'top', 'side' and 'perpendicular' orientations to the graphene surface during 60 ns of the simulation.

In support of D-domain adsorption and structural changes of P1, P2, and specifically P2-C portion, the secondary structure of the fibrinogen was partially destroyed and graphene surface shows selective protection for some α-helices, β-strands, turns and coils (see Fig. 5.21 - Fig. 5.24).

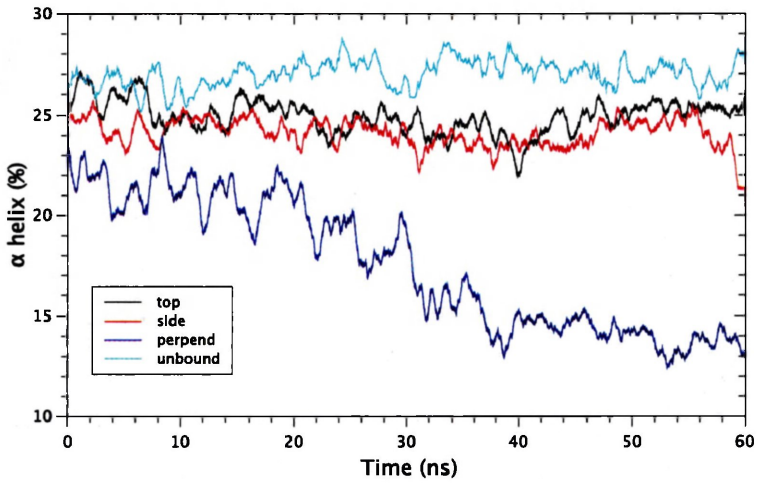

Figure 5.21: Secondary structure content (%) (α-helix) of fibrinogen D-domain at the surface of graphene. The curves correspond to the 'top' (black), 'side' (red), 'perpendicular' (blue) systems as well as fragment's unbound state (cyan) that represents its native structure.

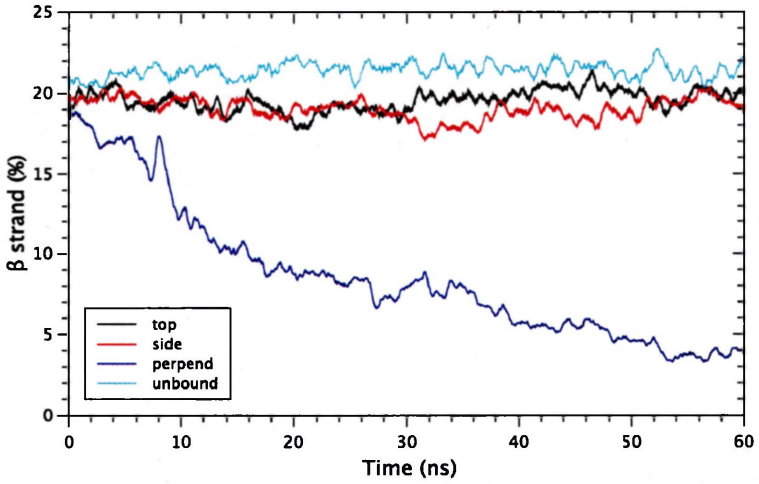

Figure 5.22: Secondary structure content (%) (β-strand) of fibrinogen D-domain at the surface of graphene. The curves correspond to the 'top' (black), 'side' (red), 'perpendicular' (blue) systems as well as fragment's unbound state (cyan) that represents its native structure.

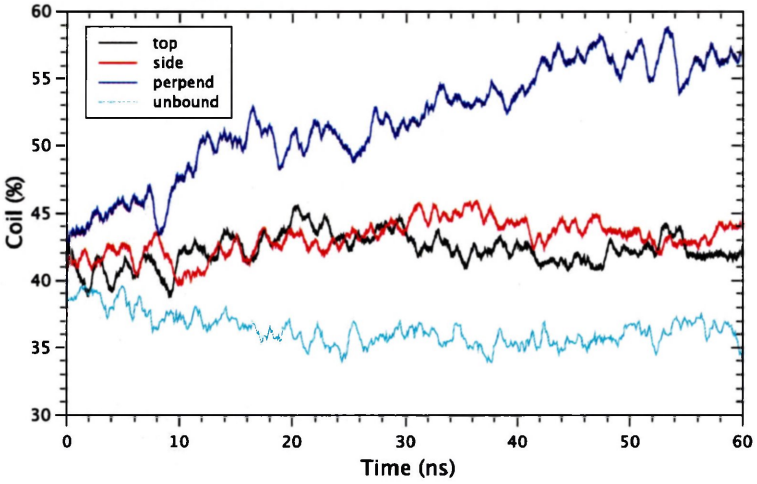

Figure 5.23: Secondary structure content (%) (coil) of fibrinogen D-domain at the surface of graphene. The curves correspond to the 'top' (black), 'side' (red), and 'perpendicular' (blue) systems as well as fragment's unbound state (cyan) that represents its native structure.

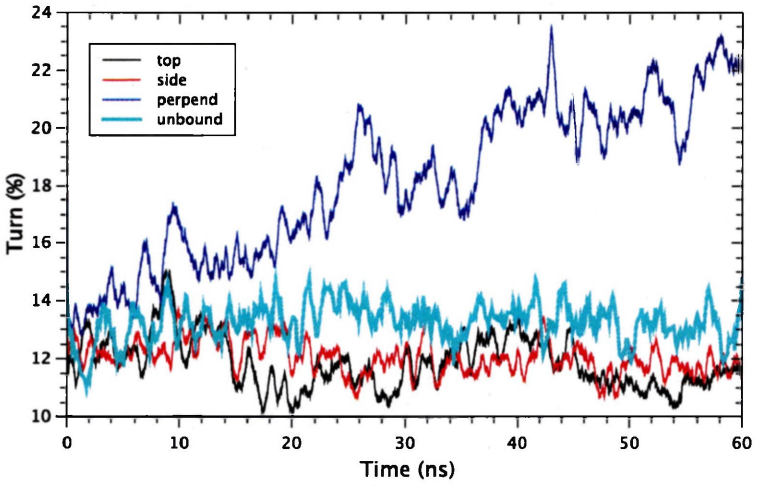

Figure 5.24: Secondary structure content (%) (turn) of fibrinogen D-domain at the surface of graphene. The curves correspond to the 'top' (black), 'side' (red), and 'perpendicular' (blue) systems as well as fragment's unbound state (cyan) that represents its native structure.

Hydrophobic interactions between the D-domain and graphene surface may be a reason for breakdown in the protein's secondary structure. Fig. 5.21 - Fig. 5.24 show changes (%) in secondary structure content of D-domain during simulation. Some interesting trends are observed in these figures. Unfolding of the adsorbed D-domain occurred as a result of 'top' and 'side' (or side-on position) adsorption, as can be seen from Fig. 5.21 - Fig. 5.24. However, the most crucial changes are found to be for 'perpendicular' position. The secondary structure content of the fragment, α-helices, β-strands is retained almost completely in water (native state), indicating that the native structure of D-domain was preserved concurring with Fig. 5.21, Fig. 5.22, Fig. 5.23, Fig. 5.24. However, during the simulation some portions of the α-helices (Fig. 5.21) and β-strands (Fig. 5.22) disappear. The corresponding strands retain some helicoidal feature. In general, β-strands are hydrophobic and less robust against unfolding than their counterparts, α-helices. There is a slight decrease in α-helix content for hydrophobic surfaces in agreement with comprehensive experimental study conducted by Tunc et. al [94] and by Sivaraman et. al [312].

Also, based on Fig. 5.9, Fig. 5.11 and experimental work by Wang et. al [95], hydrophobic graphene surface causes fast, consistent and strong adsorption (within first 10 ns of the simulation time (Fig. 5.14)) of the D-domain oriented in 'top' and 'side' positions. We hypothesize that the D-domain undergoes only moderate secondary structure changes because it ends up in a favourable orientation finding its energy minimum.

The results for 30 ns of simulation time show that perpendicularly-oriented fibrinogen D-domain does not adsorb to the surface consisted of self-assembled PEG-chains (Fig. 5.7). This result is in agreement with Burchenal et. al [313] that found de-

creased fibrinogen adsorption to a surface coated with PEG, which is considered as a promising biocompatible material [288, 289, 292, 314–316]. Evan [294] suggested that the reason for protein's resistance to adsorb to PEG is due to the fact that water molecules hydrate PEG units creating a hydration shell through hydrogen bonds. Although there is some loss in hydrogen bonding for D-domain interacting with PEG monolayer (Table 5.3). There is conservation of the D-domain secondary structure as a results of their interactions (Fig. 5.25, Fig. 5.26, Fig. 5.27, Fig. 5.28).

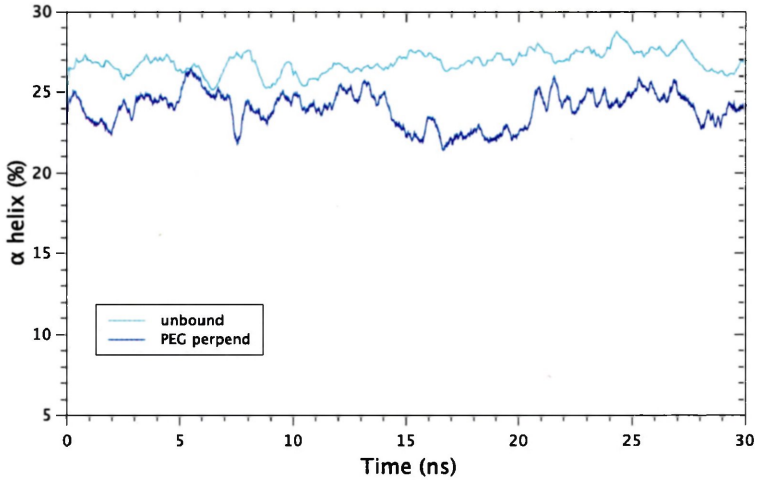

Figure 5.25: Secondary structure content (%) (α-helix) of fibrinogen D-domain on the PEG monolayer. The curves correspond to the 'perpendicular' (blue) and D-domain's unbound (native) structure (cyan).

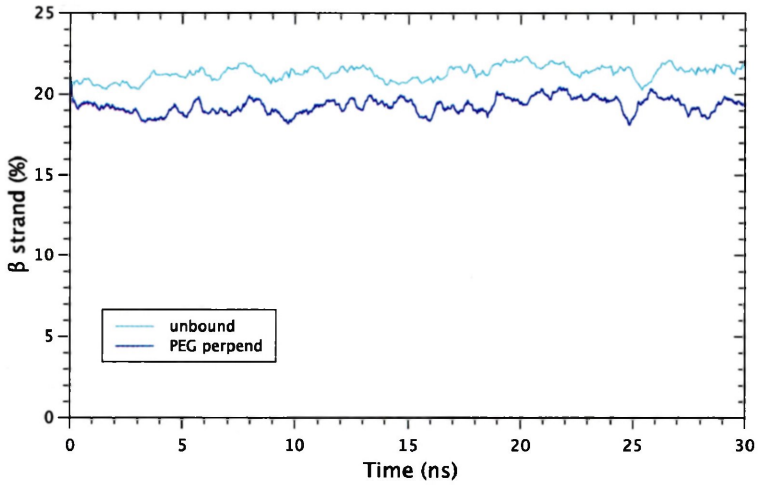

Figure 5.26: Secondary structure content (%) (β-strand) of fibrinogen D-domain on the PEG monolayer. The curves correspond to the 'perpendicular' (blue) and D-domain's unbound (native) structure (cyan).

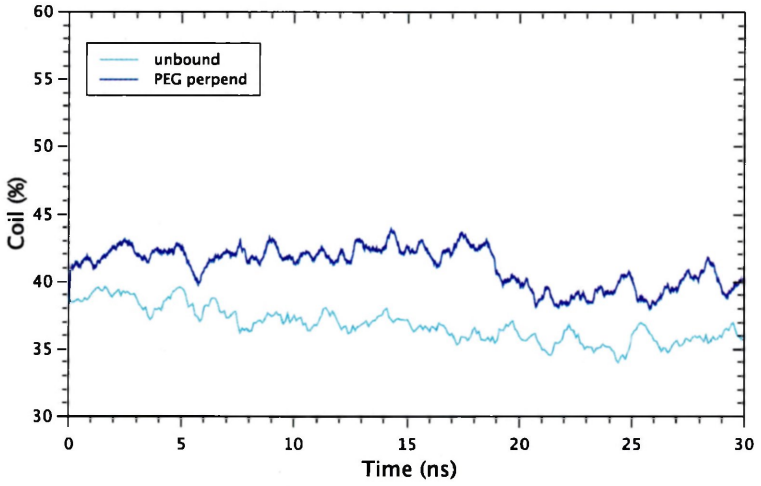

Figure 5.27: Secondary structure content (%) (coil) of fibrinogen D-domain on the PEG monolayer. The curves correspond to the 'perpendicular' (blue) and D-domain's unbound (native) structure (cyan).

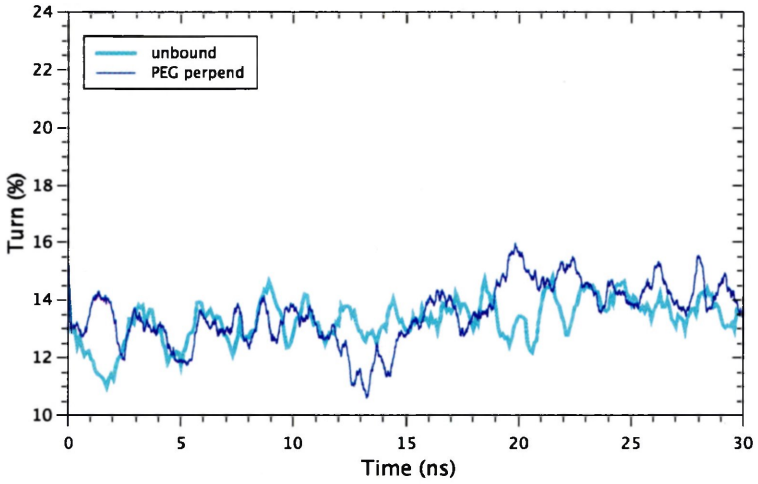

Figure 5.28: Secondary structure content (%) (turn) of fibrinogen D-domain at the PEG monolayer. The curves correspond to the 'perpendicular' (blue) and D-domain's unbound (native) structure (cyan).

To obtain additional information on the deformation (reorganization) of the D-domain at the surface of graphene as well as PEG monolayer, D-domain secondary structure content by residue with respect to the native protein structure was analyzed (see Sec. 5.7: Fig. 5.31 - Fig. 5.35). In particular, the secondary structure content for P1 and P2 cryptic sites for both cases, adsorption onto graphene and resistance to PEG, were summarized in Fig. 5.29 and Fig. 5.30. It can be seen from Fig. 5.29 (a) that P1 binding sequence conserves fully its secondary structure within unbound (native) D-domain as well as D-domain adsorbed to the graphene surface with side-on (top and side) orientations analyzed every 20 ns of the simulation period. However, at 60 ns of simulation time, there is a complete damage of secondary structure of the P1 motif when D-domain is oriented perpendicularly (end-on) to the graphene sheet. Specifically, the P1 sequence looses its β-extended strand and bend. On the contrary, the secondary structure of the P1 sequence within D-domain perpendicularly oriented to PEG self-assembled monolayer maintains its secondary structure absolutely (Fig. 5.29(b)). The same trend can be noticed for P2 (or P2-C) cryptic sequence (Fig. 5.30(a,b)). Only slight deviations in the secondary structure for P2 (or P2-C) motif within D-domain bound to the graphene substrate with 'top' and 'side' orientations are found such as some damage of hydrogen-bonded turns and bends (Fig. 5.30(a)). Similarly to P1, P2 (P2-C) sequence undergoes the most significant structural changes (damage of the β-extended strand) when D-domain is perpendicularly adsorbed to the graphene surface. For the P2 (P2-C) site as a part of D-domain with end-on (perpendicular) orientation to the PEG monolayer, there is a quite good maintenance of the secondary structure (Fig. 5.30(b)). For the entire D-domain, the amount of residual secondary structure also differs for graphene

and PEG substrates: a significant maintained population of α-helices is shown for D-domain as a result of interactions with PEG monolayer (Sec. 5.7: Fig. 5.35), while the α-helices of D-domain are found to be unstable on the graphene surface (Sec. 5.7: Fig. 5.31 - Fig. 5.33).

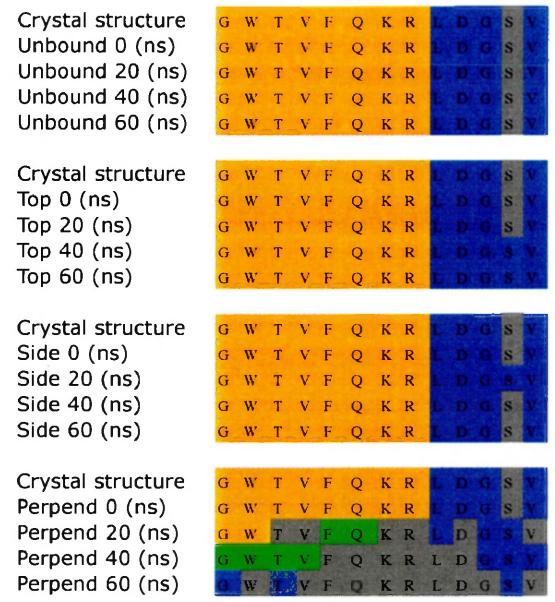

a)

b)

Figure 5.29: Secondary structure content per residue of P1 portion of fibrinogen D-domain at the surface of graphene (a) and PEG monolayer (b). The colours refer to β-extended strand (orange), bend (blue), hydrogen-bonded turn (green), and undetermined/random coil (grey).

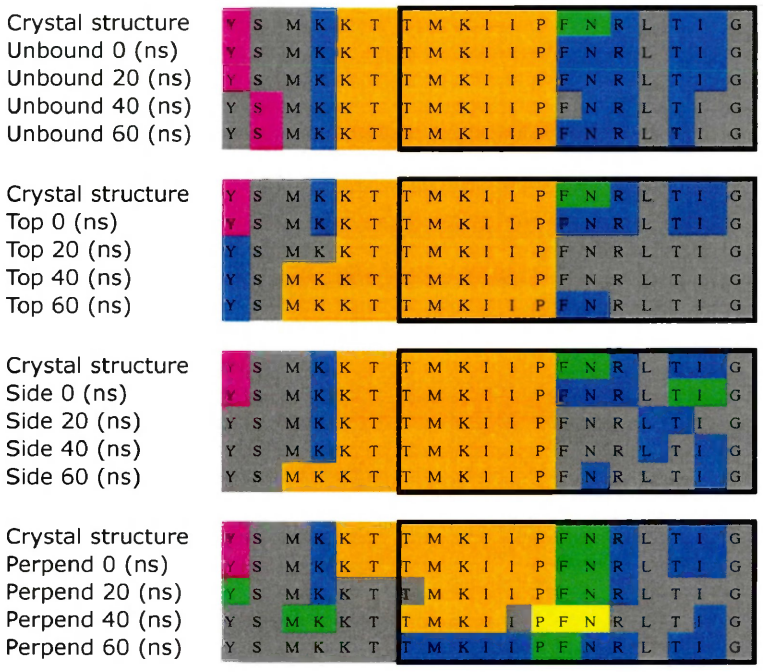

a)

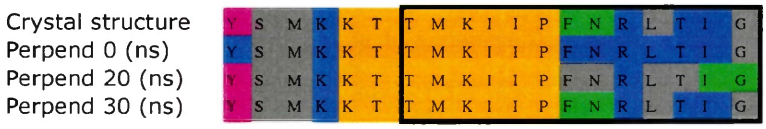

b)

Figure 5.30: Secondary structure content per residue of P2 and its P2-C (TMKI-IPFNRLTIG) portion (a bold box) of fibrinogen D-domain at the surface of graphene (a) and PEG monolayer (b). The colours refer to β-extended strand (orange), bend (blue), β bridge (purple), hydrogen-bonded turn (green), G-helix (yellow), and undetermined/random coil (grey), respectively.

5.5 Discussion and comparison with experiments

5.5.1 Adsorption-induced fibrinogen structural changes

The ability of accessible bioactive motifs (hidden sites) of fibrinogen to bind and, consequently, activate wide range of immune cells was previously shown [266]. These inflammatory mechanisms and processes are discussed in detail in Chapter 1, subsection 1.2. Particularly, peptide sequences P1 and P2 within fibrinogen D-domain were found to interact with a leukocyte integrin $\alpha_M\beta_2$ (Mac-1) [52, 75, 76, 92, 267, 268, 317]. The P2-C portion of P2 sequence [268, 317, 318] is recognized by both the α_M and β_2 subunits, whereas P1 is recognized by only the α_M subunit. Most importantly, Flick et. al [74] proved that P2-C portion γ 390-396 is very specific because when it was modified by an alanine mutation, the protein failed to trigger adhesion of immune cells containing CD11b/CD18 integrin, as well as failed to promote clotting fibrous formation.

A previous report of MD simulations of fibrinogen γ-chain (5 ns of time scale, GROMACS (v. 3.1.4) MD simulation package, GROMACS force field) on self-assembled monolayers showed no significant structural changes for the protein fragment [282]. The authors also suggested that some substantial rotational and translational motions of the γ-chain as a result of interactions with the surface may occur. However, probably because of the short simulation time or the size of the fibrinogen fragment, these conclusions were not able to demonstrate a direct link between surface chemistry/wettability, degree of protein structural changes, inaccessible sites behaviour and biocompatibility. In comparison, the obtained results are for longer simulation time (60 ns). Also, the specificity of the hidden sequences makes it excit-

ing to monitor their behaviour as a result of the entire D-domain adsorption to the hydrophobic graphene.

As it is shown in Fig. 5.4 (b), Fig. 5.5 (b) and Fig. 5.6, there is an evident protein conformational changes upon adsorption to graphene surface that is also supported by structural analysis data. The 'side' and 'perpendicular' initial positions of D-domain demonstrate some changes of $RMSD$ parameters. Although in the primary peptide chain (according to amino acids order in the primary protein structure), the P1 γ190-202 and P2 γ377-395 motifs are located further apart of each other, these sites appear to be close packed neighbours representing antiparallel β strands (Fig. 5.1). Consequently, changes in an accessibility of one motif may affect another, and as result, their interaction with leukocyte Mac-1 integrin.

Under physiological conditions, graphene surface adsorbs proteins due to hydrophobic interactions. Electrostatic interactions between protein-graphene do not affect interactions because of neutral nature of graphene. The strength of D-domain-graphene interactions can be explained by weak surface-water interactions that are not able to overcome multiple hydrophobic non-bonded attraction for protein-substrate. Water is repelled from highly hydrophobic pure graphene surface because formation of interface is energetically unfavorable. For the hydrophilic surfaces, the protein is supposed to be screened from the surface by a high density water layer and desorbs. Adsorption versus desorption behaviour is pre-determined by interplay between all participants in the system, such as protein, surface and solute contributions. We have found that solvent interactions at the hydrophobic graphene surface restructure the fibrinogen D-domain, and contribute to the adsorption energy (Table 5.1). Number of hydrogen bonds between the adsorbate and the graphene surface changes due to con-

formational rearrangements that the fragment undergoes. The adsorption is mostly driven by van der Waals interactions. The non-polar residues and aromatic residues of D-domain may adsorb to the surface of graphene due to van der Waals ($\pi - \pi$ stacking) interactions (see Chapter 3). This is in agreement with experimental work by F. Sharifi et al. [319], who showed a close linear correlation with the van der Waals contributions of the adsorption energies of different amino acids with graphene. The reason for the sharp rise in the number of hydrophobic interactions is that surfaces with the greatest number of carbons will have the strongest hydrophobic interactions. These observations are in line with Ta et. al [99], who proposed that fibrinogen binds to the graphite hydrophobically through the D-domains (weak adsorption on mica and strong featuring significant structural changes for highly ordered pyrolytic graphite).

The obtained results show that adsorbed fibrinogen fragment is not fully unfolded as a result of adsorption to hydrophobic graphene surface, it strongly conserves partially ordered secondary structure for all but one starting orientation. The percent (%) of secondary structure content crucially changes for 'perpendicular' orientation, and the obtained results show decreased β-strand/turn ratios caused by D-domain adsorption to graphene surface in contrast to PEG monolayer (Table 5.2, Table 5.3). This result is consistent with experimental findings by Steiner et. al [320]. The authors investigated fibrinogen adsorption on hydrophobic and hydrophilic silicon surfaces. Based on their findings, they concluded that lower β-strand/turn ratios appear on hydrophobic surfaces and higher ratios for hydrophilic surfaces. In our results, the amount of β-strand is much higher for PEG in comparison to graphene surface, in agreement with Steiner et. al [320], who showed increasing amount of β-strand for fibrinogen at the hydrophilic silicon surface.

The detailed analysis of the secondary structure content for the D-domain with 'top' and 'side' orientations adsorbed to graphene surface shows very little changes in the content of extended β-strand and α-helices (see Sec. 5.7: Fig. 5.31, Fig. 5.32). The local structure of the P1 and P2 sites remained unchanged as a result of interaction with graphene sheet. The changes on the secondary structure content for the entire D-domain at the PEG monolayer are small and related only to the unfolding of a few extended β-strands regions (see Sec. 5.7: Fig. 5.35). The P1 and P2 sites conserve their structure during D-domain interactions with hydrophilic PEG monolayer. The same is true for D-domain secondary structure in water (Fig. 5.34). However, the 'perpendicular' orientation of the D-domain on the hydrophobic graphene surface shows significant secondary structure changes in the helical (coiled-coil) part of the D-domain as well as its P1, P2 binding sites (Sec. 5.7: Fig. 5.33).

An experimental work by Desroches et. al [321] found that fibrinogen α-helix structure undergoes small structural changes upon adsorption to a stainless steel surface with a contact angle about 61°, while β-sheet decreases and turn increases more significantly. According to Berg's limit, this surface is considered to be more hydrophobic than hydrophilic i.e. it will be able to cause protein structural changes. The secondary structural parameters obtained by Desroches et. al [321] for fibrinogen adsorbed to a stainless steel are in agreement with our findings for graphene surface (Table 5.2).

In this work, an assumption is made that D-domain dominantly interacts only with the surface/monolayer, the interactions with other proteins/biomolecules are not considered. As it is shown in the literature, the increased fibrinogen concentration leads to its end-on ('perpendicular') orientation as a result of adsorption to the

surface [81, 274]. The density of adsorbed fibrinogen is 7 times higher for end-on in comparison to side-on orientation [274, 294]. It should be noted that the surface promotes an immunological response if the density of adsorbed fibrinogen is at least 10 ng/cm^2 [294, 322]. This fact suggests that graphene, because it leads to stable 'perpendicular' adsorption of fibrinogen, may possess non-biocompatible properties. Moreover, according to the obtained results, 'perpendicular' orientation shows the most significant surface-dependent conformational changes, in comparison to side-on ('top', 'side') positions, that can cause binding to leukocyte Mac-1 integrin, and consequently, trigger cascade of immune reaction and inflammation. In this work the interactions of a single D-domain adsorbing to the graphene surface is modelled. It is capable to mimic the behaviour of a protein surrounded and supported by other proteins (taking into account the required concentration) due to the difference in time scale for the cooperative adsorption kinetics of group of interacting proteins (few minutes) and an adsorption kinetics for an individual protein (few nanoseconds) used in this work. As a result, the D-domain perpendicularly placed on the surface of graphene shows no migration over the surface during 60 ns of the simulation time, and this is consistent with experimental works by Santore et al. [274] and by Rabe et. al [81] for group of fibrinogens that have vertical orientation as most favourable.

The obtained results confirm stabilizing protein-surface interactions on highly hydrophobic graphene (i.e. positive control) surface, and resistant properties to strongly hydrophilic PEG (negative control) surface. The binding energies and closest distances are consistent with experimental observations [97, 99, 135, 269–274, 277] where fibrinogen is stabilized by adsorption onto hydrophobic surfaces. Also the degree of biocompatibility as well as protein binding strength to the PEG may depend on the

density of PEG chains and other factors.

To summarize, according to Table 5.2, perpendicularly-oriented D-domain undergoes the most crucial conformational changes upon adsorption to pure graphene surface, while PEG shows no effect on the structure of the D-domain (Table 5.3).

Simulation time range of 60 ns may not be enough to observe the final adsorption state following total protein unfolding because in average, the unfolding process takes a few minutes, however, the general trend can be explored using MD simulations. Further investigations on the exact confirmations of binding sites, as a result of fibrinogen adsorption to non-biocompatible surface, relative to its ability to promote immune cells reaction need to be done.

For the purposes of orthopaedic applications, design of the material that could be able to selectively adsorb fibrinogen is beneficial. For example, natural killer cells (leukocytes) express Mac-1 receptor [323–325] and recruit mesenchymal stromal cells that differentiate into osteoblasts (bone repair/regeneration), at the same time natural killer cell adhesion does not lead to cytokine secretion. Also, Almeida et. al [326] reported that adhesion of natural killer cells is higher on materials with adsorbed fibrinogen.

5.6 Conclusions

In addition to experimental techniques investigating foreign body reaction, substantial advances in computational methods and analysis have been made recently. Most importantly, experimental methods have difficulties to determine complex molecular structures and mechanisms. Although the processes including protein folding and

unfolding occur at the time scale that is more than a few nanoseconds, it is possible to get important knowledge related to conformational changes of adsorbed to the surface protein using the MD simulations.

Performance of an implanted device is affected by the dynamics and specificity of blood proteins. The adsorbed proteins treat a coating layer on the implant surface and can be recognized as a trigger for biological responses to foreign materials. Both the properties of the proteins as well as of the surface define the probability of the immune response. Therefore, the detailed knowledge of the processes accompanying protein adsorption is essential to model the surface of the implant that will be compatible with living tissue.

Although the exact mechanism behind the changes in fibrinogen cryptic sites' activity is not defined in literature, advances in computational biochemistry tools have greatly assisted in the study of fibrinogen adsorption behaviour. The literature on fibrinogen conformational assessment (particularly, P1 and P2 inaccessible bioactive sites analysis) is both broad and deep; however, it does not provide understanding of the mechanisms leading to deteriorated biocompatibility.

In the present paper, the simulations provide an important insight into understanding protein-hydrophobic (graphene) and protein-hydrophilic (for example, PEG) interactions, that cannot be identified by experiments. In this study, the adsorption dynamics of a D-domain fibrinogen model onto graphene surface was investigated by MD simulations. Our results also demonstrate the utility of AMBER03 force field for protein-artificial surface interaction description. The obtained quantitative structural information on the conformational changes of D-domain after adsorption to graphene sheet includes $RMSD$, $SASA$, secondary structure content (%) as well as other valu-

able parameters were also calculated. Also, fibrinogen as a potent pro-inflammatory mediator in determining the extent of local and general inflammation as well as its unique structural properties have been discussed. Overall, the results indicate that surface chemistry plays a crucial role in the conformational changes that protein undergoes upon adsorption on an inorganic (synthetic, artificial) surface. This work contributes towards development of theoretical approaches to assessment the biocompatibility of synthetic materials. The ultimate goal of designing surfaces should be focused on controlling fibrinogen adsorption behaviour, and as a result, biological response.

5.7 Appendix

Detailed secondary structure content per residue for each of the simulation orientation such as 'top', 'side', 'perpendicular' at the surface of graphene, 'perpendicular' at the PEG monolayer as well as native state is presented in the following figures: Fig. 5.31 - Fig. 5.34. The rows correspond to a D-domain crystal structure, its structure at 0 ns, 20 ns, 40 ns, and 60 ns of the simulation time, respectively. For a PEG monolayer there is a D-domain crystal structure, its structure at 0 ns, 20 ns and 30 ns of the simulation time. For each of the orientation, outlined in black fragments correspond to the most significant changes in the secondary structure content of the D-domain such as unfolding of the α-helix and/or β-extended strand; while the outlined in red fragments are P1 γ190-202 and P2 γ377-395 binding sites.

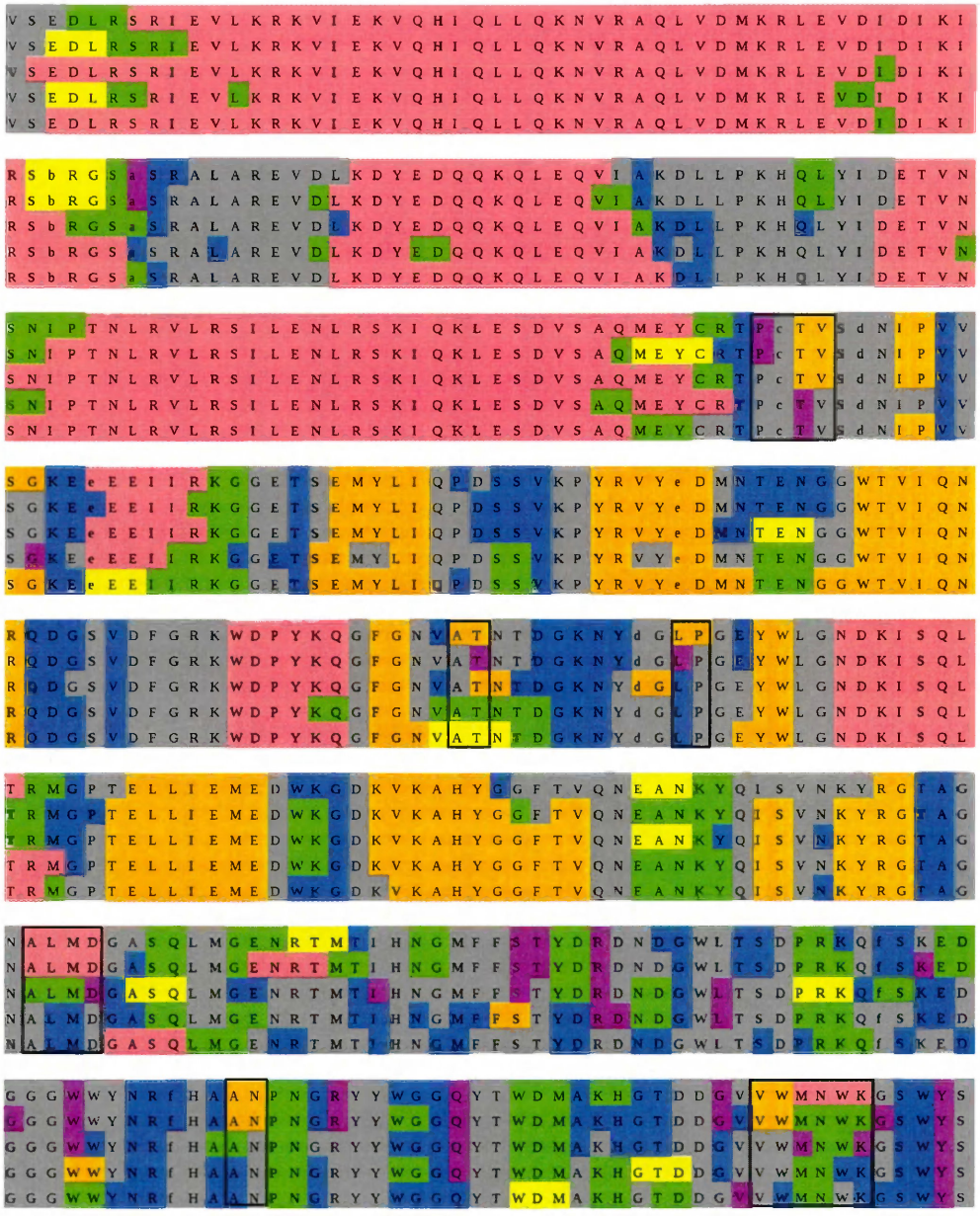

Figure 5.31: Secondary structure content per residue for D-domain at the surface of graphene (top position) every 20 ns period during 60 ns of the simulation time. The colours correspond to α-helix (pink), β-extended strand (orange), bend (blue), β bridge (purple), hydrogen-bonded turn (green), G-helix (yellow), and undetermined/random coil (grey), respectively.

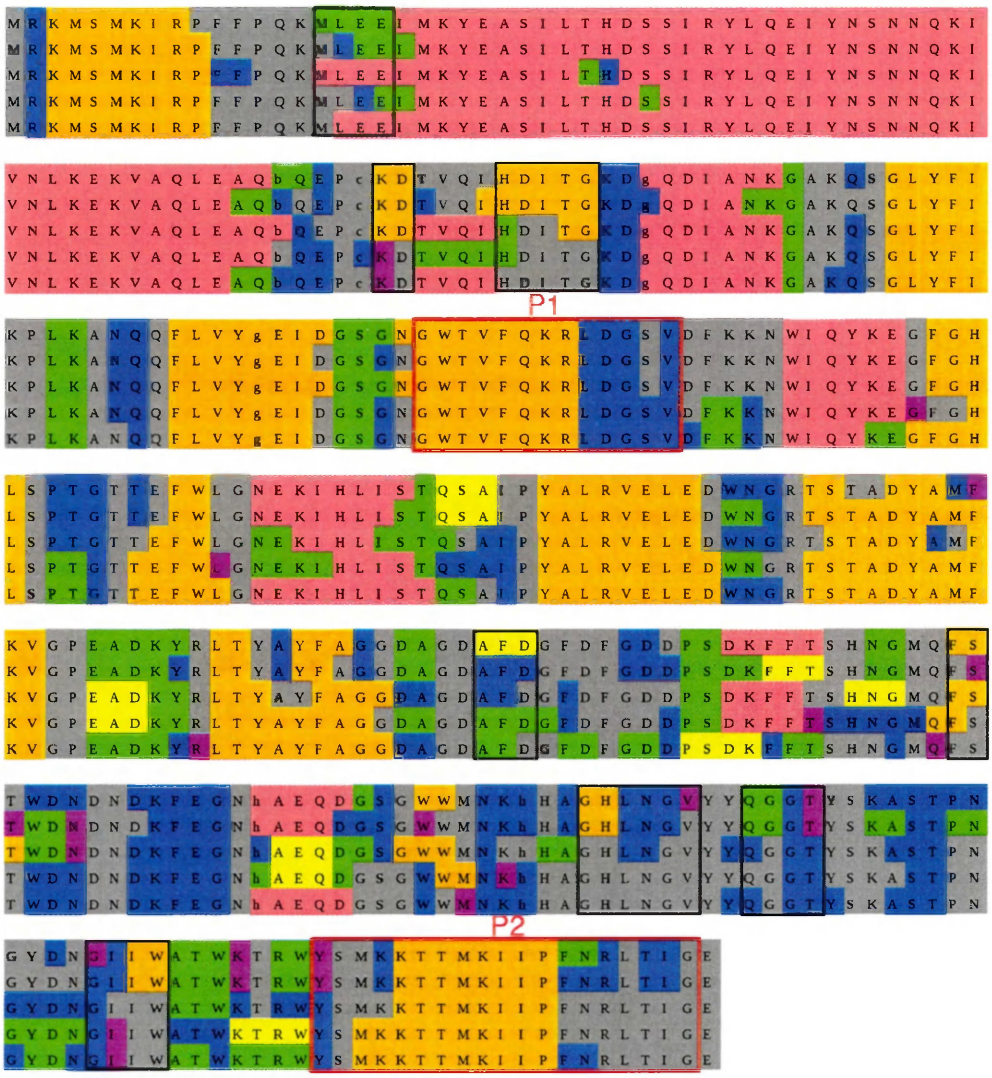

Figure 5.31: **Continued.** Secondary structure content per residue for D-domain at the surface of graphene (top position) every 20 ns period during 60 ns of the simulation time. The colours correspond to α-helix (pink), β-extended strand (orange), bend (blue), β bridge (purple), hydrogen-bonded turn (green), G-helix (yellow), and undetermined/random coil (grey), respectively.

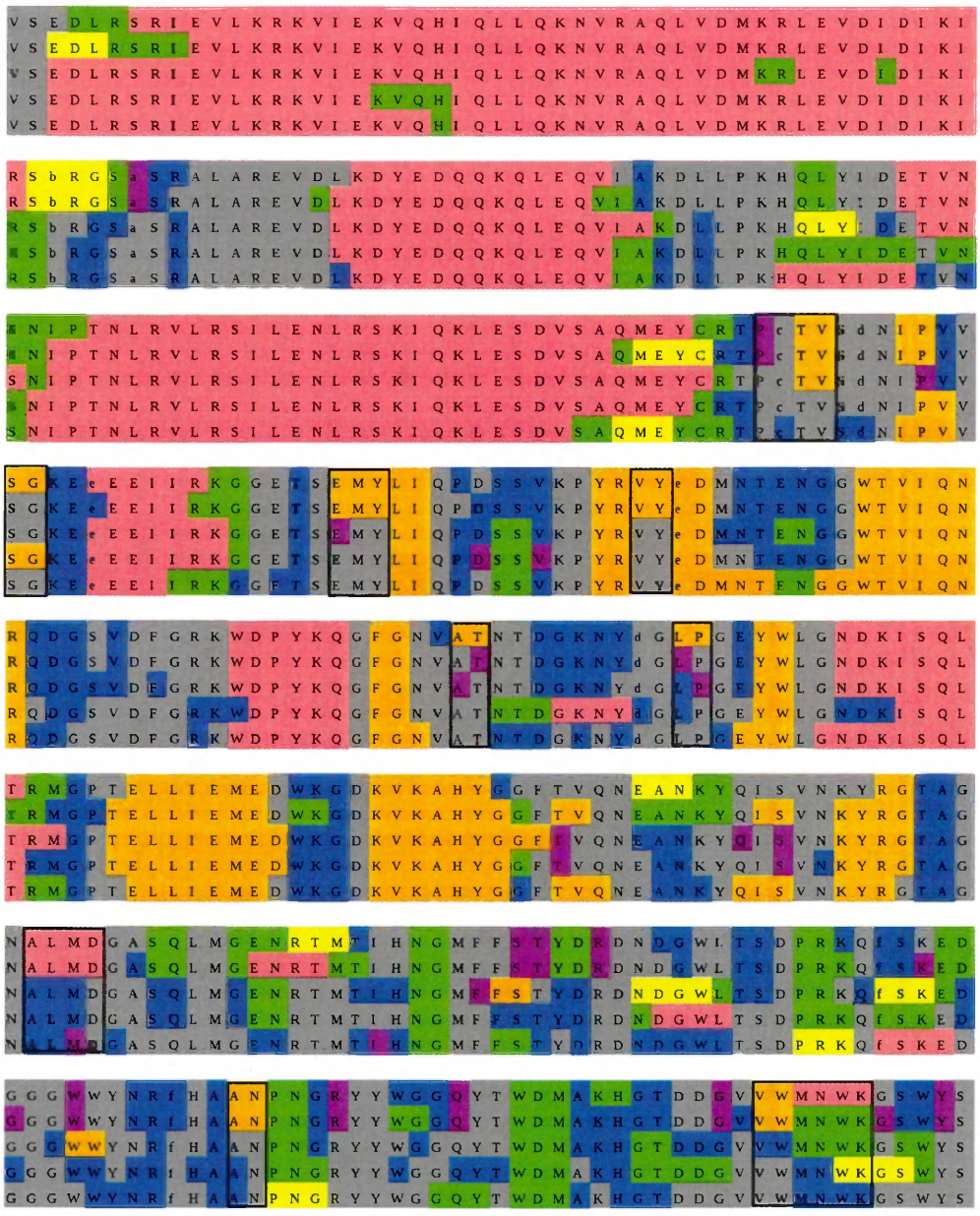

Figure 5.32: Secondary structure content per residue for D-domain at the surface of graphene (side position) every 20 ns period during 60 ns of the simulation time. The colours correspond to α-helix (pink), β-extended strand (orange), bend (blue), β bridge (purple), hydrogen-bonded turn (green), G-helix (yellow), and undetermined/random coil (grey), respectively.

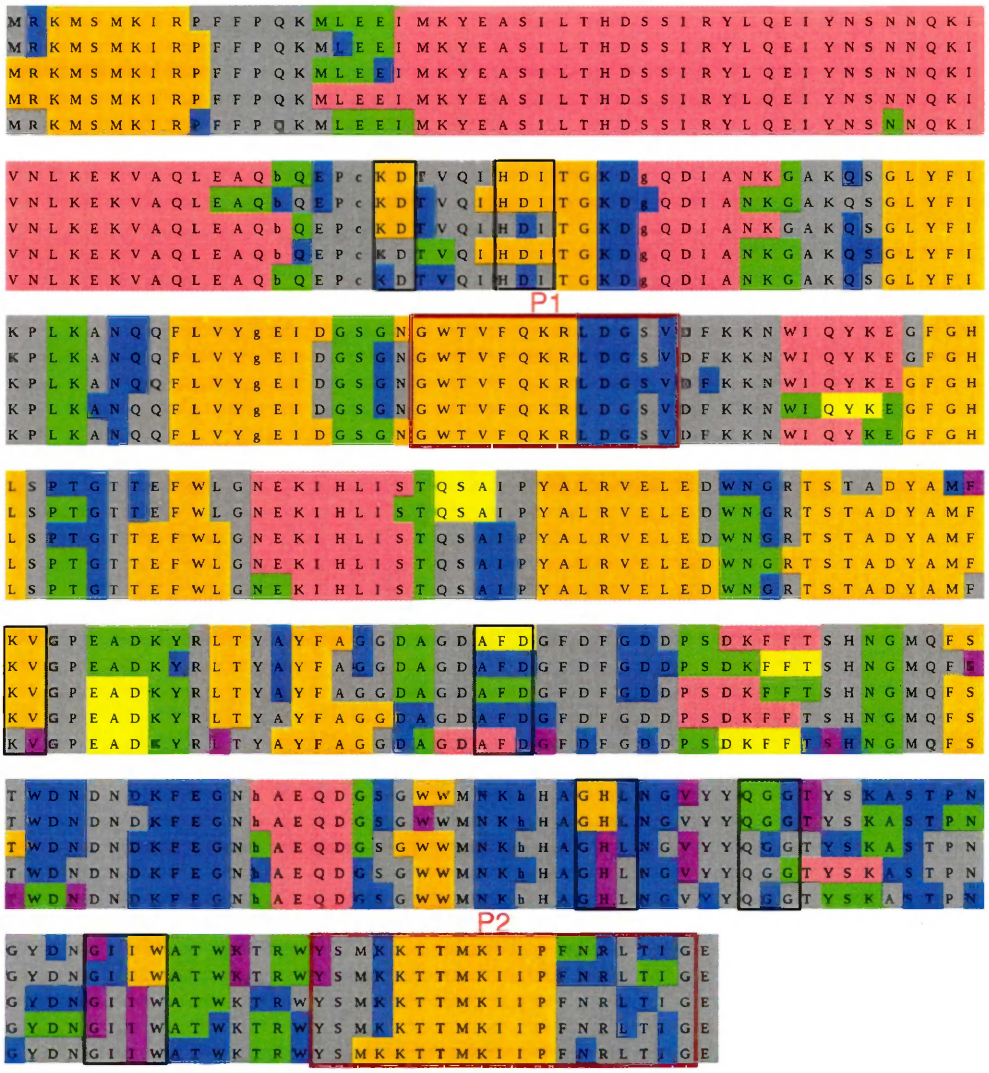

Figure 5.32: **Continued.** Secondary structure content per residue for D-domain at the surface of graphene (side position) every 20 ns period during 60 ns of the simulation time. The colours correspond to α-helix (pink), β-extended strand (orange), bend (blue), β bridge (purple), hydrogen-bonded turn (green), G-helix (yellow), and undetermined/random coil (grey), respectively.

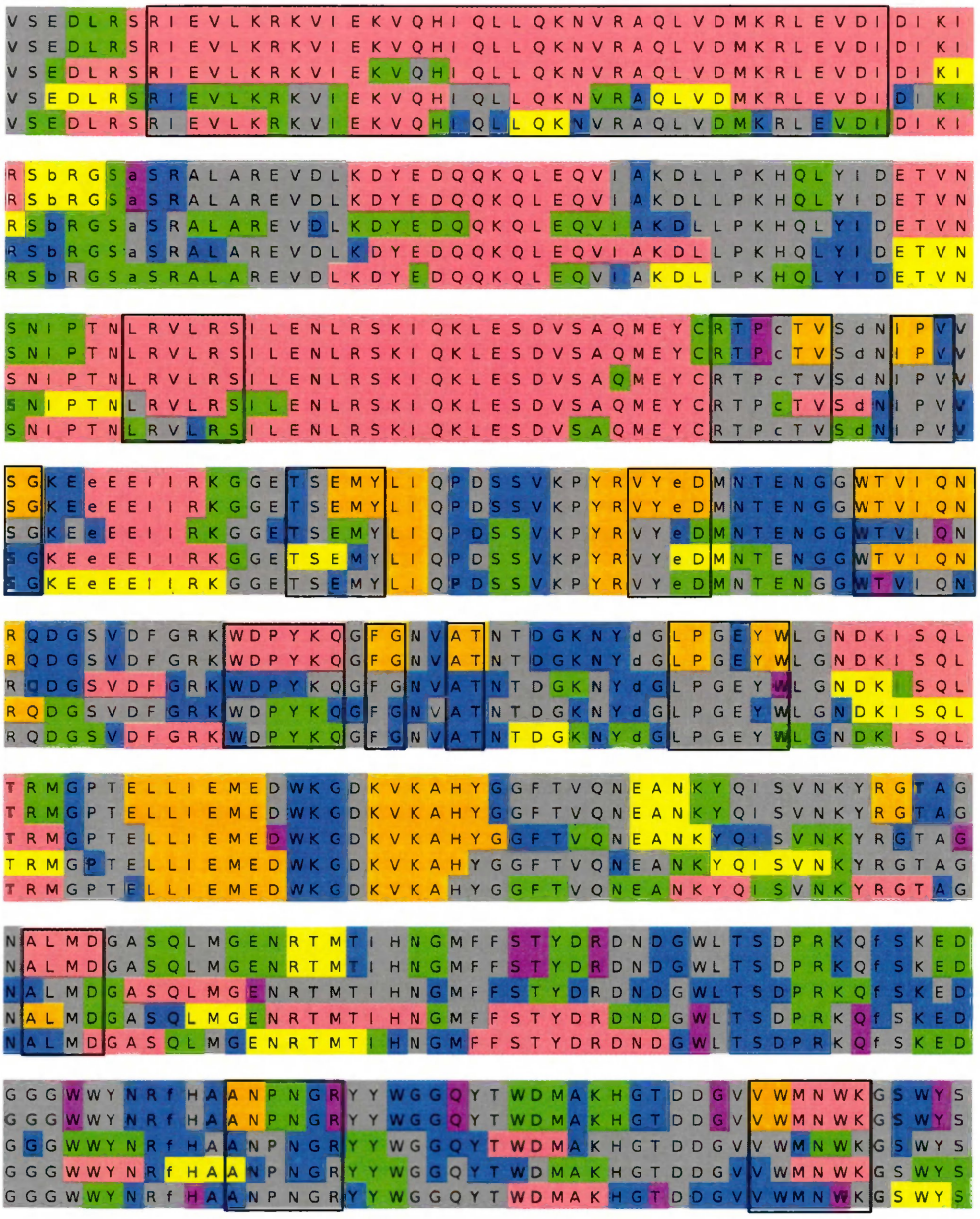

Figure 5.33: Secondary structure content per residue for D-domain at the surface of graphene (perpendicular position) every 20 ns period during 60 ns of the simulation time. The colours correspond to α-helix (pink), β-extended strand (orange), bend (blue), β bridge (purple), hydrogen-bonded turn (green), G-helix (yellow), and undetermined/random coil (grey), respectively.

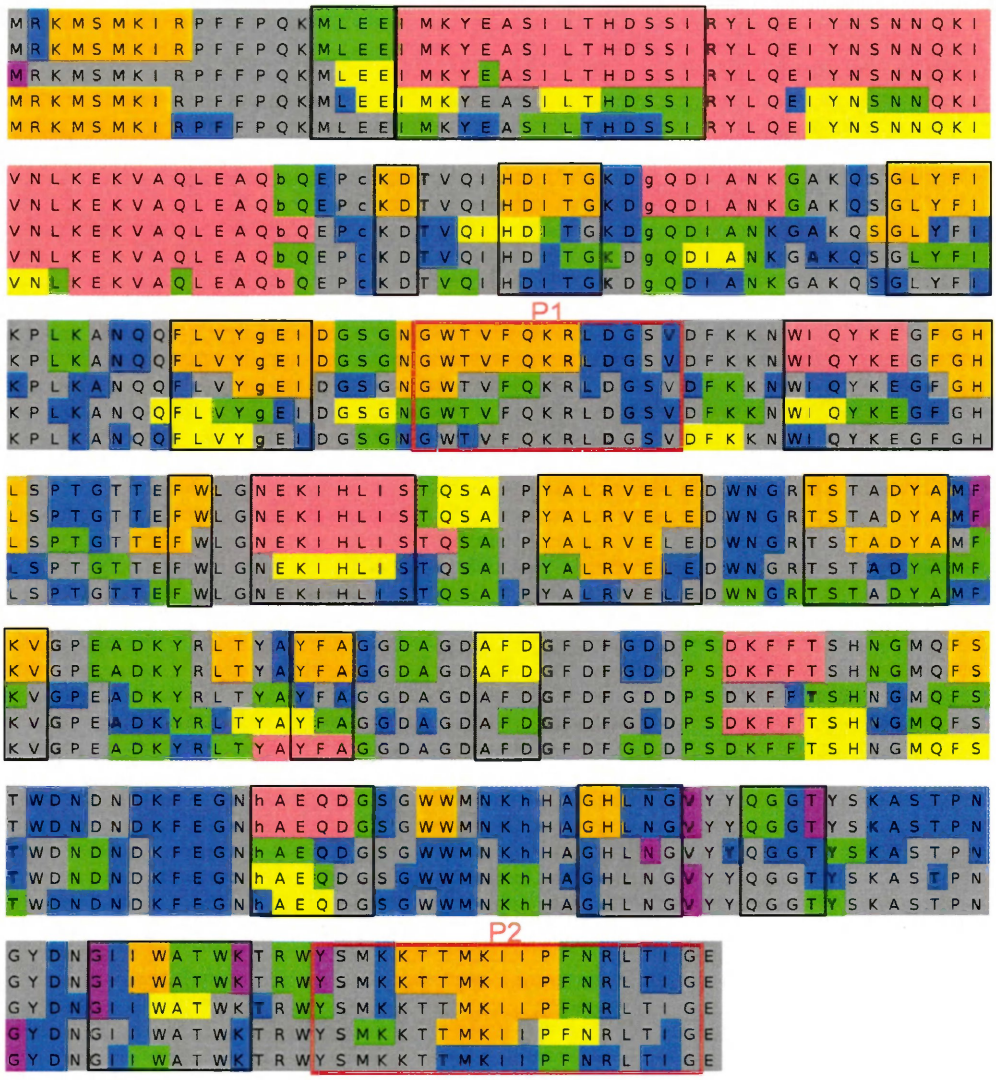

Figure 5.33: **Continued.** Secondary structure content per residue for D-domain at the surface of graphene (perpendicular position) every 20 ns period during 60 ns of the simulation time. The colours correspond to α-helix (pink), β-extended strand (orange), bend (blue), β bridge (purple), hydrogen-bonded turn (green), G-helix (yellow), and undetermined/random coil (grey), respectively.

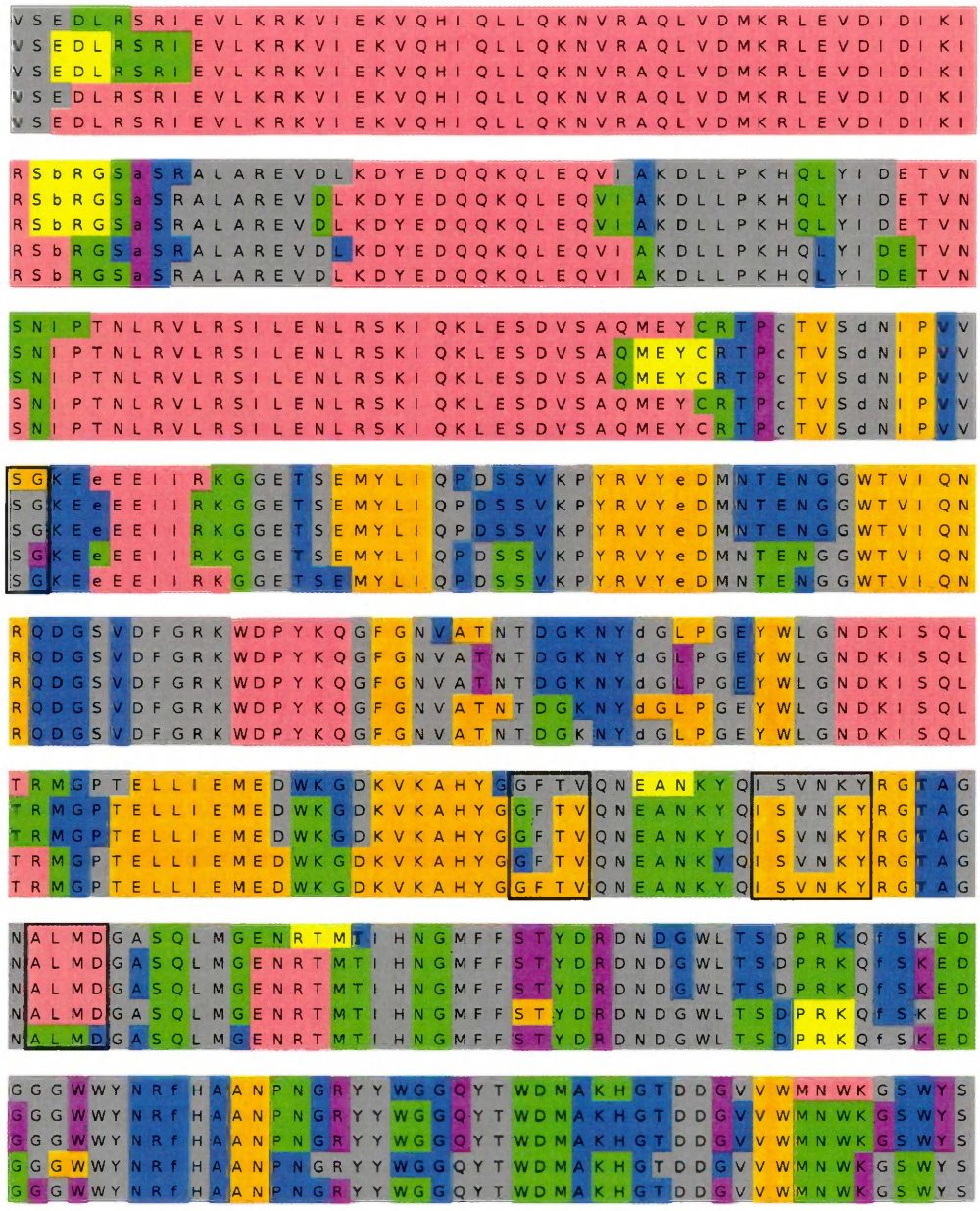

Figure 5.34: Secondary structure content per residue for D-domain in the unbound (native) state every 20 ns period during 60 ns of the simulation time. The colours correspond to α-helix (pink), β-extended strand (orange), bend (blue), β bridge (purple), hydrogen-bonded turn (green), G-helix (yellow), and undetermined/random coil (grey), respectively.

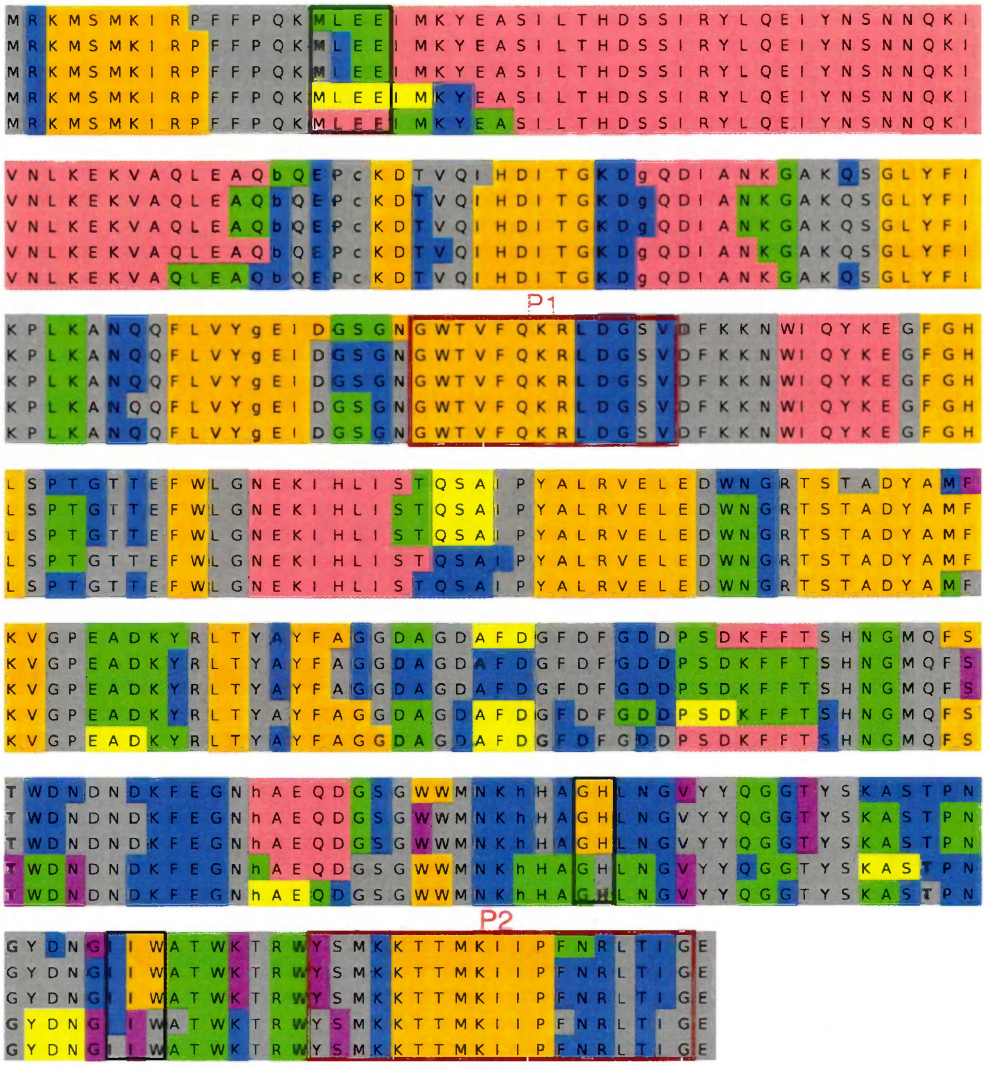

Figure 5.34: **Continued.** Secondary structure content per residue for D-domain in the unbound (native) state every 20 ns period during 60 ns of the simulation time. The colours correspond to α-helix (pink), β-extended strand (orange), bend (blue), β bridge (purple), hydrogen-bonded turn (green), G-helix (yellow), and undetermined/random coil (grey), respectively.

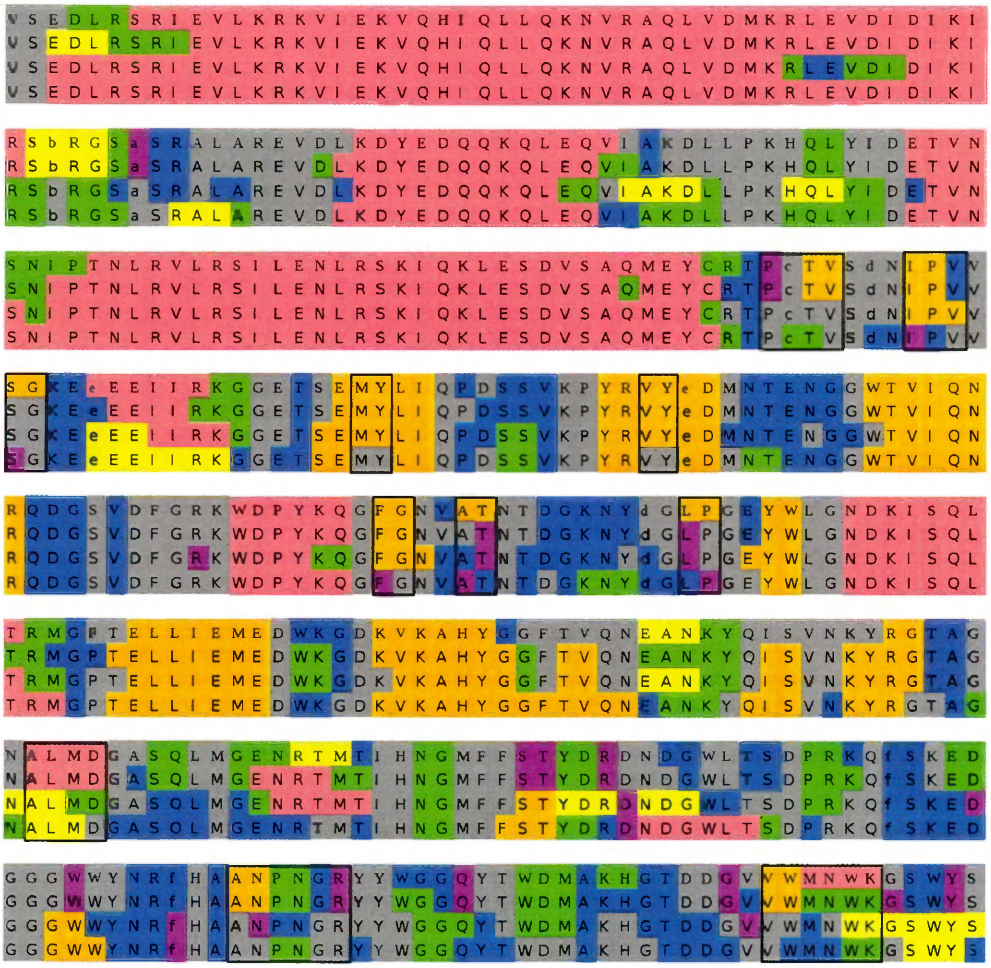

Figure 5.35: Secondary structure content per residue for D-domain at the PEG monolayer (perpendicular position) every 20 ns period during 60 ns of the simulation time. The colours correspond to α-helix (pink), β-extended strand (orange), bend (blue), β bridge (purple), hydrogen-bonded turn (green), G-helix (yellow), and undetermined/random coil (grey), respectively.

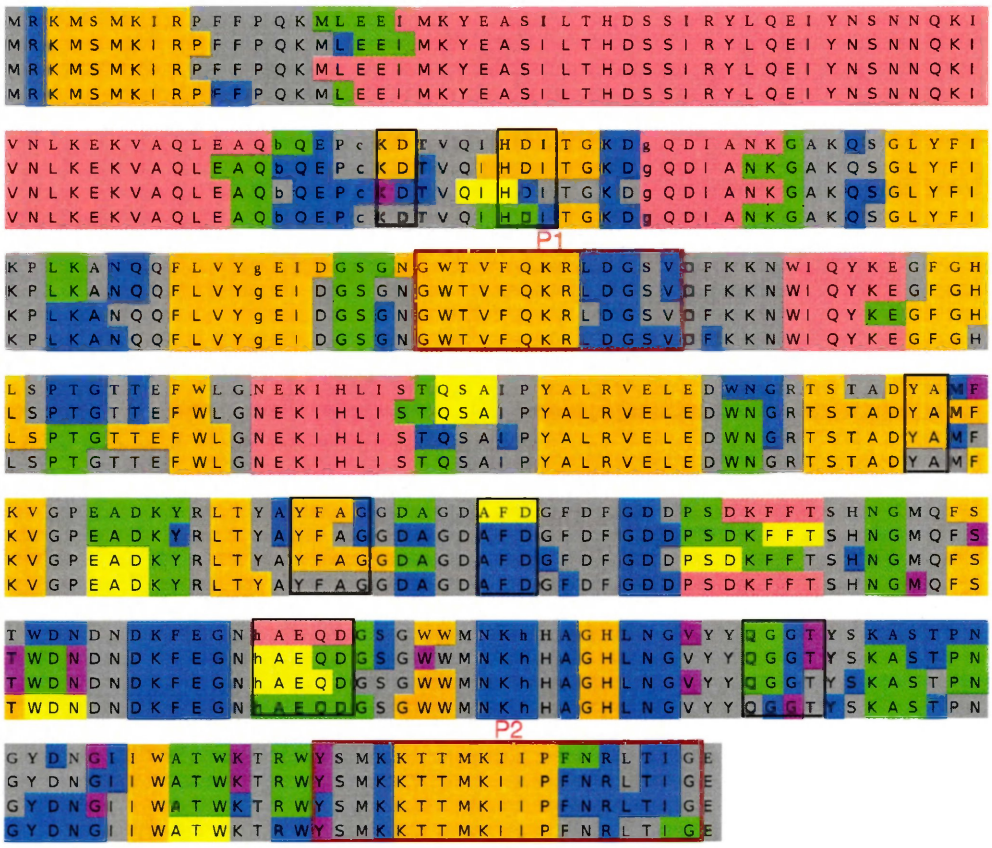

Figure 5.35: **Continued.** Secondary structure content per residue for D-domain at the PEG monolayer (perpendicular position) every 20 ns period during 60 ns of the simulation time. The colours correspond to α-helix (pink), β-extended strand (orange), bend (blue), β bridge (purple), hydrogen-bonded turn (green), G-helix (yellow), and undetermined/random coil (grey), respectively.

Chapter 6

Conclusions and future work

Although experimental studies on protein adsorption have been described in the literature, they are not able to provide details on biocompatibility molecular mechanisms, and explain how adverse reactions can be prevented. Therefore, the goal in research of materials for orthopaedic purposes has to be shifted from understanding the adsorption properties of unmodified materials to intelligent design of materials to mediate the adsorption process.

As it was discussed in the Chapter 1, biomaterials should not only be tolerant to the living tissue, but also enhance bone cell growth participating in healing processes. To perform the rational design of materials used for production of biomedical implant devices, the fibrinogen adhesion to the surface should be guided.

With increasing computer performance, however, this issue will certainly be possible to address. Chapters 3-5 now allow to address this issue by understanding molecular mechanisms that happen at the fibrinogen/graphene surface interface. The atomistic details of the interactions that determine plasma protein affinity modes on

surfaces with high hydrophobicity were studied. The results of this work propose that graphene is potentially pro-inflammatory surface, and cannot be used directly (without alterations) for biomedical purposes. The results also help in understanding the role of surface wettability and structure in controlling fibrinogen interactions with biomaterial as well as offer insight into the fundamental processes that occur when proteins contact an artificial surface. The developed methodology can be applied for other surfaces that potentially may be used as biomaterials in orthopaedic devices. It is also important to determine adhesion behaviour between proteins and surfaces because of proteins' ability to activate cells functionality.

The ideal biomaterial must stimulate very precise non-immunologic reactions to proteins and cells by using adhesive (for bone cells attachment and growth) and non-adhesive (for selective fibrinogen binding) regions. It is possible that a surface could be designed to adsorb the fibrinogen in a manner to prevent cryptic sites from being exposed. This can be achieved by using surface chemistry to control (guide) adsorbed fibrinogen to desired orientations.

Although the research is still in the early stages, it has a potential to sophisticate the quality of existing implants by understanding molecular mechanisms of protein-implant surface interactions in an aqueous environment. Future work will be focused on modulating immune response by modifying surface properties. Fibrinogen adsorption behaviour can be investigated as a function of surface chemistry (by covalently adding hydroxyl, carboxyl, amine, methyl and phosphate groups) of graphene-based nano materials using AMBER03 force field. The next step in this project will be to simulate graphene oxide surface interacting with fibrinogen fragment. Graphene properties may modulate the ability of tightly adsorbed fibrinogen fragment to inter-

act with complement cells. The graphene oxide hydrophilic properties could increase the long-term effectiveness of orthopaedic devices by interfering with the initial phase of implant rejection (fibrinogen adsorption).

The perfect material should affect normal immune cell function such that they promote healing and implant integration while sustaining specific implant function. The modulating of biomaterials on their effects on both acquired and innate immune responses as a component of biocompatibility assessment needs to be done. Alteration of material surface properties either passively via physico-chemical features or actively with molecules or matrices designed to systematically target cell behaviour will be performed. The aim is to increase mineralization of osteoblasts, prevent inflammation responses, reduce to possible minimum thickness of fibrous capsule and fibrinogen adsorption.

Bibliography

[1] G. M. Alberton, W. A. High, and B. F. Morrey. Dislocation after revision total hip arthroplasty: An analysis of risk factors and treatment options. *J. Bone Joint Surg. Am.*, 84-A:1788–1792, 2002.

[2] P. Cram, X. Lu, P. J. Kaboli, M. S. Vaughan-Sarrazin, X. Cai, B. R. Wolf, and Y. Li. Clinical characteristics and outcomes of medicare patients undergoing total hip arthroplasty, 1991-2008. *JAMA*, 305:1560–1567, 2011.

[3] M. Hukkanen, S. A. Corbett, J. Batten, Y. T. Konttinen, I. D. Mccarthy, J. Maclouf, S. Santavirta, S. P. F. Hughes, and J. M. Polak. Aseptic loosening of total hip replacement. *J. Bone Joint Surg. [Br]*, 79-B, 1997.

[4] Y. Abu-Amer, I. Darwech, and J. C. Clohisy. Aseptic loosening of total joint replacements: mechanisms underlying osteolysis and potential therapies. *Arthritis Res. Ther.*, 9, 2007.

[5] C. Drake, M. Ace, and G. E. Maale. Revision total hip arthroplasty. *AORN Journal*, 76:414–417, 419–427, 2002.

[6] R. G. Nelissen, E. R. Valstar, R.G. Pöll, E. H. Garling, and R. Brand. Factors

associated with excessive migration in bone impaction hip revision surgery: A radiostereometric analysis study. *J. Arthroplasty*, 17:826–833, 2002.

[7] N. N. Mahomed, J. A. Barrett, J. N. Katz, C. B. Phillips, E. Losina, R. A. Lew, E. Guadagnoli, W. H. Harris, R. Poss R, and J. A. Baron. Rates and outcomes of primary and revision total hip replacement in the united states medicare population. *J. Bone Joint Surg. Am.*, 85-A:27–32, 2003.

[8] J. N. Katz, J. Wright, E. A. Wright, and E. Losina. Failures of total hip replacement: a population-based perspective. *Orthop. J. Harv. Med. Sch.*, 9, 2004.

[9] R. Trahair. *All About Hip Replacement: A Patient's Guide.* ISBN 0-19-554112-X. Melbourne, Oxford, and New York: Oxford University Press, 1998.

[10] N. T. Ómalley, F. J. Fleming, D. D. Gunzler, S. P. Messing, and S. L. Kates. Factors independently associated with complications and length of stay after hip arthroplasty. analysis of the national surgical quality improvement program. *J. Arthroplasty*, 27:1832–1837, 2012.

[11] V. A. Blake, J. P. Allegrante, L. Robbins, C. A. Mancuso, M. G. Peterson ang J. M. Esdaileand S. A. Paget, and M. E. Charlson. Racial differences in social network experience and perceptions of benefit of arthritis treatments among new york city medicare beneficiaries with self-reported hip and knee pain. *Arthritis Rheum.*, 47:366–371, 2002.

[12] K. R. Pelletier. *CAM Therapies for Specific Conditions.* New York: Simon and Schuster, 2002.

[13] I. Silber. *A Patient's Guide to Knee and Hip Replacement: Everything You Need to Know.* New York: Simon & Schuster, 1999.

[14] L. Puri, R. L. Wixson, S. H. Stern, J. Kohli, R. W. Hendrix, and S. D. Stulberg. Use of helical computed tomography for the assessment of acetabular osteolysis after total hip arthroplasty. *J. Bone Joint Surg. Am.*, 84-A(4):609–614, 2002.

[15] J. N. Katz, E. Losina J. Barrett, C. B. Phillips, N. N. Mahomed, R. A. Lew, E. Guadagnoli, W. H. Harris, R. Possand, and J. A. Baron. Association between hospital and surgeon procedure volume and outcomes of total hip replacement in the united states medicare population. *J. Bone Joint Surg. Am.*, 83-A:1622–1629, 2001.

[16] M. Aynardi C.L. Jacovides R. Huang, S.M. Mortazavi, and J. Parvizi. Risk factors for early mortality following modern total hip arthroplasty. *J. Arthroplasty*, 28:517– 520, 2013.

[17] J. R. Berstock, A. D. Beswick, E. Lenguerrand, M. R. Whitehouse, and A. W. Blom. Mortality after total hip replacement surgery: A systematic review. *Bone Joint Res.*, 3:175–182, 2014.

[18] B. Bordini, S. Stea, M. De Clerico, S. Strazzari, A. Sasdelli, and A. Toni. Factors affecting aseptic loosening of 4750 total hip arthroplasties: multivariate survival analysis. *BMC Musculoskelet. Di.*, 8, 2007.

[19] A. H. Sott and J. W. Rosson. The influence of biomaterial on patterns of failure after cemented total hip replacement. *Int. Orthop.*, 26:287–290, 2002.

[20] M. Navarro, A. Michiardi, O. Castano, and J. A. Planell. Biomaterials in orthopaedics. *J. R. Soc. Interface*, 5:1137–1158, 2008.

[21] B. D. Ratner, A. S. Hoffman, F. J. Schoen, and J. E. Lemons. *Biomaterials Science, 2nd Edition An Introduction to Materials in Medicine.* ISBN-10: 0125824637. Elsevier Academic Press, 2004.

[22] D. J. Langton, S. S. Jameson, T. J. Joyce, N. J. Hallab, S. Natu, and A. V. F. Nargol. Early failure of metal-on-metal bearings in hip resurfacing and large-diameter total hip replacement a consequence of excess wear. *J. Bone Joint Surg. [Br]*, 92B:38–46, 2010.

[23] S.T. Donell, C. Darrah amd J. F. Nolan, J. Wimhurst, A. Toms, T. H. W. Barker, C. P. Case, and J. K. Tucker. Early failure of the ultima metal-on-metal total hip replacement in the presence of normal plain radiographs. *J. Bone Joint Surg. [Br]*, 92-B:1501–1508, 2010.

[24] D. J. Langton, S. S. Jameson, T. J. Joyce, J. N. Gandhi, R. Sidaginamale, P. Mereddy, and J. Lordand A. V. F. Nargol. Accelerating failure rate of the asr total hip replacement. *J. Bone Joint Surg. [Br]*, 93B:1011–1016, 2011.

[25] G. Manivasagam, D. Dhinasekaran, and A. Rajamanickam. Biomedical implants: Corrosion and its prevention - a review. *Recent Patents on Corrosion Science*, 2:40–54, 2010.

[26] M. I. Sabir, X. Xu, and L. Li. A review on biodegradable polymeric materials for bone tissueengineering applications. *J. Mater. Sci.*, 44:5713–5724, 2009.

[27] E. Kontou and G. Spathis. Viscoplastic response and creep failure time prediction of polymers based on the transient network model. *Mech. Time-Depend. Mater.*, 18:373–386, 2014.

[28] J. Zhao, L. X. Lu, and T. Rabczuk. The tensile and shear failure behavior dependence on chain length and temperature in amorphous polymers. *Comp. Mater. Sci.*, 96:567–572, 2015.

[29] A. Faraj. Patterns of failure of ceramic liner in total hip replacement: report of two cases. *Eur. J. Orthop. Surg. Traumatol.*, 19:43–46, 2009.

[30] R. Morrell, R. Danzer, I. Milosev, and R. Trebse. An assessment of in vivo failures of alumina ceramic total hip joint replacements. *J. Eur. Ceram. Soc.*, 32:3073–3084, 2012.

[31] J. M. Brandt, T. C. Gascoyne, L. E. Guenther, A. Allen, D. R. Hedden, T. R. Turgeon, and E. R. Bohm. Clinical failure analysis of contemporary ceramic-on-ceramic total hip replacements. *Proceedings of the Institution of mechanical engineers part H-Jornal of engineering in medicine*, 227:833–846, 2013.

[32] D. Fabio, M. Molina, G. Riva, G. Zatti, and P. Cherubino. Failure of dual radius hydroxyapatite-coated acetabular cups. *J. Orthop. Surg. Res.*, 3:35, 2008.

[33] N. A. Rakngarm, T. Loanapakul, Y. Otsuka, and Y. Mutoh. Effect of apatite precipitation on failure behavior of hydroxyapatite coating layer on titanium substrate. *J. Biomater. Appl.*, 506:61–65, 2012.

[34] B. Stevens, Y. Yang, A. Mohandas, B. Stucker, and K. T. Nguyen. A review

of materials, fabrication methods, and strategies used to enhance bone regeneration in engineered bone tissues. *J. Biomed. Mater. Res. B Appl. Biomater.*, 85:573–582, 2008.

[35] D. F. Williams. On the mechanisms of biocompatibility. *Biomaterials*, 29:2941–2953, 2008.

[36] P. Vadgama. Surface biocompatibility. *Annu. Rep. Prog. Chem., Sect. C: Phys. Chem.*, 101:14–52, 2005.

[37] K. Udipi, A. Hezi-Yamit, M. F. Chen, P. W. Cheng, J. Wong, C. Sullivan, and J. N. Wilcox. Importance of polymer hydrophilicity/hydrophobicity on biocompatibility of DES coatings. *Am. J. Cardiol.*, 100:162L, 2007.

[38] S. Bonakdar, F. Orang, M. Rafiena, and R. Imani. Comparison of the effect of hydrophilicity on biocompatibility and platelet adhesion of two different kinds of biomaterials. *IJPS*, 4:37–44, 2008.

[39] G. Tihan, S. Minkovska, M. Giurginca, T. Tite, H. Iovu, and I. Demetrescu. Hydrophilic/hydrophobic balance in relation with structure and biocompatibility of ternary biofilms PVA-HAP-collagen gel. *Mol. Cryst. Liq. Cryst. Sci. Technol.*, 486:1217–1224, 2008.

[40] M. C. Jones, S. A. Jones, Y. Riffo-Vasquez, D. Spina, E. Hoffman, A. Morgan, A. Patel, S. Page, B. Forbes, and L. A. Dailey. Quantitative assessment of nanoparticle surface hydrophobicity and its influence on pulmonary biocompatibility. *J. Controlled Release*, 183:94–104, 2014.

[41] K. Murphy. *Immunobiology, 8th edition.* 978-0-8153-4243-4. Garland Science, Taylor & Francis Group, LLC, 2012.

[42] S. Franz, S. Rammelt, D. Scharnweber, and J. C. Simon. Immune responses to implants e a review of the implications for the design of immunomodulatory biomaterials. *Biomaterials*, 32:6692–6709, 2011.

[43] M. B. Gorbet and M. V. Sefton. Biomaterial-associated thrombosis: roles of coagulation factors, complement, platelets and leukocytes. *Biomaterials*, 25:5681–5703, 2004.

[44] J. M. Anderson, A. Rodriguez, and D. T. Chang. Foreign body reaction to biomaterials. *Semin. Immunol.*, 20:86–100, 2008.

[45] J. K. Ryu and D. D. Akassoglou. Fibrinogen signal transduction in the nervous system. *JTH*, 7:151–154, 2009.

[46] M. S. Diamond and T. A. Springer. A subpopulation of Mac-1 (CD11b/CD18) molecules mediates neutrophil adhesion to ICAM-1 and fibrinogen. *J. Cell Biol.*, 120:545–556, 1993.

[47] W.-J. Hu, J. W. Eaton, T. P. Ugarova, and L. Tang. Molecular basis of biomaterial-mediated foreign body reactions. *Blood*, 98:1231–1238, 2001.

[48] T. P. Ugarova, A. Solovjov, and L. Zhang. Identification of a novel recognition equence for integrin $\alpha_M\beta_2$ within the γ-chain of fibrinogen. *J.Biol. Chem.*, 273:22519–22527, 1998.

[49] L. Tang, T. P. Ugarova, E. F. Plow, and J. W. Eaton. Molecular determinants of acute inflammatory responses to biomaterials. *J. Clin. Invest.*, 97:1329–1334, 1996.

[50] C. B. Forsyth, D. A. Solovjov, T. P. Ugarova, and E. F. Plow. Integrin $\alpha_{\mathrm{m}}\beta_2$-mediated cell migration to fibrinogen and its recognition peptides. *J. Exp. Med.*, 2001.

[51] V. P. Yakubenko, D. A. Solovjov, L. Zhang, V. C. Yee, E. F. Plow, and T. P. Ugarova. Identification of the binding site for fibrinogen recognition peptide γ383-395 within the α_{MI}-domain of integrin $\alpha_M\beta_2$. *J. Biol. Chem.*, 276:13995–14003, 2001.

[52] V. K. Lishko, B. Kudryk, V. P. Yakubenko, V. C. Yee, and T. P. Ugarova. Regulated unmasking of the cryptic binding site for integrin $\alpha_{\mathrm{M}}/\beta_2$ in the γ c-domain of fibrinogen. *Biochemistry*, 41:12942–12951, 2002.

[53] T. P. Ugarova, V. K. Lishko, N. P. Podolnikova, N. Okumura, S. M. Merkulov, V. P. Yakubenko, V. C. Yee, S. T. Lord, and T. A. Haas. Sequence γ377-395 (P2), but not γ190-202 (P1), is the binding site for the α_{MI}-domain of integrin $\alpha_M\beta_2$ in the γc-domain of fibrinogen. *Biochemistry*, 42:9365–9373, 2003.

[54] V. K. Lishko, N. P. Podolnikova, V. P. Yakubenko, S. Yakovlev, L. Medved, S. P. Yadav, and T. P. Ugarova. Multiple binding sites in fibrinogen for integrin $\alpha_M\beta_2$ (Mac-1). *J. Biol. Chem.*, 279:44897–44906, 2004.

[55] M. Fischer, C. Sperling, P. Tengvall, and C. Werner. The ability of surface

characteristics of materials to trigger leukocyte tissue factor expression. *Biomaterials*, 31:2498–2507, 2010.

[56] M. Frank and L. Fries. The role of complement in inflammation and phagocytosis. *Immunol. Today*, 12:322–326, 1991.

[57] C. J. Wilson, R. E. Clegg, D. I. Leavesley, and M. J. Pearcy. Mediation of biomaterial-cell interactions by adsorbed proteins: a review. *Tissue Eng.*, 11, 2005.

[58] D. T. Luttikhuizen, M. C. Harmsen, and M. J. A. Van Luyn. Cellular and molecular dynamics in the foreign body reaction. *Tissue Eng.*, 12:1955–1970, 2006.

[59] Z. Xia and J.T. Triffitt. A review on macrophage responses to biomaterials. *Biomed. Mater.*, 1:R1–R9, 2006.

[60] D. Ricklin, G. Hajishengallis, K. Yang, and J. D. Lambris. Complement: a key system for immune surveillance and homeostasis. *Nat. Immunol.*, 11:785797, 2010.

[61] A. E. Engberg, J. P. Rosengren-Holmberg, H. Chen, B. Nilsson, J.D. Lambris, I. A. Nicholls, and K. N. Ekdahl. Blood protein-polymer adsorption: implications for understanding complement-mediated hemoincompatibility. *J. Biomed. Mater. Res. A*, 97:74–84, 2011.

[62] K. N. Ekdahl, J. D. Lambris, H. Elwing, D. Ricklin, P. H. Nilsson, Y. Teramura, and I. A. Nicholllsand B. Nilsson. Innate immunity activation on biomaterial

surfaces: a mechanistic model and coping strategies. *Adv. Drug Deliv. Rev.*, 63:1042–1050, 2011.

[63] D. B. Kuhns, D. A. Priel, and J. I. Gallin. Induction of human monocyte interleukin (IL)-8 by fibrinogen through the toll-like receptor pathway. *Inflammation*, 30:178–188, 2007.

[64] T. H. Rogers and J. E. Babensee. Altered adherent leukocyte profile on biomaterials in toll-like receptor 4 deficient mice. *Biomaterials*, 31:564–601, 2010.

[65] V. Barrera, O. A. Skorokhod, D. Baci, G. Gremo, P. Arese, and E. Schwarzer. Host fibrinogen stably bound to hemozoin rapidly activates monocytes via TLR-4 and CD11b/CD18-integrin: a new paradigm of hemozoin action. *Blood*, 117:5674–5682, 2011.

[66] C. Jennewein, N. Tran, P. Paulus, P. Ellinghaus, J. Andreas Eble, and K. Zacharowski. Novel aspects of fibrin(ogen) fragments during inflammation. *Mol. Med.*, 17:568–573, 2011.

[67] E. Al-ofi, S. B. Coffelt, and D. O. Anumba. Fibrinogen, an endogenous ligand of toll-like receptor 4, activates monocytes in pre-eclamptic patients. *J. Reprod. Immunol.*, 103, 2014.

[68] R. O. Hynes. Integrin: bidirectional, allosteric signaling machines. *Cell*, 110:673–687, 2002.

[69] R. Li and M. A. Arnaout. Functional analusis of the β_2 integrins. *Methods Mol. Biol.*, 129:105–124, 1999.

[70] M. H. Faridi, M. M. Altintas, C. Gomez, J. C. Duque, R. I. Vazquez-Padron, and V. Gupta. Small molecule agonists of integrin CD11b/CD18 do not induce global conformational changes and are significantly better than activating antibodies in reducing vascular injury. *Biochim. Biophys. ACTA*, 1830:3696–3710, 2013.

[71] S. D. Wright, J. I. Weitz, A. J. Huang, S. M. Levin, S. C. Silverstein, and J. D. Loike. Complement receptor type three (CD11b/CD18) of human polymorphonuclear leukocytes recognizes fibrinogen. *Proc. Natl. Acad. Sci. USA*, 85:7734–7738, 1988.

[72] D. C. Altieri, J. Plescia, and E. F. Plow. The structural motif glycine 190-valine 202 of the fibrinogen γ chain interacts with CD11b/CD18 integrin and promotes leukocyte adhesion. *J. Biol. Chem.*, 268:1847–1853, 1993.

[73] D. H. Farrell. Pathophysiologic roles of the fibrinogen γ chain. *Curr. opinion in hematology*, 11:151–155, 2004.

[74] M. J. Flick, X. Du, D. P. Witte, M. Jirousková, D. A. Soloviev, S. J. Busuttil, E. F. Plow, and J. L. Degen. Leukocyte engagement of fibrin(ogen) via the integrin receptor $\alpha_M\beta_2$ / mac-1 is critical for host inflammatory response in vivo. *J. Clin. Invest.*, 113:1596–1606, 2004.

[75] S. Yakovlev, L. Zhang, T. Ugarova, and L. Medved. Interaction of fibrin(ogen) with leukocyte receptor $\alpha_M\beta_2$ (Mac-1): Further characterization and identification of a novel binding region within the central domain of the fibrinogen γ-module. *Biochemistry*, 44:617–626, 2005.

[76] N. C. Kaneider, B. Mosheimer, A. Gunther, C. Feistritzer, and C. J. Wiedermann. Enhancement of fibrinogen-triggered pro-coagulant activation of monocytes in vitro by matrix metalloproteinase-9. *J.Thromb.*, 8, 2010.

[77] Z. J. Deng, M. Liang, M. Monteiro, I. Toth, and R. F. Minchin. Nanoparticle-induced unfolding of fibrinogen promotes mac-1 receptor activation and inflammation. *Nat. Nanotech. Lett.*, 6:39–44, 2011.

[78] D. G. Castner and B. D. Ratner. Biomedical surface science: foundations to frontiers. *Surf. Sci.*, 500:2860, 2002.

[79] X. Liu, S. J. Valentine, M. D. Plasencia, S. Trimpin, S. Naylor, and D. E. Clemmer. Mapping the human plasma proteome by scx-lc-ims-ms. *J. Am. Soc. Mass Spectrom.*, 18:1249–1264, 2007.

[80] D. Davalos and K. Akassoglou. Fibrinogen as a key regulator of inflammation in disease. *Semin. Immunopathol.*, 34:43–62, 2011.

[81] M. Rabe, D. Verdes, and S. Seeger. Understanding protein adsorption phenomena at solid surfaces. *Adv. Colloid. Interface Sci.*, 162:87–106, 2011.

[82] Y. Yuan and T. R. Lee. Contact angle and wetting properties. *Springer Series in Surf. Sci.*, 51, 2013.

[83] J. R. Huntsberger. Surface chemistry and adhesion-review of some fundamentals. *J. Adhes*, 7:289–299, 1976.

[84] L.-C. Xu and C. A. Siedlecki. Atomic force microscopy studies of the initial interactions between fibrinogen and surfaces. *Langmuir*, 25:3675–3681, 2009.

[85] G. Janvier, C. Baquey, C. Roth, N. Benillan, S. Bélisle, and J.F. Hardy. Extracorporeal circulation, hemocompatibility, and biomaterials. *Ann. Thorac. Surg.*, 62:1926–1934, 1996.

[86] P. Cacciafesta, A. D. L. Humphris, K. D. Jandt, and M. J. Miles. Human plasma fibrinogen adsorption on ultraflat titanium oxide surfaces studied with atomic force microscopy. *Langmuir*, 16:8167–8175, 2000.

[87] M. Ramazanoglu and Y. Oshida. *Osseointegration and Bioscience of Implant Surfaces - Current Concepts at Bone-Implant Interface, Implant Dentistry - A Rapidly Evolving Practice.* Number 978-953-307-658-4. 2011. http://www.intechopen.com/books/implant-dentistry-a-rapidly-evolving-practice/osseointegration-andbioscience- of-implant-surfaces-current-concepts-at-bone-implant-interface.

[88] M. I. Kay, R. A. Young, and A. S. Posner. Crystal structure of hydroxyapatite. *Nature*, 204:1050–1052, 1964.

[89] C. Yong Tay, W. Fang, M. I. Setyawati, S. L. Chia, K. S. Tan, C. H. L. Hong, and D. T. Leong. Nano-hydroxyapatite and nano-titanium dioxide exhibit different subcellular distribution and apoptotic profile in human oral epithelium. *ACS Appl. Mater. Interfaces*, 6:6248–6256, 2014.

[90] P. Thevenot, W. Hu, and L. Tang. Surface chemistry influences implant biocompatibility. *Curr. Topics in Med. Chem.*, 8:270–280, 2008.

[91] M. W. Mosesson, K. R. Siebenlist, and D. A. Meh. The structure and biological features of fibrinogen and fibrin. *Ann. N. Y. Acad. Sci.*, 936:11–30, 2001.

[92] M. W. Mosesson. Fibrinogen and fibrin structure and functions. *J. Throm. Haemost.*, 3:1894–1904, 2005.

[93] P. Roach, D. Farrar, and C. C. Perry. Interpretation of protein adsorption: Surface-induced conformational changes. *J. Am. Chem. Soc.*, 127:8168–8173, 2005.

[94] S. Tunc, M. F. Maitz, G. Steiner, L. Vázquez, M. T. Pham, and R. Salzer. In situ conformational analysis of fibrinogen adsorbed on si surfaces. *Colloid. Surface B: Biointerfaces*, 42:219–225, 2005.

[95] J. Wang, X. Chen, M. L. Clarke, and Z. Chen. Vibrational spectroscopic studies on fibrinogen adsorption at polystyrene/protein solution interfaces: Hydrophobic side chain and secondary structure changes. *J. Phys. Chem. B*, 110:5017–5024, 2006.

[96] C. Yongli, Z. Xiufang, G. Yandao, Z. Nanming, Z. Tingying, and S. Xinqi. Conformational changes of fibrinogen adsorption onto hydroxyapatite and titanium oxide nanoparticles. *J. Colloid. Interface Sci.*, 214:38–45, 1999.

[97] I. V. D. Keere, R. Willaert, A. Hubin, and J. Vereecken. Interaction of human plasma fibrinogen with commercially pure titanium as studied with atomic force microscopy and x-ray photoelectron spectroscopy. *Langmuir*, 24:1844–1852, 2008.

[98] M. Yaseen, X. Zhao, A. Freund, A. M. Seifalian, and J. R. Lu. Surface structural conformations of fibrinogen polypeptides for improved biocompatibility. *Biomaterials*, 31:3781–3792, 2010.

[99] T. C. Ta, M. T. Sykes, and M. T. McDermott. Real-time observation of plasma protein film formation on well-defined surfaces with scanning force microscopy. *Langmuir*, 14:2435–2443, 1998.

[100] B. Drake, C. B. Prater, A. L. Weisenhorn, S. A. Gould, T. R. Albrecht, C. F. Quate, D. S. Cannell, H. G. Hansma, and P. K. Hansma. Imaging crystals, polymers, and processes in water with the atomic force microscope. *Science*, 243:1586–1589, 1989.

[101] S. Y. Park, J. Park, S. H. Sim, M. G. Sung, K. S. Kim, B. H. Hong, and S. Hong. Enhanced differentiation of human neural stem cells into neurons on graphene. *Adv. Mater.*, 23:H263–H267, 2011.

[102] J. Woodley. Bioadhesion: New possibilities for drug administration? *Clin. Pharmacokinet.*, 40:77–84, 2001.

[103] L. R. Rodrigues. Inhibition of bacterial adhesion on medical devices. *Adv. Exp. Med. Biol.*, 715:351–367, 2011.

[104] F. Nederberg, J. Watanabe, K. Ishihara, J. Hilborn, and T. Bowden. Biocompatible and biodegradable phosphorylcholine ionomers with reduced protein adsorption and cell adhesion. *J. Biomater. Sci., Polym. Ed.*, 17:605–614, 2006.

[105] K. Anselme. Osteoblasts adhesion on biomaterials. *Biomaterials*, 21:667–681, 2000.

[106] M. Dettin, M.T. Conconi, R. Gambaretto, A. Bagno, C. Di Bello, A. M. Menti,

C. Grandi, and P. P. Parnigotto. Effect of synthetic peptides on osteoblast adhesion. *Biomaterials*, 26:4507–4515, 2005.

[107] N. V. Shah and R. Meislin. Current state and use of biological adhesives in orthopedic surgery. *Orthopedics*, 36:945–956, 2013.

[108] A. F. Mavrogenis, R. Dimitriou, J. Parvizi, and G. C. Babis. Biology of implant osseointegration. *J. Musculoskelet. Neuronal Interact.*, 9:61–71, 2009.

[109] D. A. Puleo and A. Nanci. Understanding and controlling the bone-implant interface. *Biomaterials*, 20:2311–2321, 1999.

[110] M. J. Allen, V. C. Tung, and R. B. Kaner. Honeycomb carbon: A review of graphene. *Chem. Rev.*, 110:132–145, 2010.

[111] T. K. Das and S. Prusty. Recent advances in applications of graphene. *Int. J. Chem. Sciencis and Appl.*, 4:39–55, 2013.

[112] X. Hu and Q. Zhou. Health and ecosystem risks of graphene. *Chem. Rev.*, 113:3815–3835, 2013.

[113] V. C. Sanchez, A. Jachak, R. H. Hurt, and A. B. Kane. Biological interactions of graphene-family nanomaterials: an interdisciplinary review. *Chem. Res. Toxicol.*, 25:15–34, 2012.

[114] H. Ying Mao, S. Laurent, W. Chen, O. Akhavan, M. Imani, A. A. Ashkarran, and M. Mahmoudi. Graphene: Promises, facts, opportunities, and challenges in nanomedicine. *Chem. Rev.*, 113:3407–3424, 2013.

[115] C. N. R. Rao, A. K. Sood, K. S. Subrahmanyam, and A. Govindaraj. Graphene: The new two-dimensional nanomaterial. *Angew. Chem., Int. Ed.*, 48:77527777, 2009.

[116] Z. Chen, L. Dong, D. Yang, and H. Lu. Superhydrophobic graphene-based materials: surface construction and functional applications. *Adv. Mater.*, 25:5352–5359, 2013.

[117] Q. X. Pei, Y. W. Zhang, and V. B. Shenoy. Mechanical properties of methyl functionalized graphene: a molecular dynamics study. *Nanotech.*, 21:115709, 2010.

[118] Y. Hu, J. Shen, N. Li, M. Shi, H. Ma, B. Yan, W. Wang, W. Huang, and M. Ye. Amino-functionalization of graphene sheets and the fabrication of their nanocomposites. *Polym. Composit.*, 31:1987–1994, 2010.

[119] J. Liu, J. Tanga, and J. J. Gooding. Strategies for chemical modification of graphene and applications of chemically modified graphene. *J. Mater. Chem.*, 22:12435–12452, 2012.

[120] J. B. Goods, S. A. Sydlik, J. J. Walish, and T. M. Swager. Phosphate functionalized graphene with tunable mechanical properties. *Adv. Mater.*, 26:718–723, 2014.

[121] J. Kim, L. J. Cote, and J. Huang. Two dimensional soft material: New faces of graphene oxide. *Acc. Chem. Res.*, 45:13561364, 2012.

[122] S. Liu, T. H. Zeng, M. Hofmann, E. Burcombe, J. Wei, R. Jiang, J. Kong, and

Y. Chen. Antibacterial activity of graphite, graphite oxide, graphene oxide, and reduced graphene oxide: Membrane and oxidative stress. *ACS Nano*, 5:6971–6980, 2011.

[123] J. S. Czarnecki, K. Lafdi, and P. A. Tsonis. A novel approach to control growth, orientation, and shape of human osteoblasts. *Tissue Eng. Part A*, 14:255–265, 2008.

[124] T. R. Nayak, H. Andersen, V. S. Makam, C. Khaw, S. Bae, X. Xu, P.-L. R. Ee, J.-H. Ahn, B. H. Hong, G. Pastorin, and B. Ozyilmaz. Graphene for controlled and accelerated osteogenic differentiation of human mesenchymal stem cells. *ACS Nano*, 5:4670–4678, 2011.

[125] D. Y. Lee, Z. Khatun, J. H. Lee, Y. Lee, and I. In. Blood compatible graphene/heparin conjugate through noncovalent chemistry. *Biomacromolecules*, 12:336–341, 2011.

[126] T. Utesch, G. Daminelli, and M. A. Mroginski. Molecular dynamics simulations of the adsorption of bone morphogenetic protein-2 on surfaces with medical relevance. *Langmuir*, 27:13144–13153, 2011.

[127] S. Ryu and B.-S. Kim. Culture of neutral cells and stem cells on graphene. *Tissue Eng. and Reg. Med.*, 10:39–46, 2013.

[128] A. Bianco. Graphene: Safe or toxic? the two faces of the medal. *Nanomaterials*, 52:4986–4997, 2013.

[129] C. I. Branden and J. Tooze. *Introduction to Protein Structure.* Number 0-8153-2305-O. Garland Publishing, New York, 1999.

[130] G. E. Schulz and R. H. Schirmer. *Principles of protein structure.* ISBN 3-540-90386-0. Springer-Verlag, Berlin, Heidelberg, New York, 1979.

[131] C. Fuss, J. C. Palmaz, and E. A. Sprague. Fibrinogen: structure, function, and surface interactions. *J. Vasc. Interv. Radiol.*, 12:677–682, 2001.

[132] S. T. Lord. Molecular mechanisms affecting fibrin structure and stability. *Arterioscler. Thromb. Vasc. Biol.*, 31:494–499, 2011.

[133] J. M. Kollman, L. Pandi, M. R. Sawaya, M. Riley, and R. F. Doolittle. Crystal structure of human fibrinogen. *Biochemistry*, 48:3877–3886, 2009.

[134] I. S. Yermolenko, V. K. Lishko, T. P. Ugarova, and S. N. Magonov. High-resolution visualization of fibrinogen molecules and fibrin fibers with atomic force microscopy. *Biomacromolecules*, 12:370–379, 2011.

[135] Z. Bai, M. J. Filiaggi, and J. R. Dahn. Fibrinogen adsorption onto 316l stainless steel, nitinol and titanium. *Surf. Sci.*, 603:839–846, 2009.

[136] W. Kohn. Nobel lecture: Electronic structure of matterwave functions and density functionals. *Rev. Mod. Phys.*, 71:1253–1266, 1999.

[137] R. M. Dreizler and E. Engel. *Density Functional Theory : An Advanced Course.* Number ISBN 9783642140891 in Theoretical and Mathematical Physics. Berlin: Springer, 2011.

[138] R. M. Martin. *Electronic Structure: Basic Theory and Practical Methods.* Cambridge University Press, 2004.

[139] S. Cottenier. *Density functional theory and family of (L)ARW-methods: a step-by-step introduction.* ISBN 978-90-807215-1-7. 2013.

[140] J. Hafner. Atomic-scale computational materials. *Acta Mater.*, 48:71–92, 2000.

[141] S. A. Adcock and J. A. McCammon. Molecular dynamics: Survey of methods for simulating the activity of proteins. *Chem. Rev.*, 106:1589–1615, 2006.

[142] M. Griebel, S. Knapek, and G. Zumbusch. *Numerical Simulation in molecular dynamics.* Number 1611-0994. Springer, 2007.

[143] H. A. Scheraga, M. Khalili, and A. Liwo. Protein-folding dynamics: Overview of molecular simulation techniques. *Annu. Rev. Phys. Chem.*, 58:57–83, 2007.

[144] H. C. Andersen. Molecular-dynamics simulations at constant pressure and-or temperature. *J. Phys. Chem*, 95:3358–3363, 1991.

[145] P. L. Freddolino, C. B. Harrison, Y. Liu, and K. Schulten. Challenges in protein folding simulations: Timescale, representation, and analysis. *Nat Phys.*, 6:751–758, 2010.

[146] J. L. Klepeis, K. Lindorff-Larsen, R. O. Dror, and D. E. Shaw. Long-timescale molecular dynamics simulations of protein structure and function. *Curr. Opin. Struct. Biol.*, 19:120–127, 2009.

[147] T. Hansson, C. Oostenbrink, and W. F. van Gunsteren. Molecular dynamics simulations. *Curr. Opin. Struct. Biol.*, 12:190–196, 2002.

[148] M. Karplus and J. A. McCammon. Molecular dynamics simulations of biomolecules. *Nat. Struct. Biol.*, 9:646–652, 2002.

[149] M. A. González. Force fields and molecular dynamics simulations. *Collection SFN*, 12:169–200, 2011.

[150] W. D. Cornell, P. Cieplak, C. I. Bayly, I. R. Gould, K. M. Merz, D. M. Ferguson, D. C. Spellmeyer, T. Fox, J. W. Caldwell, and P. A. Kollman. A second generation force field for the simulation of proteins, nucleic scids, and organic molecules. *J. Am. Chem. Soc.*, 117:5179–5197, 1995.

[151] U. Zimmerli, M. Parrinello, and P. Koumoutsakos. Dispersion corrections to density functionals for water aromatic interactions. *J. Chem. Phys.*, 120, 2004.

[152] H. Heinz, R. A. Vaia, B. L. Farmer, and R. R. Naik. Accurate simulation of surfaces and interfaces of face-centered cubic metals using 12-6 and 9-6 Lennard-Jones potentials. *J. Chem. Phys. C*, 112:1728117290, 2008.

[153] V. A. Parsegian. *Van der Waals Forces: A Handbook for Biologists, Chemists, Engineers, and Physicists.* Number 978-0-521-83906-8. Cambridge University Press, 2006.

[154] C. Sagui and T. A. Darden. Molecular dynamics simulations of biomolecules: Long-range electrostatic effects. *Annu. Rev. Biophys. Biomol. Struct.*, 28:155–179, 1999.

[155] M. J. Harvey and G. De Fabritiis. An implementation of the smooth Particle-

Mesh Ewald method on GPU hardware. *J. Chem. Theory Comput.*, 5:2371–2377, 2009.

[156] P. P. Ewald. Die berechnung optischer und elektrostatischer gitterpotentiale. *ADP*, 369:253–287, 1921.

[157] T. Darden, D. York, and L. Pedersen. Particle Mesh Ewald: An N log(N) method for Ewald sums in large systems. *J. Chem. Phys.*, 98:1008910092, 1993.

[158] S. W. de Leeuw, J. W. Perram, and E. R. Smith. Simulation of electrostatic systems in periodic boundary conditions. I. Lattice sums and dielectric constants. *Proc. R. Soc. Lond.*, 373:27–56, 1980.

[159] A. Jakalian, D. B. Jack, and C. I. Bayly. Fast, efficient generation of high-quality atomic charges. AM1-BCC model: Ii. parameterization and validation. *J. Comput. Chem.*, 23:1623–1641, 2002.

[160] J. Wang, R. M. Wolf, J. W. Caldwell, P. A. Kollman, and D. A. Case. Development and testing of a general amber force field. *J. Comput. Chem.*, 25:1157–1174, 2004.

[161] A. D. Mackerell. Empirical force fields for biological macromolecules: overview and issues. *J. Comput. Chem.*, 25:1584–1604, 2004.

[162] V. Hornak, R. Abel, A. Okur, B. Strockbine, A. Roitberg, and C. Simmerling. Comparison of multiple amber force fields and development of improved protein backbone parameters. *Proteins*, 65:712–725, 2006.

[163] S. Patel, A. D. Mackerell, and C. L. Brooks. Charmm fluctuating charge force field for proteins: Ii - protein/solvent properties from molecular dynamics simulations using a nonadditive electrostatic model. *J. Comput. Chem.*, 25:1504–1514, 2004.

[164] G. A. Kaminski, R. A. Friesner, J. Tirado-Rives, and W. L. Jorgensen. Evaluation and reparametrization of the OPLS-AA force field for proteins via comparison with accurate quantum chemical calculations on peptides. *J. Phys. Chem. B*, 105:6474–6487, 2001.

[165] X. Daura, B. Oliva, E. Querol, F.X. Aviles, and O. Tapia. On the sensitivity of md trajectories to changes in water-protein interaction parameters: The potato carboxypeptidase inhibitor in water as a test case for the gromos force field. *Proteins: Struct., Funct., Genet.*, 25:89–103, 1996.

[166] C. J. Cramer and D. G. Truhlar. Implicit solvation models:? equilibria, structure, spectra, and dynamics. *Chem. Rev.*, 99:2161–2200, 1999.

[167] C. R. W. Guimaraes, G. Barreiro, C. A. F. de Oliveira, and R. B. de Alencastro. On the application of simple explicit water models to the simulations of biomolecules. *Braz. J. Phys.*, 34, 2004.

[168] W. L. Jorgensen, J. Chandrasekhar, J. D. Madura, R. W. Impey, and M. L. Klein. Comparison of simple potential functions for simulating liquid water. *J. Chem. Phys.*, 79:926–936, 1983.

[169] H. J. C. Berendsen, J. P. M. Postma, W. F. Vangunsteren, A. Dinola, and J. R.

Haak. Molecular dynamics with coupling to an external bath. *J. Chem. Phys.*, 81:3684–3690, 1984.

[170] N. Dragneva, W. B. Floriano, D. Stauffer, R. C. Mawhinney, G. Fanchini, and O. Rubel. Favorable adsorption of capped amino acids on graphene substrate driven by desolvation effect. *J. Chem. Phys.*, 139:174711–174711–6, 2013.

[171] Y. Shao, J. Wang, H. Wu, J. Liu, I. A. Aksay, and Y. Lina. Graphene based electrochemical sensors and biosensors: A review. *Electroanal.*, 22:1027–1036, 2009.

[172] H. Chang, L. Tang, Y. Wang, J. Jiang, and J. Li. Graphene fluorescence resonance energy transfer aptasensor for the thrombin detection. *Anal. Chem.*, 82:2341–2346, 2010.

[173] Y. Wang, Z. Li, D. Hu, C.T. Lin, J. Li, and Y. Lin. Aptamer/graphene oxide nanocomplex for in situ molecular probing in living cells. *J. Am. Chem. Soc.*, 132:9274–9276, 2010.

[174] L. Tang, Y. Wang, Y. Liu, and J. Li. Dna-directed self-assembly of graphene oxide with applications to ultrasensitive oligonucleotide assay. *ACS Nano*, 5:3817–3822, 2011.

[175] X. Dong, J. Cheng, J. Li, and Y. Wang. Graphene as a novel matrix for the analysis of small molecules by maldi-tof ms. *Anal. Chem.*, 82:6208–6214, 2010.

[176] M. Zhang, B.-C. Yin, X.-F. Wanga, and B.-C. Ye. Interaction of peptides with

graphene oxide and its application for real-time monitoring of protease activity. *Chem. Commun.*, 47:2399–2401, 2011.

[177] O. Akhavan, E. Ghaderi, and R. Rahighi. Toward single-dna electrochemical biosensing by graphene nanowalls. *ACS Nano*, 6:2904–2916, 2012.

[178] M. S. Mannoor, H. Tao, J. D. Clayton, A. Senguptaa, D. L. Kaplan, R. R. Naik, N. V., F. G. Omenetto, and M. C. McAlpine. Graphene-based wireless bacteria detection on tooth enamel. *Nat. Commun.*, 3:763–769, 2012.

[179] T. Feng, D. Feng, W. Shi, X. Li, and H. Ma. A graphene oxide-peptide fluorescence sensor for proteolytically active prostate-specific antigen. *Mol. BioSyst.*, 8:1441–1445, 2012.

[180] Y. Zhang, J. Zhang, X. Huang, X. Zhou, H. Wu, and S. Guo. Assembly of graphene oxide-enzyme conjugates through hydrophobic interaction. *Small*, 8:154–159, 2012.

[181] W. Sun and Y. Bu. Interaction between glycine/glycine radicals and intrinsic/boron-doped (8,0) single-walled carbon nanotubes: a density functional theory study. *J. Phys. Chem.*, 112:15442–15449, 2008.

[182] Z. Liu, J. Robinson, X. Sun, and H. Dai. Pegylated nanographene oxide for delivery of water-insoluble cancer drugs. *J. Am. Chem. Soc.*, 130:10876–10877, 2008.

[183] L. Zhang, J. Xia, Q. Zhao, L. Liu, and Z. Zhang. Functional graphene oxide as

a nanocarrier for controlled loading and targeted delivery of mixed anticancer drugs. *Small*, 6:537–44, 2010.

[184] K. Yang, S. Zhang, G. Zhang, X. Sun, S. Lee, and Z. Liu. Graphene in mice: Ultrahigh in vivo tumor uptake and efficient photothermal therapy. *Nano. Lett.*, 10:3318–3323, 2010.

[185] F. Sharifi, R. Bauld, M. Shafiq Ahmed, and G. Fanchini. Transparent and conducting graphenerna-based nanocomposites. *Small*, 8:699–706, 2012.

[186] X. Hu, L. Mu, J. Wen, and Q. Zhou. Immobilized smart rna on graphene oxide nanosheets to specifically recognize and adsorb trace peptide toxins in drinking water. *J. Hazard. Mater.*, 213–214:387–392, 2012.

[187] C. Rajesh, C. Majumder, H. Mizuseki, and Y. Kawazoe. A theoretical study on the interaction of aromatic amino acids with graphene and single walled carbon nanotube. *J. Chem. Phys.*, 130:124911–124911–6, 2009.

[188] W. Qin, X. Li, Wen-Wen Bian, X.-J. Fan, and J.-Y. Qi. Density functional theory calculations and molecular dynamics simulations of the adsorption of biomolecules on graphene surfaces. *Biomaterials*, 31:1007–1016, 2010.

[189] C. Cazorla. *Ab initio* study of the binding of collagen amino acids to graphene and A-doped (A=H, Ca) graphene. *Thin Solid Films*, 518:6951–6961, 2010.

[190] R. B. Pandey, Z. Kuang, B. L. Farmer, S. S. Kim, and R. R. Naik. Stability of peptide (P1 and P2) binding to a graphene sheet via an all-atom to all-residue coarse-grained approach. *Soft Matter*, 8:9101–9109, 2012.

[191] B. L. Woods and R. A. Walker. ph effects on molecular adsorption and solvation of p-nitrophenol at silica/aqueous interfaces. *J. Phys. Chem. A*, 117:6224–6233, 2013.

[192] X. Zhang, M. M. Cunningham, and R. A. Walker. Solvent polarity at polar solid surfaces: The role of solvent structure. *J. Phys. Chem. B*, 107:3183–3195, 2003.

[193] L. M. Ghiringhelli, B. Hess, N. F.A. van der Vegt, and L. D. Site. Competing adsorption between hydrated peptides and water onto metal surfaces: From electronic to conformational properties. *J. Am. Chem. Soc.*, 130:13460–13464, 2008.

[194] R. W. G. Wyckoff. *Crystal structures.* New York: Interscience Publishers, 1963.

[195] E. Krieger, G. Koraimann, and G. Vriend. Increasing the precision of comparative models with YASARA NOVA - a self-parameterizing force field. *Proteins*, 47:393–402, 2002.

[196] Y. Duan, C. Wu, S. Chowdhury, M.C. Lee, G. Xiongand, W. Zhang, R. Yang, P. Cieplak, R. Luo, T. Lee, J. Caldwell, J. Wang, and P. Kollman. A point-charge force field for molecular mechanics simulations of proteins based on condensed-phase quantum mechanical calculations. *J. Comput. Chem.*, 24:1999–2012, 2003.

[197] A. Courty, M. Mons, N. Dimicoli, F. Piuzzi, M. P. Gaigeot, V. Brenner, P. de Pujo, and P. Millie. Quantum effects in the threshold photoionization

and energetics of the benzene-H2O and benzene-D2O complexes: Experiment and simulation. *J. Phys. Chem. A*, 102:6590–6600, 1998.

[198] C. S. Lin, R. Q. Zhang, Zaric S., G. Lee, M. Elstner, T. Frauenheim, and L. J. Wan. Simulation of water cluster assembly on a graphite surface. *J. Phys. Chem. B*, 109:14183–14188, 2005.

[199] I. W. Sudiarta and D. J. W. Geldart. Interaction energy of a water molecule with a single-layer graphitic surface modeled by hydrogen- and fluorine-terminated clusters. *J. Phys. Chem. A*, 110:10501–10506, 2006.

[200] D. J. Wallace Geldart, I. W. Sudiarta, G. Lesins, and P. Chylek. Interaction between a water molecule and a graphite surface. *Chem. Phys.*, 2008.

[201] D. Feller and K. D. Jordan. Estimating the strength of water/single-layer graphite interaction. *J. Phys. Chem. A*, 104:9971–9975, 2000.

[202] J. W. Han and D. S. Sholl. Enantiospecific adsorption of amino acids on hydroxylated quartz (0001). *Langmuir*, 25:10737–10745, 2009.

[203] L. M. Ghiringhelli, P. Schravendijk, and L. D. Site. Adsorption of alanine on a Ni(111) surface: A multiscale modeling oriented density functional study. *Phys. Rev. B*, 74:035437, 2006.

[204] A. Rimola, M. Sodupe, and P. Ugliengo. Affinity scale for the interaction of amino acids with silica surfaces. *J. Phys. Chem. C*, 113:5741–5750, 2009.

[205] M. Corno, A. Rimola, V. Bolisb, and P. Ugliengo. Hydroxyapatite as a key

biomaterial: quantum-mechanical simulation of its surfaces in interaction with biomolecules. *Phys. Chem. Chem. Phys.*, 12:6309–6329, 2010.

[206] A. Rimola, M. Aschi, R. Orlando, and P. Ugliengo. Does adsorption at hydroxyapatite surfaces induce peptide folding? insights from large-scale b3lyp calculations. *J. Am. Chem. Soc.*, 134:10899–10910, 2012.

[207] A. N. Camden, S. A. Barr, and R. J. Berry. Simulations of peptide-graphene interactions in explicit water. *J. Chem. Phys. B*, 117:10691–10697, 2013.

[208] M. Bulacu, N. Goga, W. Zhao, G. Rossi, L. Monticelli, X. Periole, D. P. Tieleman, , and S. J. Marrink. Improved angle potentials for coarse-grained molecular dynamics simulations. *J. Chem. Theory Comput.*, 9:3282–3292, 2013.

[209] S. B. Dixit, R. Bhasin, E. Rajasekaran, and B. Jayaram. Solvation thermodynamics of amino acids assessment of the electrostatic contribution and force-field dependence. *J. Chem. Soc., Faraday Trans.*, 93:1105–1113, 1997.

[210] R. S. Paton and J. M. Goodman. Hydrogen bonding and pi-stacking: how reliable are force fields? a critical evaluation of force field descriptions of nonbonded interactions. *J. Chem. Inf. Model.*, 49:944–955, 2009.

[211] D. Stauffer, N. Dragneva, W. B. Floriano, R. C. Mawhinney, G. Fanchini, S. French, and O. Rubel. An atomic charge model for graphene oxide for exploring its bioadhesive properties in explicit water. *J. Chem. Phys.*, 141:044705–044705–8, 2014.

[212] C. Cha, S. Ryon Shin, N. Annabi, M. R. Dokmeci, and A. Khademhosseini.

Carbon-based nanomaterials: multifunctional materials for biomedical engineering. *ACS Nano*, 7:2891–2897, 2013.

[213] D. Depan, B. Girase, J. S. Shah, and R. D. Misra. Structure-process-property relationship of the polar graphene oxide-mediated cellular response and stimulated growth of osteoblasts on hybrid chitosan network structure nanocomposite scaffolds. *Acta Biomater.*, 7:3432–3445, 2012.

[214] K. Wang, J. Ruan, H. Song, J. Zhang, Y. Wo, S. Guo, and D. Cui. Biocompatibility of graphene oxide. *Nanoscale Res. Lett.*, 6, 2011.

[215] Y. Zhang, S. F. Ali, E. Dervishi, Y. Xu, Z. Li, D. Casciano, and A. S. Biris. Cytotoxicity effects of graphene and single-wall carbon nanotubes in neural phaeochromocytoma-derived pc12 cells. *ACS Nano*, 4:3181–3186, 2010.

[216] Y. Zhang, C. Wu, S. Guo, and J. Zhang. Interactions of graphene and graphene oxide with proteins and peptides. *Nanotech. Rev.*, 2:27–45, 2013.

[217] S. Li, A. N. Aphale, I. G. Macwan, P. K. Patra, W. G. Gonzalez, J. Miksovska, and R. M. Leblanc. Graphene oxide as a quencher for fluorescent assay of amino acids, peptides, and proteins. *ACS Appl. Mater. Interfaces*, 4:7069–7075, 2012.

[218] J. J. Gray. The interaction of proteins with solid surfaces. *Curr. Opin. Struct. Biol.*, 14:110–115, 2004.

[219] K. A. Mkhoyan, A. W. Contryman, J. Silcox, D. A. Stewart, G. Eda, C. Mattevi, S. Miller, and M. Chhowalla. Atomic and electronic structure of graphene-oxide. *Nano Lett.*, 9:1058–1063, 2009.

[220] Z. Xu and K. Xue. Engineering graphene by oxidation: a first-principles study. *Nanotech.*, 21, 2010.

[221] M. Topsakal and S. Ciraci. Domain formation on oxidized graphene. *Phys. Rev. B*, 86, 2012.

[222] A. Bagri, C. Mattevi, M. Acik, Y. J. Chabal, M. Chhowalla, and V. B. Shenoy. Structural evolution during the reduction of chemically derived graphene oxide. *Nat. Chem.*, 2:581–587, 2010.

[223] H. Pan, J. Tao, X. Xu, and R. Tang. Adsorption processes of gly and glu amino acids on hydroxyapatite surfaces at the atomic level. *Langmuir*, 23:8972–8981, 2007.

[224] L. Feng, S. Zhang, and Z. Liu. Graphene based gene transfection. *Nanoscale*, 3:1252, 2011.

[225] X. Gonze, G. M. Rignanese, M. Verstraete, J. M. Beuken, Y. Pouillon, R. Caracas, F. Jollet, M. Torrent, G. Zerah, M. Mikami, Ph. Ghosez, M. Veithen, J. Y. Raty, V. Olevano, F. Bruneval, L. Reining, R. Godby, G. Onida, D. R. Hamann, and D. C. Allan. A brief introduction to the abinit software package. *Zeit. Kristallogr.*, 220:558–562, 2005.

[226] X. Gonze, B. Amadon, P.-M. Anglade, J.-M. Beuken, F. Bottin, P. Boulanger, F. Bruneval, D. Caliste, R. Caracas, M. Cote, T. Deutsch, L. Genovese, Ph. Ghosez, M. Giantomassi, S. Goedecker, D. R. Hamann, P. Hermet, F. Jollet, G. Jomard, S. L., M. Mancini, S. Mazevet, M. J. T. Oliveira, G. Onida, Y. Pouillon, T. Rangel, G.-M. Rignanese, D. Sangalli, R. Shaltaf, M. Torrent, M. J.

Verstraete, G. Zerah, and J. W. Zwanziger. Abinit: First-principles approach to material and nanosystem properties. *Comp. Phys. Commun.*, 180:2582–2615, 2009.

[227] N. Troullier and J. L. Martins. Efficient pseudopotentials for plane-wave calculations. *Phys. Rev. B*, 43:1993–2006, 1991.

[228] J. P. Perdew, K. Burke, and M. Ernzerhof. Generalized gradient approximation made simple. *Phys. Rev. Lett.*, 77:3865–3868, 1996.

[229] J.-A. Yan and M. Y. Chou. Oxidation functional groups on graphene: Structural and electronic properties. *Phys. Rev. B*, 82:125403–125413, 2010.

[230] Y. Mo and J. Gao. Polarization and charge-transfer effects in aqueous solution via ab initio qm/mm simulations. *J. Phys. Chem. B*, 110:2976–2980, 2006.

[231] I. V. Leontyev, M. V. Vener, I. V. Rostov, M. V. Basilevsky, and M. D. Newton. Continuum level treatment of electronic polarization in the framework of molecular simulations of solvation effects. *J. Chem. Phys.*, 119:8024–8038, 2003.

[232] J. Gao. Toward a molecular orbital derived empirical potential for liquid simulations. *J. Phys. Chem. B*, 101:657–663, 1997.

[233] O. Guvench, S. S. Mallajosyula, E. P. Raman, E. Hatcher, K. Vanommeslaeghe, T. J. Foster, F. W. Jamison, and A. D. MacKerell. Charmm additive all-atom force field for carbohydrate derivatives and its utility in polysaccharide and carbohydrateprotein modeling. *J. Chem. Theory Comput.*, 7:3162–3180, 2011.

[234] I. V. Leontyev and A. A. Stuchebrukhov. Electronic polarizability and the effective pair potentials of water. *J. Chem. Theory Comput.*, 6:3153–3161, 2010.

[235] D. L. Chen, A. C. Stern, B. Space, and J. K. Johnson. Atomic charges derived from electrostatic potentials for molecular and periodic systems. *J. Phys. Chem. A*, 114:10225–10233, 2010.

[236] A. A. Bliznyuk, A. P. Rendell, T. W. Allen, and S. H. Chung. The potassium ion channel: Comparison of linear scaling semiempirical and molecular mechanics representations of the electrostatic potential. *J. Phys. Chem. B*, 105:12674–12679, 2001.

[237] P. E. Mason, E. Wernersson, and P. Jungwirth. Accurate description of aqueous carbonate ions: an effective polarization model verified by neutron scattering. *J. Phys. Chem. B*, 116:8145–8153, 2012.

[238] C. I. Bayly, P. Cieplak, W. Cornell, and P. A. Kollman. A well-behaved electrostatic potential based method using charge restraints for deriving atomic charges: the resp model. *J. Phys. Chem.*, 97:10269–10280, 1993.

[239] J. Zeng, L. Duan, J. Z. Zhang, and Y. Mei. A numerically stable restrained electrostatic potential charge fitting method. *J. Comput. Chem.*, 34:847–853, 2013.

[240] R. Garemyr and A. Elofsson. Study of the electrostatics treatment in molecular dynamics simulations. *Proteins*, 37:417–428, 1999.

[241] Y. Li, B. Pathak, J. Nisar, Z. Qian, and R. Ahuja. Metal-decorated graphene oxide for ammonia adsorption. *EPL*, 103, 2013.

[242] A. P. Smith, A. E. McKercher, and R. C. Mawhinney. Inductive effect: A quantum theory of atoms in molecules perspective. *J. Phys. Chem. A*, 115:12544–12554, 2011.

[243] P. Mark and L. Nilsson. Structure and dynamics of the TIP3P, SPC, and SPC/E water models at 298 K. *J. Phys. Chem.*, 105:9954–9960, 2001.

[244] J. Gao and X. Xia. A priori evaluation of aqeous polarization effects through monte carlo qm-mm simulations. *Science*, 258:631–635, 1992.

[245] M. R. Shirts and V. S. Pande. Solvation free energies of amino acid side chain analogs for common molecular mechanics water models. *J. Chem. Phys.*, 122, 2005.

[246] Y. Tu and A. Laaksonen. Atomic charges in molecular mechanical force fields: a theoretical insight. *Phys. Rev. E*, 64, 2001.

[247] H. Heinz and U. W. Suter. Atomic charges for classical simulations of polar systems. *J. Phys. Chem. B*, 108:18341–18352, 2004.

[248] F. Martin and H. Zipse. Charge distribution in the water molecule a comparison of methods. *J. Comput. Chem.*, 26:97–105, 2005.

[249] R. D. King-Smith and D. Vanderbilt. Theory of polarization of crystalline solids. *Phys. Rev. B*, 47:1651–1654, 1993.

[250] P. L. Silvestrelli and M. Parrinello. Water molecule dipole in the gas and in the liquid phase. *Phys. Rev. Lett.*, 82:3308–3311, 1999.

[251] A. D. MacKerell, Jr. D. Bashford, Jr. M. R. L. Dunbrack, J. D. Evanseck, M. J. Field, S. Fischer, J. Gao, H. Guo, S. Ha, D. Joseph-McCarthy, L. Kuchnir, K. Kuczera, F. T. K. Lau, C. Mattos, S. Michnick, T. Ngo, D. T. Nguyen, B. Prodhom, W. E. Reiher, B. Roux, M. Schlenkrich, J. C. Smith, R. Stote, J. Straub, M. Watanabe, J. Wiorkiewicz-Kuczera, D. Yin, and M. Karplus. All-atom empirical potential for molecular modeling and dynamics studies of proteins. *J. Phys. Chem.*, 102:3586–3616, 1998.

[252] B. T. Thole. Molecular polarizabilities calculated with a modified dipole interaction. *Chem. Phys.*, 59:341–350, 1981.

[253] D. L. Mobley, E. Dumont, J. D. Chodera, and K. A. Dill. Comparison of charge models for fixed-charge force fields: Small-molecule hydration free energies in explicit solvent. *J. Phys. Chem. B*, 111:2242–2254, 2007.

[254] V. C. Tung, M. J. Allen, Y. Yang, and R. B. Kaner. High-throughput solution processing of large-scale graphene. *Nat. Nanotech.*, 4, 2009.

[255] M. J. McAllister, J.-L. Li, D. H. Adamson, H. C. Schniepp, A. A. Abdala, J. Liu, M. Herrera-Alonso, D. L. Milius, R. Car, R. K. Prud'homme, and I. A. Aksay. Single sheet functionalized graphene by oxidation and thermal expansion of graphite. *Chem. Mater.*, 19:4396–4404, 2007.

[256] N. Ghaderi and M. Peressi. First-principles study of hydroxyl functional groups

on pristine, defected graphene, and graphene epoxide. *J. Phys. Chem. C*, 114:21625–21630, 2010.

[257] H. C. Schniepp, J.-L. Li, M. J. McAllister, H. Sai, M. Herrera-Alonso, D. H. Adamson, R. K. Prud'homme, R. Car, D. A. Saville, and I. A. Aksay. Functionalized single graphene sheets derived from splitting graphite oxide. *J. Phys. Chem. B*, 110:8535–8539, 2006.

[258] D. R. Dreyer, S. Park, C. W. Bielawski, and R. S. Ruoff. The chemistry of graphene oxide. *Chem. Soc. Rev.*, 39:228–240, 2010.

[259] S. Radic, N. K. Geitner, R. Podila, P. C. Ke, and F. Ding. Competitive binding of natural amphiphiles to graphene derivatives. *Nanotech.*, 3:163–166, 2013.

[260] L. Shahriary and A. A. Athawale. Graphene oxide synthesized by using modified hummers approach. *Int. J. Energy Environ. Eng.*, 2:58–63, 2014.

[261] M. Hirata, T. Gotou, S. Horiuchi, M. Fujiwara, and M. Ohba. Thin-film particles of graphite oxide 1: High-yield synthesis and flexibility of the particles. *Carbon*, 42:2929–2937, 2004.

[262] D. Yu and L. Dai. Self-assembled graphene/carbon nanotube hybrid films for supercapacitors. *J. Phys. Chem. Lett.*, 1:467–470, 2010.

[263] H. Ahn, T. Kimband, H. Choia, C. Yoonaa, K. Uma, J. Namc, K. H. Ahnd, and K. Lee. Gelation of graphene oxides induced by different types of amino acids. *Carbon*, 71:229–237, 2014.

[264] C. D. Walkey and W. C. W. Chan. Understanding and controlling the interaction of nanomaterials with proteins in a physiological environment. *Chem. Soc. Rev.*, 41:2780–2799, 2012.

[265] R. G. Richards. Implant surfaces: Do they have any relevance to the surgeon? *Aodialogue*, 1:20–24, 2007.

[266] R. A. Adams, M. Passino, B. D. Sachs, T. Nuriel, and K. Akassoglou. Fibrin mechanisms and functions in nervous system pathology. *Mol. Interv.*, 4:163–176, 2004.

[267] L. Tang and J. W. Eaton. Natural responses to unnatural materials: A molecular mechanism for foreign body reactions. *Mol. Med.*, 5:351–358, 1999.

[268] T. P. Ugarova and V. P. Yakubenko. Recognition of fibrinogen by leukocyte integrins. *Ann. N. Y. Acad. Sci.*, 936:368–385, 2001.

[269] K. L. Marchin and C. L. Berrie. Conformational changes in the plasma protein fibrinogen upon adsorption to graphite and mica investigated by atomic force microscopy. *Langmuir*, 19:9883–9888, 2003.

[270] A. Agnihotri and C. A. Siedlecki. Time-dependent conformational changes in fibrinogen measured by atomic force microscopy. *Langmuir*, 20:8846–8852, 2004.

[271] R. T. T. Gettens, Z. J. Bai, and J. L. Gilbert. Quantification of the kinetics and thermodynamics of protein adsorption using atomic force microscopy. *J. Biomed. Mater. Res. A*, 72A:246, 2005.

[272] R. E. Marchant, M.D. Barb, J. R. Shainoff, S. J. Eppell, D. L. Wilson, and C. A. Siedlecki. Three dimensional structure of human fibrinogen under aqueous conditions visualized by atomic force microscopy. *Thromb. Haemost.*, 77:1048–1051, 1997.

[273] P. Sidney Sit and R. E. Marchant. Surface-dependent differences in fibrin assembly visualized by atomic force microscopy. *Surf. Sci.*, 491:421–432, 2001.

[274] M. M. Santore and C. F. Wertz. Protein spreading kinetics at liquid-solid interfaces via an adsorption probe method. *Langmuir*, 21:10172–10178, 2005.

[275] K. D. Jandt, M. Finke, and P. Cacciafesta. Aspects of the physical chemistry of polymers, biomaterials and mineralised tissues investigated with atomic force microscopy (AFM). *Colloid. Surface B*, 19:301–314, 2000.

[276] R. Wigren, H. Elwing, R. Erlandsson, S. Welin, and I. Lundstrom. Structure of adsorbed fibrinogen obtained by scanning force microscopy. *FEBS Lett.*, 280:225–228, 1991.

[277] D. J. Taatjes, A. S. Quinn, R. J. Jenny, P. Hale, E. G. Bovill, and J. McDonagh. Tertiary structure of the hepatic cell protein fibrinogen in fluid revealed by atomic force microscopy. *Cell Biol. Int.*, 21:715–726, 1997.

[278] K. Bergstrom, K. Holmberg, A. Safranj, A. S. Hoffman, M. J. Edgell, A. Kozlowski, B. A. Hovanes, and J. M. Harris. Reduction of fibrinogen adsorption on peg-coated polystyrene surfaces. *J. Biomed. Mater. Res.*, 26:779–790, 1992.

[279] M. E. Price, R. M Cornelius, and J. L. Brash. Protein adsorption to polyethylene

glycol modified liposomes from fibrinogen solution and from plasma. *Biomembranes*, 1512:191–205, 2001.

[280] K. E. Bremmell, P. Kingshott, Z. Ademovic, B. Winther-Jensen, and H. J. Griesser. Colloid probe AFM investigation of interactions between fibrinogen and PEG-like plasma polymer surfaces. *Langmuir*, 22:313–318, 2006.

[281] J.-W. Shen, T. Wu, and Q. Wang and H.-H. Pan. Molecular simulation of protein adsorption and desorption on hydroxyapatite surfaces. *Biomaterials*, 29:513–532, 2008.

[282] M. Agashe, V. Raut, S. J. Stuart, and R. A. Latour. Molecular simulation to characterize the adsorption behavior of a fibrinogen γ-chain fragment. *Langmuir*, 21:1103–1117, 2005.

[283] G. Spraggon, S. J. Everse, and R. F. Doolittle. Crystal structures of fragment d from human fibrinogen and its crosslinked counterpart from fibrin. *Nature*, 389, 1997.

[284] M. Kalbacova, A. Broz, J. Kong, and M. Kalba. Graphene substrates promote adherence of human osteoblasts and mesenchymal stromal cells. *Carbon*, 48:4323–4329, 2010.

[285] Y. Li, Y. Liu, Y. Fu, T. Wei, L. L. Guyader, G. Gao, R.-S. Liu, Y.-Z. Chang, and C. Chen. The triggering of apoptosis in macrophages by pristine graphene through the MAPK and TGF-β signaling pathways. *Biomaterials*, 33:402–411, 2012.

[286] A. Schinwald, F. A. Murphy, A. Jones, W. MacNee, and K. Donaldson. Graphene-based nanoplatelets: A new risk to the respiratory system as a consequence of their unusual aerodynamic properties. *ACS Nano*, 6:736–746, 2012.

[287] K.-H. Liao, Y.-S. Lin, C. W. Macosko, and C. L. Haynes. Previous article next article table of contents cytotoxicity of graphene oxide and graphene in human erythrocytes and skin fibroblasts. *ACS Appl. Mater. Interfaces*, 3:2607–2615, 2011.

[288] M. Mrksich and G. M. Whitesides. Using self-assembled monolayers that present oligo(ethyleneglycol) groups to control the interactions of proteins with surfaces. *ACS*, pages 361–373, 1997.

[289] P. Harder, M. Grunze, R. Dahint, G. M. Whitesides, and P. E. Laibinis. Molecular conformation in oligo(ethylene glycol)-terminated self-assembled monolayers on gold and silver surfaces determines their ability to resist protein adsorption. *J. Phys. Chem. B*, 102:426–436, 1998.

[290] HIC-Up. Hetero-compound information centre uppsala. *http://xray.bmc.uu.se/hicup/15P/.*

[291] Z. Yang, J. A. Galloway, and H. Yu. Protein interactions with poly(ethylene glycol) self-assembled monolayers on glass substrates: Diffusion and adsorption. *Langmuir*, 15:8405–8411, 1999.

[292] N. A. Alcantar, E.S. Aydil, and J.N. Israelachvili. Polyethylene glycolcoated biocompatible surfaces. *J. Biomed. Mater. Res.*, 51:343–351, 2000.

[293] G. Thakur, K. Prashanthi, and T. Thundat. Directed self-assembly of proteins into discrete radial patterns. *Sci. Rep.*, 3:1923, 2013.

[294] S. Evan. *Improving Biocompatibility By Controlling Protein Adsorption: Modification And Design Of Biomaterials Using Poly(Ethylene Glycol) Microgels And Microspheres.* All Theses and Dissertations (ETDs). Paper 316., 2009.

[295] U. Essman, L. Perera, M. L. Berkowitz, T. Darden, H. Lee, and L. G. Pedersen. A smooth particle mesh ewald method. *J. Chem. Phys. B*, 103:8577–8593, 1995.

[296] M. Y. Lobanov, N. S. Bogatyreva, and O. V. Galzitskaya. Radius of gyration as an indicator of protein structure compactness. *Mol. Biol.*, 42:623–628, 2008.

[297] L. Hong and J. Lei. Scaling law for the radius of gyration of proteins and its dependence on hydrophobicity. *J. Polym. Sci. Part B: Polym. Phys.*, 47:207–214, 2009.

[298] B. Lee and F. M. Richards. The interpretation of protein structures: estimation of static accessibility. *J. Mol. Biol.*, 55:379–400, 1971.

[299] T. J. Richmond. Solvent accessible surface area and excluded volume in proteins. analytical equations for overlapping spheres and implications for the hydrophobic effect. *J. Mol. Biol.*, 178:63–89, 1984.

[300] J. A. Marsh and S. A. Teichmann. Relative solvent accessible surface area predicts protein conformational changes upon binding. *Structure*, 19:859–867, 2011.

[301] R. E. Hubbard and M. K. Haider. Hydrogen bonds in proteins: Role and strength. *eLS*, 2010.

[302] W. Kabsch and C. Sander. Dictionary of protein secondary structure: pattern recognition of hydrogen-bonded and geometrical features. *Biopolymers*, 22:2577–2637, 1983.

[303] R. P. Joosten, T. A. H.Beek, E. Krieger, M. L. Hekkelman, R. W. W. Hooft, R. Schneider, C. Sander, and G. Vriend. A series of PDB related databases for everyday needs. *Nucleic Acids Research*, 39 (Database issue):D411–D419, 2011.

[304] D. A. C. Beck and V. Daggett. Methods for molecular dynamics simulations of protein folding/unfolding in solution. *Methods*, 34:112–120, 2004.

[305] J. W. Pitera, I. Haque, and W. C. Swope. Absence of reptation in the high-temperature folding of the trpzip2 β-hairpin peptide. *J. Chem. Phys.*, 124:141102–141102–4, 2006.

[306] Y. M. Rhee, E. J. Sorin, G. Jayachandran, E. Lindahl, and V. S. Pande. Simulations of the role of water in the proteinfolding mechanism. *PNAS*, 101:6456–6461, 2004.

[307] A. E. García and J. N. Onuchic. Folding a protein in a computer: An atomic description of the foldingunfolding of protein a. *PNAS*, 100:13898–13903, 2003.

[308] J. Gsponer and A. Caflisch. Molecular dynamics simulations of protein folding from the transition state. *PNAS*, 99:6719–6724, 2002.

[309] S. Wang, Y. Zhang, N. Abidi, and L. Cabrales. Wettability and surface free energy of graphene films. *Langmuir*, 25:110780–11081, 2009.

[310] L. Gao and T. J. McCarthy. A perfectly hydrophobic surface (θa / θr = 180°/ 180°). *J. Am. Chem. Soc.*, 128:9052–9053, 2006.

[311] E. Krieger, K. Joo, J. Lee, S. Raman, J. Thompson, M. Tykaand D. Baker, and K. Karplus. Improving physical realism, stereochemistry, and side-chain accuracy in homology modeling: Four approaches that performed well in CASP8. *Proteins*, 77:114–122, 2009.

[312] B. Sivaraman, K. P. Fears, and R. A. Latour. Investigation of the effects of surface chemistry and solution concentration on the conformation of adsorbed proteins using an improved circular dichroism method. *Langmuir*, 25:3050–3056, 2009.

[313] J. E. Burchenal, C. R. Deible, T. E. Deglau, A. J. Russell, E. J. Beckman, and W. R. Wagner. Polyethylene glycol diisocyanate decreases platelet deposition after balloon injury of rabbit femoral arteries. *J. Thromb. Thrombolysis*, 13:27–33, 2002.

[314] Y. Arima, M. Toda, and H. Iwata. Complement activation on surfaces modified with ethylene glycol units. *Biomaterials*, 29:551–560, 2008.

[315] J. Piehler, A. Brecht, R. Valiokas, B. Liedberg, and G. Gauglitz. A high-density poly(ethylene glycol) polymer brush for immobilization on glass-type surfaces. *Biosens. Bioelectron.*, 15:473481, 2000.

[316] B. Zhu, T. Eurell, R. Gunawan, and D. Leckband. Chain-length dependence of the protein and cell resistance of oligo(ethylene glycol)-terminated self-assembled monolayers on gold. *J. Biomed. Mater. Res.*, 56:406–416, 2001.

[317] T. P. Ugarova, D. A. S. Solovjov L. Zhang, D. I. Loukinov, V. C. Yee, L. V. Medved, and E. F. Plow. Identification of a novel recognition sequence for integrin $\alpha_M\beta_2$ within the γ-chain of fibrinogen. *J. Biol. Chem.*, 273:22519–22527, 1998.

[318] D. A. Solovjov, E. Pluskota, and E. F. Plow. Distinct roles for the α and β subunits in the functions of integrin $\alpha_M\beta_2$. *J. Biol. Chem.*, 280:1336–1345, 2005.

[319] F. Sharifi. *Kelvin Probe Force Microscopy on Graphene Thin Films for Solar Cell and Biosensing Applications.* Electronic thesis and dissertation repository. paper 2597, University of Western Ontario, 2014.

[320] G. Steiner, S. Tunc, M. Maitz, and R. Salzer. Conformational changes during protein adsorption. ft-ir spectroscopic imaging of adsorbed fibrinogen layers. *Anal. Chem.*, 79:1311–1316, 2007.

[321] M.-J. Desroches and S. Omanovic. Adsorption of fibrinogen on a biomedical-grade stainless steel 316lvm surface: a pm-irras study of the adsorption thermodynamics, kinetics and secondary structure changes. *Phys. Chem. Chem. Phys.*, 10:2502–2512, 2008.

[322] J. L. Bohnert and T. A. Horbett. Changes in adsorbed fibrinogen and albumin

interactions with polymers indicated by decreases in detergent elutability. *J. Colloid. Interface Sci.*, 111:363–377, 1986.

[323] S. Muto, V. Vetvicka, and G. D. Ross. CR3 (CD11b/CD18) expressed by cytotoxic t cells and natural killer cells is upregulated in a manner similar to neutrophil CR3 following stimulation with various activating agents. *J. Clin. Immunol.*, 13:175–184, 1993.

[324] G. D. Ross and V. Vetvicka. CR3 (CD11b, CD18): a phagocyte and nk cell membrane receptor with multiple ligand specificities and functions. *Clin. Exp. Immunol.*, 92:181–184, 1993.

[325] Y. T. Bryceson, M. E. March, H. G. Ljunggren, and E. O. Long. Activation, coactivation, and costimulation of resting human natural killer cells. *Immunol. Rev.*, 214:73–91, 2006.

[326] C. R. Almeida, D. P. Vasconcelos, R. M. Gonccalves, and M. A. Barbosa. Enhanced mesenchymal stromal cell recruitment via natural killer cells by incorporation of inflammatory signals in biomaterials. *J. R. Soc. Interface*, 9:261–271, 2012.